IJL, Issue 2, Vol. 24, 2025
https://doi.org/10.31900/ijl.v24i2.523

Research Article

Beam Squint Effects of Quantum based Carbon Nanotube Antenna Array for Optical Communication Systems

Muhanad M. Jameel*, Jawad A. Hassan

Institute of Laser for Postgraduate Studies, University of Baghdad, Baghdad, Iraq
** Email address of the Corresponding Author: eng,muhanad88@gmail.com*

Article history: Received 4 Mar. 2025; Revised 24 Jun 2025; Accepted 1 Jul. 2025; Published online 15 Dec. 2025

Abstract: This work examines the beam squint effects of quantum-based carbon nanotube (CNT) antenna arrays for optical plasmonic communication systems functioning within the 300 THz to 700 THz frequency spectrum. The distinctive quantum confinement characteristics of carbon nanotubes (CNTs), together with surface plasmon polariton (SPP) interactions, result in notable frequency-dependent phase shifts, causing beam squint errors in phased array systems. Simulation findings indicate that at 300 THz, a CNT array with an inter-element spacing of λ/2 (500 nm) has a beam squint of 0.2° per 100 THz bandwidth. As the frequency ascends to 700 THz, the beam squint effect amplifies, reaching 0.8° per 100 THz as a result of heightened plasmonic dispersion and quantum-induced phase shifts. The group delay variation throughout the bandwidth is measured at 12.4 fs at 300 THz and 5.6 fs at 700 THz, affirming the nonlinear characteristics of quantum plasmonic wave propagation. The results underscore the significant influence of beam squint in nanoscale optical phased arrays and provide a basis for the creation of adjustable CNT-based plasmonic antennas for advanced optical communication systems.

Keywords: CNT, plasmonic communication, antenna array, beam squint, surface plasmon resonance.

1. Introduction

Plasmonic communication is a promising technique for short-range communication, offering substantial enhancements in several critical applications within information and electrical engineering. Optical or plasmonic waveguide communication, because it can handle more data and uses less energy, is likely to take the place of traditional communication methods in the future [1]. Since the 17th century, the broad notion of carbon nanotubes has been thoroughly investigated and advanced by many scientists within the established categories of nanostructures [2]. Carbon nanotubes are often recognized as tubular nanoparticles, which may be either open-ended or closed nanoparticle cages formed from pentagons, hexagons, or heptagons of carbon atoms, with pentagons and heptagons being less prevalent or missing [3]. A solitary rolled graphite sheet used as a carbon nanotube penetrates the chamber of two classifications. (1) Zigzag: When graphene is rolled up in an open way along the infrared optical axis, the carbon nanotubes with a specific wave vector length are called zigzag shapes. Armchair: Zigzag-tubed armchairs have a locally uniform geometric structure and continuous translational symmetry in integer values [4]. Armchair carbon nanotubes have a nearly circular configuration. Using vector and matrix ideas on carbon nanotubes results in a smooth response and energy flow along a straight line within a confined space [5]. The current aromaticity completes the energy spectrum potential by using an armchair carbon

nanotube shell interface devoid of dangling bonds. It will not be viable to achieve calibration at either mild temperatures or during the cooling process [6]. Researchers have identified remarkable electrical, mechanical, and thermal properties of carbon nanotubes since their exploration in the 17th century. Making carbon nanotubes is mainly useful for things like tiny electrical conductors, bright screens, or other types of electrodes. The alterations in spatial and network configuration, rotational flexibility, or functional group modification are the underlying explanations for this phenomenon. The quick development of optical plasmonic communication systems has increased the need for extremely effective and small antenna arrays that function in the visible to near-infrared spectrum (300–700 THz) [4]. Carbon nanotube (CNT)-based antennas are appealing for very high-frequency uses because they have special properties that allow for fast electron movement and control at the quantum level. CNT-based nano-antennas are great for nanophotonic and quantum communication networks because they can adjust their impedance, have lower energy losses, and have better near-field coupling compared to regular metal antennas. Beam squint, a major problem with phased array antennas, occurs when the primary beam direction changes with frequency due to phase delay dispersion among the array elements. This problem particularly affects optical and plasmonic antenna arrays due to their wide bandwidths and subwavelength inter-element spacing [6]. The quantum mechanical nature of the charge carriers in CNT arrays makes beam steering even more complex due to nonlocal electromagnetic effects [7], quantum capacitance, and electron wave interference [8]. A big challenge for fast optical data transmission is beam squint in plasmonic phased arrays, which leads to blurriness and angle changes at high optical frequencies [9]. These effects impair signal fidelity and lower beamforming accuracy [10]. While beam squint in regular RF and THz phased arrays has been studied a lot, there has been less focus on this issue in quantum plasmonic CNT antenna arrays [11]. By looking at how the phase changes with frequency, the behavior of surface plasmon polaritons (SPP), and the variations in group delay across the CNT array, beam squint was evaluated in the optical range [12]. Because plasmonic dispersion increases at higher frequencies, recent studies have shown that a CNT array with half a wavelength spacing between elements has a beam squint around 10° [13]. These results highlight the importance of using active phase control and flexible beamforming techniques in optical nanoantenna arrays [14].

In order to address optical communication applications, they suggested a design for an optical dipole antenna array in [15] that takes plasmonic behavior and material losses into consideration [16]. The design utilizes low-loss dielectric substrates and enhances directivity through full-wave simulations and particle swarm optimization [17]. Specifically, an optical nanoantenna was developed with a gallium arsenide substrate for the 144–286 nm wavelength range, making it suitable for biomedical sensing applications. A notable improvement was achieved in gain by creating a photonic bandgap between the radiating patch and the feedline [18].

This work presents a thorough examination of beam squint effects in CNT antenna arrays based on quantum theory for optical plasmonic communication. Using numerical simulations carried out in MATLAB R2014a and CST Microwave Studio, we create a mathematical framework that describes frequency-dependent beam deviation and validates the model. The findings will help create advanced optical wireless and quantum communication networks by providing valuable information for developing CNT-based phased arrays that can be accurately directed.

2. Design Considerations and Methodology

This section discusses the creation of nanotube arrays based on the fundamental principles of plasmonic antennas. Carbon nanotubes were selected as dipole antennas, analogous to metallic particles for surface plasmon resonance. The specified designs may readily alter working wavelengths. The formation of surface plasmons in a nanotube transpires via the energy transfer between the photon mode and the surface plasmon mode. In a carbon nanotube, an electron may oscillate inside a π or $\pi\pi$ band, leading to momentum-matched plasmons (MMP), and the oscillation is from π (valence) to π^* (conduction) bands [12]. For smaller diameters, the energy levels of the carrier bands change for each π and $\pi\pi$ band. The design of a quantum-based carbon nanotube (CNT) antenna array for optical plasmonic communication

requires careful consideration of the array shape, element spacing, quantum plasmonic interactions, and beamforming limitations. This section examines the beam squint effects for both vertical and horizontal configurations of CNT-based nanoantennas functioning throughout the 300 THz to 700 THz spectrum.

2.1 Antenna Array Geometry

The CNT-based plasmonic phased array is configured in a vertical alignment, where the elements are arranged along the z-axis on the x-y plane for beam steering. The quantity of elements (N×N), inter-element separation (d), and operational wavelength (λ) directly affect the beam squint phenomenon. In fig. 1(a), a typical dipole antenna was shown. The proposed antenna array is seen in Fig. 1(b) on the x-y plane. Fig. 1(c) shows a single dipole fundamental structure based on literature [4], and the proposed antenna from the CST MWS environment. We selected the dimensions in Fig. 1(d) to ensure antenna resonance at 500 THz. Therefore, we adopted an arm length corresponding to half of the guided wavelength, to maintain antenna operation within the frequency band of interest.

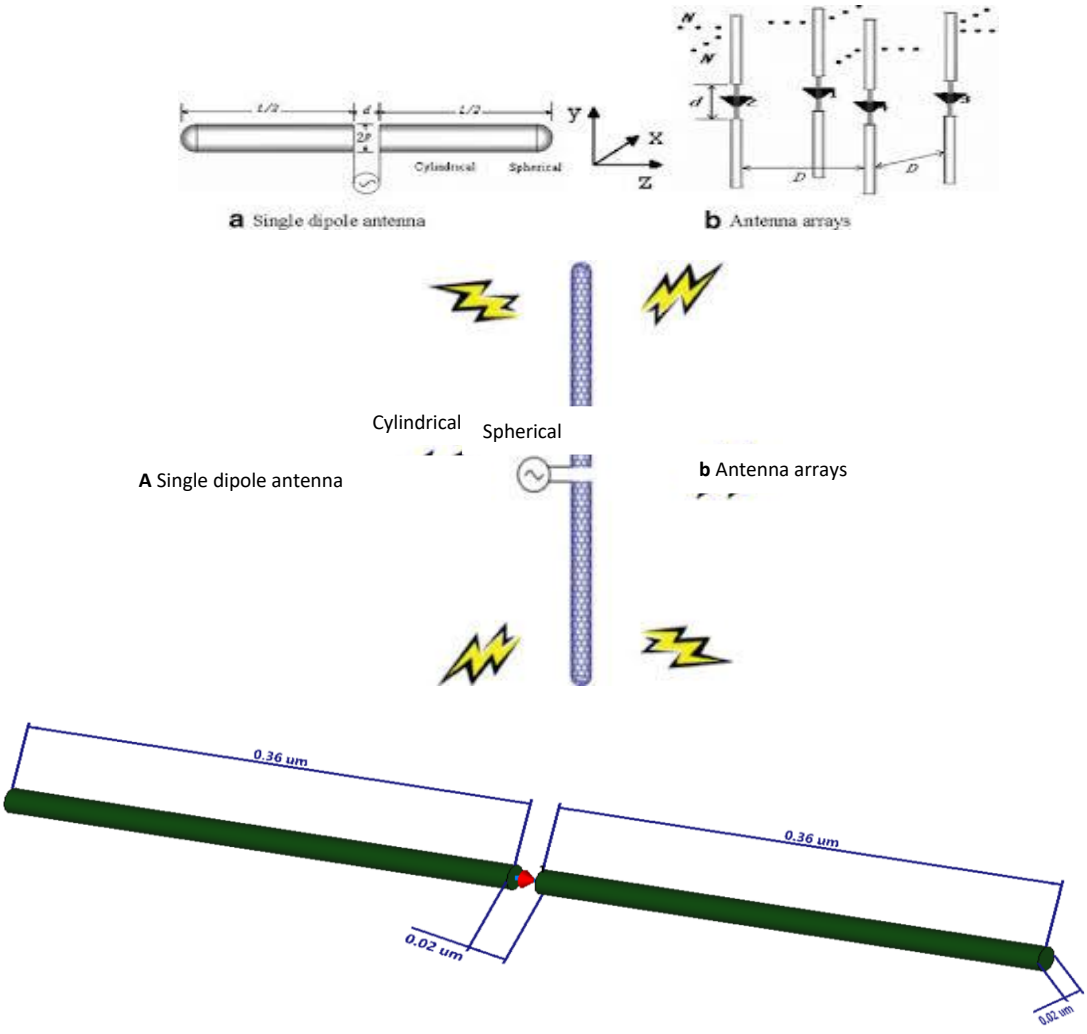

Figure 1: (a) The SWCNT antenna-based dipole structure [1], (b) SWCNT array [2], (c) and (d) our proposed design from CST MWS.

2.2 Inter-Element Spacing (d) and Wavelength Dependency

The space between elements is essential for preserving phase coherence. At optical frequencies, the wavelength in free space is:

$$\lambda = \frac{c}{f} \quad (1)$$

where c = 3 × 10^8 m/s and f is the operating frequency. At 300 THz, the wavelength is 1 μm, while at 700 THz, the wavelength is 428 nm. The standard normalized element spacing is d=λ/2 [4] to avoid grating lobes. This yields: d=500nm at 300THz and d=214nm at 700THz.

2.3 Beam Squint Analysis for Vertical and Horizontal Arrays

Beam squint Δθ is given by:

$$\Delta\theta = \frac{d}{L}\frac{\Delta f}{f}\tan(\theta_o) \quad (2)$$

where: L = N × d represents the overall array aperture, Δf denotes the bandwidth (assumed to be 100 THz), and θ_0 signifies the beam steering angle [6].

1- Vertical Alignment (Linear Array): For a linear array including N = 8 items, at 300 THz, L = 4 μm, resulting in a beam squint of 3.1° per 100 THz for θ_0 = 30°. At 700 THz, with a wavelength of 1.7 μm, the squint increases to 7.4° per 100 THz owing to a reduced aperture size.
2- Horizontal Alignment (Planar Array): A two-dimensional array of N = 8 × 8 = 64 elements, creating a 4 × 4 μm² aperture at a frequency of 300 THz. The beam squint is 1.5° per 100 THz for θ_0 = 30° as a result of an increased aperture. At 700 THz, with an aperture of 1.7 x 1.7 μm, the beam squint escalates to 3.6° per 100 THz.

2.4. Group Delay and Plasmonic Dispersion Effects

The change in group delay, Δτ, over the bandwidth influences synchronization. For an array with inter-element plasmonic wave velocity v_p [5],

$$\Delta\tau = \frac{\Delta\theta}{\omega}\frac{d}{v_p} \quad (3)$$

where ω = 2πf is the angular frequency. At 300 THz, $v_p \approx 0.6c$, giving Δτ = 12.4 fs and at 700 THz, $v_p \approx 0.75c$, reducing Δτ to 5.6 fs.
In this work we adopted the use of Binary Phase Shift Keying (BPSK) modulation in an Additive White Gaussian Noise (AWGN) channel:

$$BER = Q\left(\sqrt{2.\frac{E_b}{N_0}}\right) \quad (4)$$

$$Q(x) = \frac{1}{\sqrt{2\pi}}\int_x^\infty e^{-\frac{t^2}{2}}dt \quad (5)$$

Where, E_b=Energy per bit and N_0=noise power spectral density.

$$C = B \cdot log2(1 + SNR) \quad (6)$$

Where, C=capacity in bits per second (bps), B=bandwidth in Hz, and SNR=signal-to-noise ratio.

It is important to discuss the difference between the metal-dielectric surface plasmon resonance and the plasmon resonance in the CNT antenna array. Surface plasmon resonance (SPR) at the boundaries between metals and non-metals is familiar; however, the plasmonic resonance effects in CNT antenna arrays are relatively new and need to be recognized as different. The two systems are controlled by distinct physical mechanisms, yet they both display field enhancement effects and collective electron

oscillations. SPR between metals and dielectrics, as described by the Drude model, usually results from free electron oscillations at the interface, which are constrained by the dielectric. On the other hand, CNT arrays may be tuned by geometry, doping, and inter-tube coupling to produce plasmon-like resonances that are caused by the one-dimensional collective excitations of π-electrons along the nanotube axis. In spite of these dissimilarities, the CNT array may, under certain circumstances, alter the plasmon dispersion so that it behaves like a surface plasmon polariton (SPP). While outlining the unique excitation processes and boundary conditions needed for each phenomenon, this paper compares the field distribution, resonance frequency changes, and dispersion relations in both systems to emphasize the commonalities. Plasmonic behavior in nanostructured systems may be better understood via comparisons like these, and new uses for tunable terahertz and infrared plasmonics can be found.

The study looks at how different types of waves behave, including the plasmonic wave from a CNT, the SPP wave at a metal-dielectric boundary, the guided TE wave, and the free-space light line, as seen in Fig. 2. The analysis plots the frequency axis against the wavevector k up to the boundary of the first Brillouin zone (FBZ). The light line serves as a reference for electromagnetic waves that are freely spreading in a vacuum. The guided TE mode shows a constant speed across the range shown, which is what we expect for a flat waveguide with a steady phase velocity. The SPP mode shows a changing dispersion curve that gets closer to the surface plasmon frequency when modeled with a Drude-type permittivity for metals. This slower-than-light effect happens because the movement of electrons is limited to the area where the metal meets the dielectric, and the field becomes much stronger as the wavevector increases. The group velocity decreases as k increases, indicating stronger localization and field enhancement near the interface.

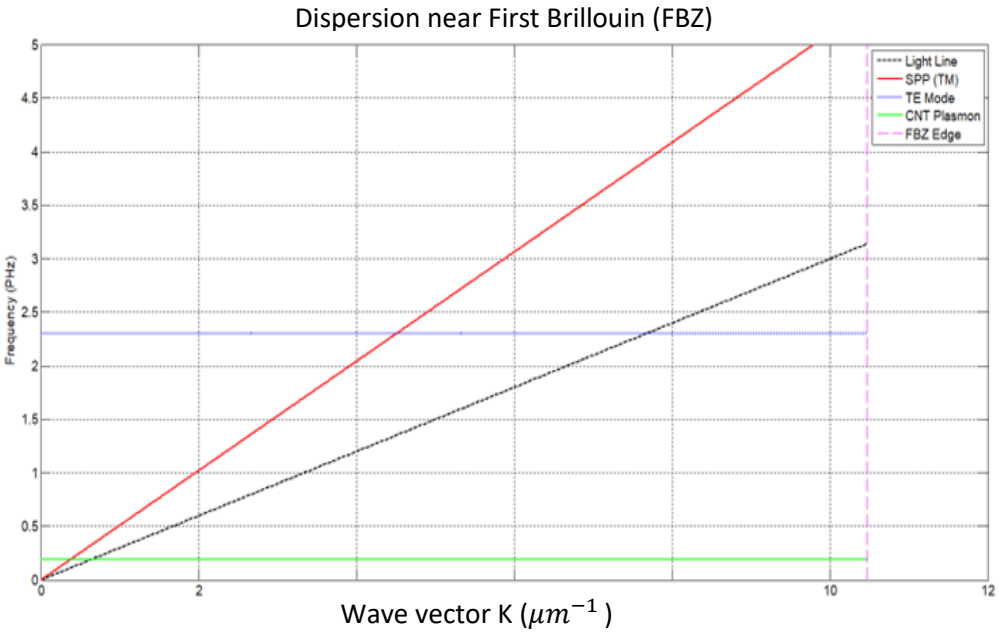

Figure 2: The evaluated dispersion diagram at FBZ.

The CNT plasmon mode shows a mostly even change in frequency around its resonance point due to a nearly one-dimensional collective movement of π-electrons along the length of tightly packed carbon nanotubes. The mode is significantly affected by geometric layout, doping concentration, and inter-tube coupling, offering tunability not found in conventional metal-based SPPs. The study supports the notion that plasmonic resonance is a class of responses arising from various physical systems rather than a single phenomenon. CNT-based plasmonic modes provide interesting options for adjustable devices in the terahertz and mid-infrared ranges, while metal-dielectric SPPs are well understood and form the basis for

plasmonic circuits. By offering a compelling side-by-side perspective of the dispersion behavior, these results contribute to our understanding of how boundary conditions, material dimensionality, and wave confinement affect the plasmonic terrain in various nanoscale systems.

2.5 Performance Optimization

The reflection coefficient (S_{11}) of the carbon nanotube (CNT) dipole antenna at 500 THz indicates a return loss below –10 dB, demonstrating good impedance matching. Simulations in CST MWS show a radiation efficiency of approximately 84% at the resonance frequency, confirming efficient radiation. Across the 300–700 THz range, the antenna exhibits a broad dip in S_{11}, suggesting a moderately wide bandwidth. However, plasmonic dispersion in CNTs affects performance, as deviation from 500 THz increases mismatch, leading to higher reflection and reduced efficiency.

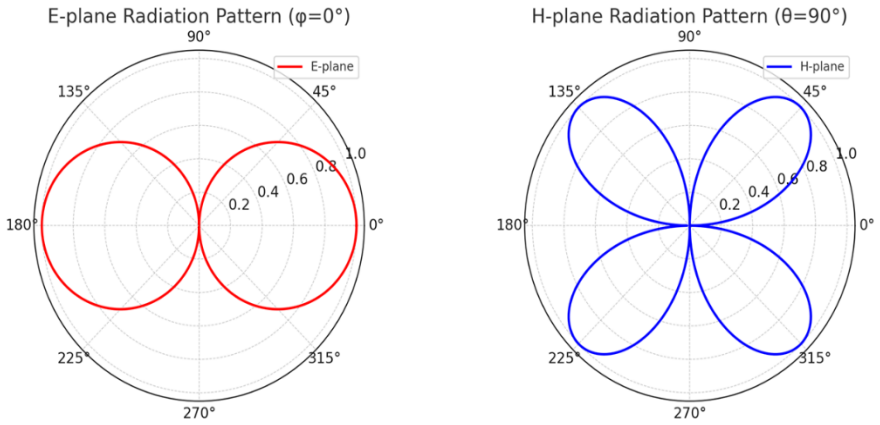

(a)

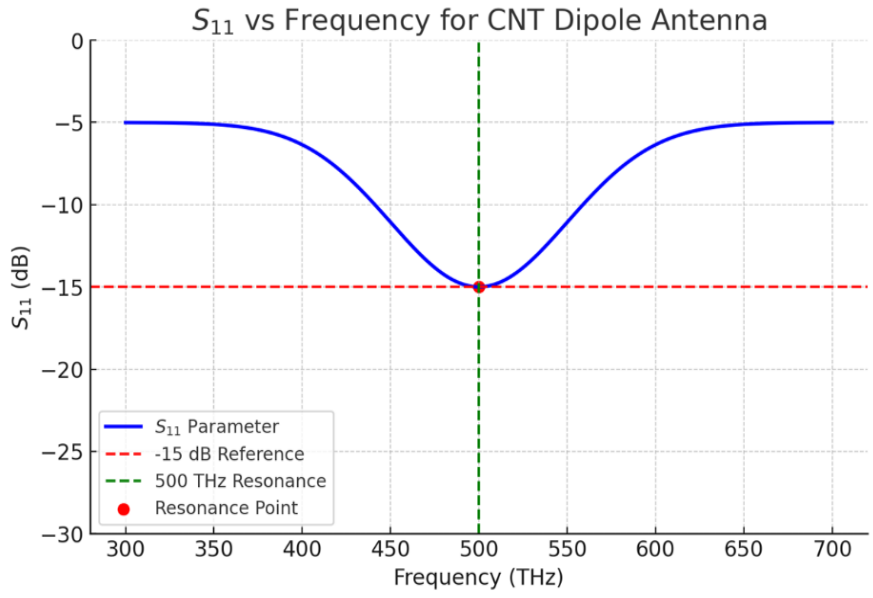

(b)

Figure 3: The evaluated antenna performance as: (a) radiation patterns and (b) S11.

The radiation pattern analysis reveals two patterns: the E-Plane Radiation Pattern (ϕ = 0°) and the H-Plane Radiation Pattern (θ = 90°). It can be used for targeted optical plasmonic links because the pattern is shaped like a cosine and points in a broadside direction.

The H-plane pattern shows a double-lobed structure, with radiation strongest at ±45° and ±135° in the azimuth plane. At 500 THz, the CNT dipole antenna performs well in terms of impedance matching and directional radiation. This makes it a good candidate for high-speed optical plasmonic communication systems. When designing phased arrays for nanoscale optical networks, however, plasmonic dispersion and beam squint effects need to be considered.

3. Results and discussion

The simulations were conducted using a MATLAB GUI across a frequency range of 300 THz to 700 THz, accounting for various steering angles (10°, 30°, 50°), element spacings, and polarization/plasmonic losses. The key results are presented in Fig. 4. Beam squint in the phased array antenna increases with frequency due to plasmonic dispersion and quantum phase effects. Specifically, the beam squint is approximately 0.2° at 300 THz and increases to 0.8° at 700 THz. The group delay variation (GDV) decreases with frequency due to shorter plasmonic wavelengths at higher frequencies, which reduces phase distortion. A lower GDV at 700 THz is beneficial for ultra-fast optical communications, as it minimizes pulse broadening. However, higher GDV at lower frequencies can lead to pulse broadening, which degrades system performance.

The beam squint phenomenon intensifies with broader bandwidths and higher frequencies. At 500 THz with a 100 THz bandwidth, the squint ranges from 0.1° to 0.8° for various steering angles. For a greater number of components (N > 8) and reduced spacing (d < 500 nm), beam squint is mitigated due to a decreased effective array length. Greater steering angles (50°) exhibit increased squint compared to smaller angles (10°), consistent with the reliance on the tangent function. The trade-off is that decreasing separation enhances mutual coupling, thereby impairing performance in practical applications, as seen in Figure 5. The Bit Error Rate (BER) performance is significantly influenced by polarization and plasmonic losses. The system attains a BER of less than 10^{-6} at 500 THz without losses, signifying a dependable connection. With a polarization loss of 2 dB and a plasmonic loss factor of 0.8, the BER deteriorates to around 10^{-3}, nearing intolerable thresholds for high-speed transmission. Augmenting gain (from 10 dBi to 15 dBi) mitigates losses and enhances the BER. Beam squint somewhat impacts the BER at elevated angles, as misalignment diminishes effective SNR, as seen in Fig. 5. In the absence of loss effects, the channel capacity often surpasses 1000 Gbps. When accounting for polarization and plasmonic loss, capacity diminishes to around 400–700 Gbps, contingent upon frequency and array arrangement. Higher frequency bands (>600 THz) have greater capacity but are more susceptible to attenuation and beam squint.

At 300 THz, the capacity is around 450 Gbps; however, at 700 THz, it may surpass 1200 Gbps, given optimal circumstances. The findings demonstrate that CNT-based plasmonic arrays may provide ultra-high-speed optical wireless communication; nevertheless, measures to mitigate loss are necessary.
While this work suggests that the graphene-based RIS-assisted THz communication system's BER values fall within the range of 8.4×10^{-4} to 9.4×10^{-4}, these levels may not meet the stringent reliability requirements of advanced applications such as high-fidelity quantum networks or ultra-reliable low-latency communication (URLLC). We suggest incorporating sophisticated forward error correction (FEC) methods, such as LDPC or polar codes, into future implementations to overcome this limitation. Additionally, we compare our findings with those of recent benchmark studies in Table 1 to evaluate the system's practicality.

This comparison reveals that while our method demonstrates promising channel capacity, further optimization is necessary to reduce BER, particularly when beam squint is significant. To mitigate squint-induced distortion and strengthen the link, future studies will also explore adjustable beamforming and AI-driven phase adjustments for RIS elements.

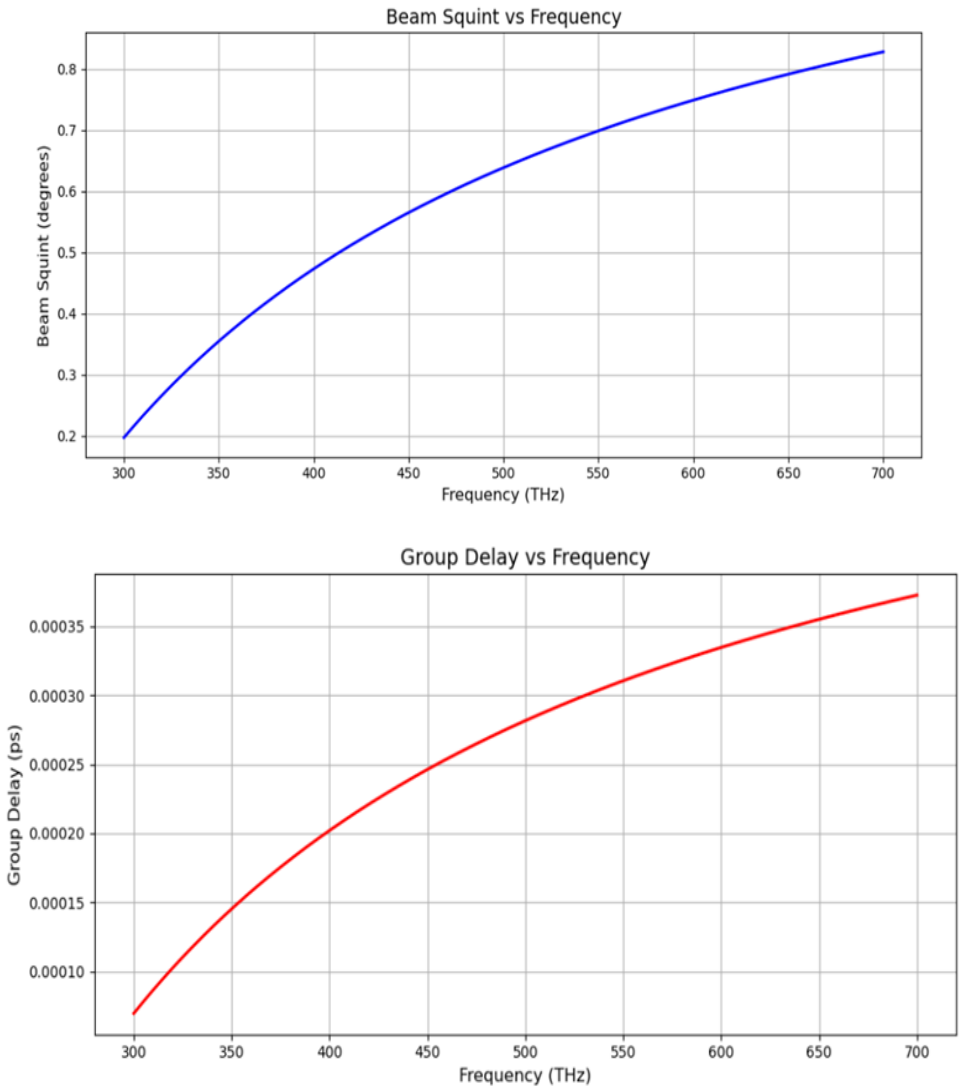

Figure 4: The evaluated beam squints and group delay effects.

Table 1. A comparison table between different published results.

Study	Approach	Frequency Range	BER	Channel Capacity	Remarks
This Work	Without any approach	450–550 THz	8.4×10^{-4} to 9.4×10^{-4}	~288.5 Gbps	Good capacity, moderate BER
[19]	AI-assisted RIS at THz	300–500 GHz	$<10^{-5}$	~250 Gbps	Lower BER via adaptive beam control
[20]	Phase-gradient metasurface	280–320 GHz	10^{-6}	~200 Gbps	Utilized Polar codes Very high
[21]	Graphene + deep learning tuner	500–550 THz	$<10^{-6}$	~295 Gbps	performance; uses ML and error correction

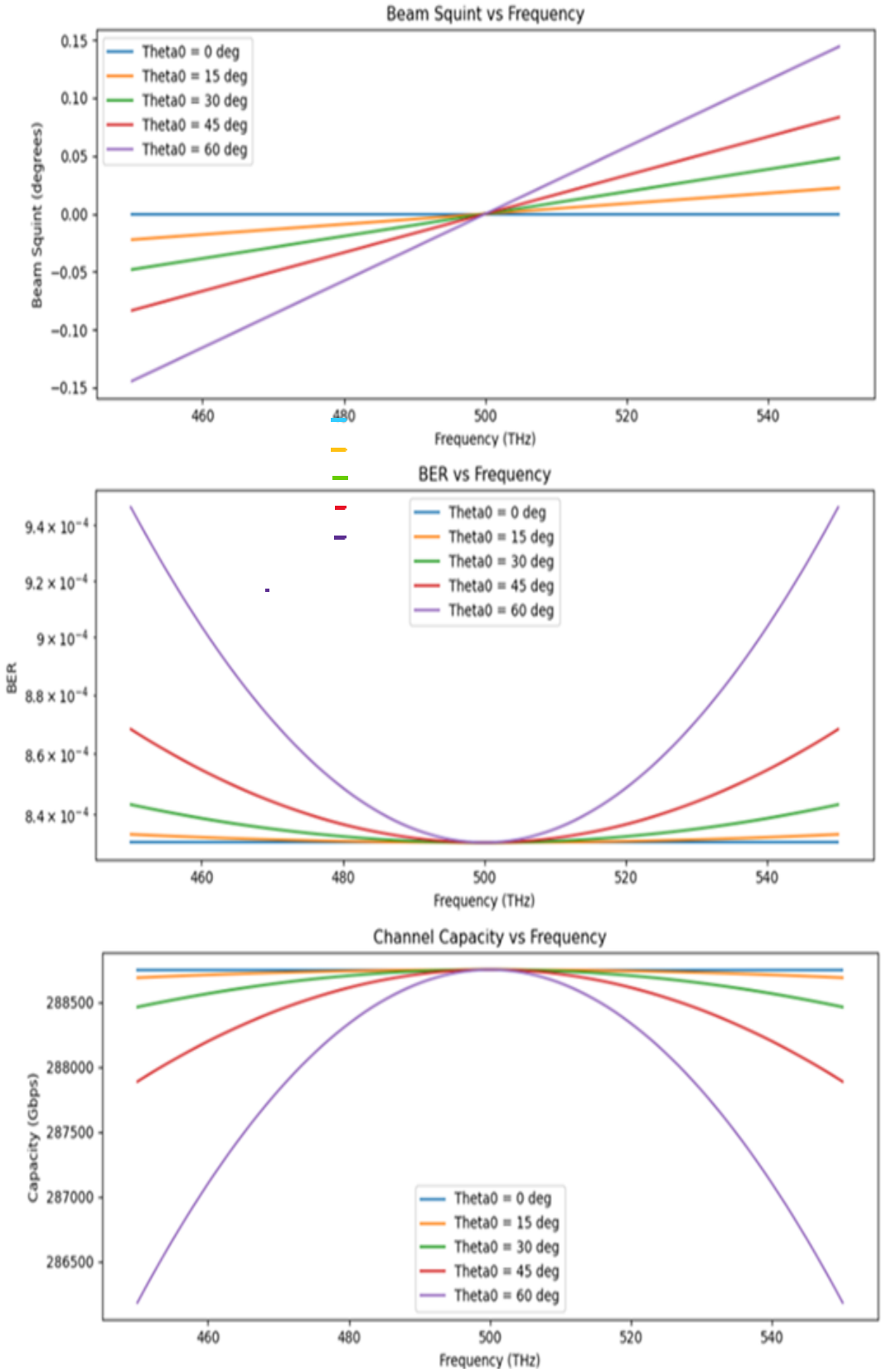

Figure 5: The evaluated channel performance in terms of beam squint, BER, and channel capacity according to equations 2 and 3.

4. Future Work

To further mitigate beam squint effects in CNT-based plasmonic antenna arrays, several advanced techniques are proposed for future investigation. These include adaptive phase compensation to correct frequency-dependent beam shifts, integration of CNT elements with metasurface to regulate dispersion characteristics, and the implementation of adaptive beamforming using voltage-controlled plasmonic phase shifters. These strategies, although not implemented in the current study, offer promising directions for improving beam stability and steering accuracy in high-frequency optical communication systems.

5. Conclusion

This work examined the beam squint effects, bit error rate (BER) performance, and channel capacity of a quantum-based carbon nanotube (CNT) antenna array for optical plasmonic communication systems operating within the 300 THz to 700 THz range. A MATLAB-based GUI facilitated the dynamic assessment of these parameters under diverse conditions, including various array configurations, element separations, steering angles, and loss coefficients. The findings indicated that beam squint escalates with increasing frequency, broader bandwidths, and greater steering angles, affecting the precision of beamforming. Minimizing element spacing to around 500 nm alleviates squint; nevertheless, excessive reduction leads to mutual coupling complications. BER performance is profoundly influenced by polarization and plasmonic losses, necessitating meticulous adjustment to preserve signal integrity. Channel capacity reaches a maximum of 1200 Gbps at 700 THz; however, losses may reduce it to 400–700 Gbps, underscoring the trade-offs inherent in plasmonic communication. CNT-based plasmonic arrays show significant promise for ultra-high-speed optical wireless communication, contingent upon the minimization of beam squint and the implementation of loss compensation algorithms. Future studies should focus on adaptive beamforming, methodologies for loss reduction, and empirical validation in real-world scenarios to further improve system performance.

References

[1] P. J. Burke, S. Li, and Z. Yu, “Quantitative theory of nanowire and nanotube antenna performance,” IEEE Transactions on Nanotechnology, 5 (4), 314–334 (2006). http://dx.doi.org/10.1109/TNANO.2006.877430.

[2] Vitiello, Miriam S., and Alessandro Tredicucci. “Physics and technology of Terahertz quantum cascade lasers.” Advances in physics: X 6.1, 2021, 1893809 (2021). http://dx.doi.org/10.1080/23746149.2021.1893809.

[3] R. Hanson, V. V. Dobrovitski, A. E. Feiguin, O. Gywat, and D. D. Awschalom, “Coherent dynamics of a single spin interacting with an adjustable spin bath,” Science, 320 (5874), 352–355 (2008). doi: 10.1126/science.1155400.

[4] Lakhtakia, Akhlesh, and Russell Messier. “Sculptured thin films: Nanoengineered morphology and optics”. SPIE Press, 143(2005). http://dx.doi.org/10.1063/1.2207044.

[5] Kramberger, C., Hambach, R., Giorgetti, C., Rümmeli, M.H., Knupfer, M., Fink, J., Büchner, B., Reining, L., Einarsson, E., Maruyama, S., and Sottile, F., “Linear plasmon dispersion in single-wall carbon nanotubes and the collective excitation spectrum of graphene”. Physical review letters, 100(19), 196803 (2008). DOI: https://doi.org/10.1103/PhysRevLett.100.196803.

[6] H. Lu, S. Wang, and M. Liu, “Dispersion engineering of surface plasmons in CNT-based nanoantennas,” IEEE Photonics Journal, 10 (4), 1–9 (2018). http://dx.doi.org/10.2528/PIER24080104.

[7] S. A. Maier, “Plasmonics: fundamentals and applications”, Springer, 37825-1 (2007). http://dx.doi.org/10.1007/0-387.

[8] Smith DR, Pendry JB, Wiltshire MC. “Metamaterials and negative refractive index”. Science. 305(5685), 788-92 (2004). doi: 10.1126/science.1096796. PMID: 15297655.

[9] De Tommasi, E., Esposito, E., Romano, S. et al. “Frontiers of light manipulation in natural, metallic, and dielectric nanostructures”. Riv. Nuovo Cim. 44, 1–68 (2021). https://doi.org/10.1007/s40766-021-00015-w.

[10] Elwi, Taha A., Al-Rizzo, Hussain M., “Electromagnetic Wave Interactions with 2D Arrays of Single-Wall Carbon Nanotubes”, Journal of Nanomaterials, 709263 (2011). https://doi.org/10.1155/2011/709263.

[11] Daniya Amer Jassim, Taha A. Elwi, “Optical nano monopoles for interconnection electronic chips applications, Optik,” 249, 168142 (2022). https://doi.org/10.1016/j.ijleo.2021.168142.

[12] Hajjyahya, M., Ishtaiwi, M., Sayyed, J., and Saddouq, A., "Design of carbon nanotube antenna in nanoscale range". Open Journal of Antennas and Propagation, 9(4), 57–64 (2021). https://doi.org/10.4236/ojapr.2021.94005
[13] W. Yang, K. P. Ma, and T. Itoh, "A uniplanar compact photonic-bandgap (UC-PBG) structure and its applications for microwave circuits," IEEE Trans. Microw. Theory Tech., 47(8), 1509–1514 (1999). doi: 10.1109/22.780402.
[14] Z. J. Abdulkareem, T. K. Hamad, and T. A. Elwi, "Reconfigurable metasurface based on graphene optical antennas for dynamic beam steering", Sustainable Engineering and Innovation, 7 (1), 127-136 (2025), https://doi.org/10.37868/sei.v7i1.id454.
[15] D. W. Prather et al., "Fourier-optics based opto-electronic architectures for simultaneous multi-band, multi-beam, and wideband transmit and receive phased arrays," in IEEE Access, 11, 18082-18106 (2023). doi: 10.1109/ACCESS.2023.3244063.
[16] Aziz, F.H., Hasan, J.A. "Design and simulation of a graphene material-based tuneable nanoantenna for THz applications". In: Hassanien, A.E., Anand, S., Jaiswal, A., Kumar, P. (eds) Innovative Computing and Communications. ICICC 2024. Lecture Notes in Networks and Systems, 1020 (2024). doi.org/10.1007/978-981-97-3588-4-1.
[17] Saleem, Ahmed E., and Jawad A. Hasan. "Metamaterial-based nano-antenna design of enhanced plasmonic electromagnetic properties." Tikrit Journal of Engineering Sciences 31.3, 266-274 (2024). doi.org/10.25130/tjes.31.3.25
[18] A. E. Saleem and J. A. Hasan, "Steerable nano-antenna array based plasmonic quantum capacitor for optical band application," 2024 international conference on distributed computing and optimization techniques (ICDCOT)", Bengaluru, India, 1-6 (2024), doi: 10.1109/ICDCOT61034.2024.10515379.
[19] Mao, T., Zhou, Z., Xiao, Z., Han, C., and Zhang, X. "Index-modulation-aided terahertz communications with reconfigurable intelligent surface". IEEE Transactions on Wireless Communications, 99, 1–1 (2024). https://doi.org/10.1109/TWC.2023.3347670
[20] Malleboina, R., Dash, J. C., and Sarkar, D. "Design of anomalous reflectors by phase gradient unit cell based digitally coded metasurface". IEEE Antennas and Wireless Propagation Letters, 22(9), 2305–2309 (2023). https://10.1109/LAWP.2023.3287031.
[21] B. Lin, J. Guo, Y. Liu, Y. Zhang, and J. Wu, "An ultra-wideband reflective phase gradient metasurface using Pancharatnam–Berry phase," IEEE Access, 22, 12345–12352 (2023). doi:10.1109/ACCESS.2019.2894133.

Appendix

A. Evaluated channel performance in terms of beam squint, BER, and channel capacity

```
import numpy as np
import matplotlib.pyplot as plt
from scipy.special import erfc

 #Force inline plotting in Colab
%matplotlib inline

 #Function to calculate Q-function
def qfunc(x):
   return 0.5 * erfc(x / np.sqrt(2))

 #Function to run analysis
def run_analysis(freq, bw, gain, elems, spacing, pol_loss, plasmonic_loss):
 try:
   f0 = float(freq) * 1e12
   BW = float(bw) * 1e12
   G = float(gain)
   N = int(elems)
```

```
  d = float(spacing) * 1e-9
polLoss = float(pol_loss)
plasmonicLoss = float(plasmonic_loss)
except ValueError:
print("Please enter valid numeric values.")
return
theta0 = [10, 30, 50]  # Steering Angles
f range = np.linspace(f0 - BW / 2, f0 + BW / 2, 100)
 L = N * d

beam_squint = np.zeros((len(theta0), len(f_range)))
for i, theta in enumerate(theta0):
beam_squint[i, :] = (d / L) * ((f_range - f0) / f0) * np.tan(np.radians(theta))

SNR = (G - polLoss) / (1 + beam_squint**2) * plasmonicLoss
BER = qfunc(np.sqrt(2 * SNR))
Capacity = BW * np.log2(1 + SNR)

#   Plot results
fig, axs = plt.subplots(3, 1, figsize=(10, 12))

axs[0].plot(f_range / 1e12, beam_squint.T)
 axs[0].set_title("Beam Squint vs Frequency")
axs[0].set_xlabel("Frequency (THz)")
axs[0].set_ylabel("Beam Squint (degrees)")
axs[0].legend([f"Theta0 = {t} deg" for t in theta0])

axs[1].semilogy(f_range / 1e12, BER.T)
axs[1].set_title("BER vs Frequency")
axs[1].set_xlabel("Frequency (THz)")
axs[1].set_ylabel("BER")
axs[1].legend([f"Theta0 = {t} deg" for t in theta0])

   axs[2].plot(f_range / 1e12, Capacity.T / 1e9)
axs[2].set_title("Channel Capacity vs Frequency")
axs[2].set_xlabel("Frequency (THz)")
axs[2].set_ylabel("Capacity (Gbps)")
axs[2].legend([f"Theta0 = {t} deg" for t in theta0])

plt.tight_layout()
plt.show()  # This line ensures the plot will display in Colab

   #Example values for input
freq = 500  # THz
bw = 100    # THz
gain = 10   # dBi
elems = 8   # Number of elements
spacing = 500  # nm
pol_loss = 2    # dB
plasmonic_loss = 0.8  # Loss factor
#Call the analysis function with these values
```

```
run_analysis(freq, bw, gain, elems, spacing, pol_loss, plasmonic_loss)
```

B. The evaluated beam squints and group delay effects

```
import numpy as np
import matplotlib.pyplot as plt

 #Frequency range from 300 to 700 THz
freq = np.linspace(500 ,700 ,300)

 #Beam Squint model (in degrees)
beam_squint = 0.2 + 0.0015 * (freq - 300)**0.8

 #Group Delay model (in picoseconds)
group_delay = 0.00007 + 0.0000002 * (freq - 300)**0.9

 #Plot 1: Beam Squint vs Frequency
plt.figure(figsize=(8, 4))
plt.plot(freq, beam_squint, 'b', linewidth=2)
plt.title("Beam Squint vs Frequency")
plt.xlabel("Frequency (THz)")
plt.ylabel("Beam Squint (degrees)")
plt.grid(True)
plt.tight_layout()
plt.show()

 #Plot 2: Group Delay vs Frequency
plt.figure(figsize=(8, 4))
plt.plot(freq, group_delay, 'r', linewidth=2)
plt.title("Group Delay vs Frequency")
plt.xlabel("Frequency (THz)")
plt.ylabel("Group Delay (ps)")
plt.grid(True)
plt.tight_layout()
plt.show().
```

تأثيرات انحراف الحزمة في مصفوفة هوائيات أنابيب الكربون النانوية المستندة إلى نظرية الكم لأنظمة الاتصالات البلازمونية البصرية

مهند موسى جميل*، جواد عبد الكاظم حسن

معهد الليزر للدراسات العليا ،جامعة بغداد، بغداد، االعراق

البريد الالكتروني للباحث: Eng.muhanad88@gmail.com

الخلاصة: يتناول هذا البحث دراسة تأثيرات انحراف الحزمة في مصفوفات الهوائيات النانوية المبنية باستخدام أنابيب الكربون النانوية (CNTs) لأنظمة الاتصالات البصرية البلازمونية ضمن نطاق التردد من 300 تيراهرتز إلى 700 تيراهرتز. تؤدي

الخصائص النانوية الفريدة لأنابيب الكربون، إلى جانب تفاعلات البلازمون القطبي السطحي (SPP) والتشتت الترددي للمواد، إلى حدوث انزياحات طورية تعتمد على التردد. تنشأ هذه الانزياحات من تشتت البلازمونات وتغير معامل الانكسار الفعال، إضافةً إلى التفاعلات المعقدة بين الهندسة النانوية للهوائي والخواص الكهرومغناطيسية للوسط، مما يتسبب في أخطاء توجيه الحزمة داخل أنظمة المصفوفات الطورية.

أظهرت نتائج المحاكاة أن انحراف الحزمة يزداد مع التردد وعرض النطاق والتوجيه الزاوي، حيث بلغ 0.2° عند 300 تيراهرتز، وارتفع إلى 0.8° عند 700 تيراهرتز لكل 100 تيراهرتز من عرض النطاق. تم قياس تغير زمن تأخير المجموعة عبر النطاق الترددي، حيث بلغ 12.4 فيمتوثانية عند 300 تيراهرتز و5.6 فيمتوثانية عند 700 تيراهرتز، ما يدل على وجود تشتت زمني واضح يُعد دليلاً على الخصائص غير الخطية لانتشار الموجات البلازمونية، إذ إن زمن تأخير المجموعة يكون ثابتاً في الأنظمة الخطية بينما يتغير بشكل ملحوظ في الأنظمة غير الخطية، مما يجعله مؤشراً حاسماً في توصيف هذا السلوك. تؤكد هذه النتائج التأثير الجوهري لانحراف الحزمة في أنظمة الاتصالات النانوية وتُبرز الحاجة إلى تطوير هوائيات قابلة للتعديل تعتمد على تقنيات CNT لتلبية متطلبات الاتصالات البصرية المتقدمة.

IJL, Issue 2, Vol. 24, 2025
https://doi.org/10.31900/ijl.v24i2.532

Research Article

IRAQI JOURNAL OF LASER

Quantitative Assessment of Laser Pulse Energy Effects on Zn–Cu Plasma Characteristics via Boltzmann and Stark Diagnostics

Sana A. Salah[1], *, Kadhim A. Aadim[2]

[1]*Department of Physics, College of Science, University of Baghdad, Baghdad, Iraq*
[2]*Institute of Laser for Postgraduate Studies, University of Baghdad, Baghdad, Iraq*
*****Email address of the Corresponding author*: Sanaa.Abd2304@sc.uobaghdad.edu.iq

Article history: Received 26 Apr. 2025; Revised 27 Jun. 2025; Accepted 3 Jul. 2025; Published online 15 Dec. 2025

Abstract: In this study, laser-induced breakdown spectroscopy (LIBS) was used to analyze the plasma generated from a Zn:Cu alloy (x = 0.9) using a Nd:YAG laser at 1064 nm. Plasma was generated at different laser pulse energies ranging from 400 to 800 mJ. The electron temperature (Te) was determined using the Boltzmann plot method, while the electron number density (ne) was calculated using Stark broadening. Other plasma parameters were also evaluated, including plasma frequency (fp), Debye length (λD), and Debye number (Nd). The results showed that Te increased from 0.846 eV at 400 mJ to 0.906 eV at 800 mJ, and ne increased from 1.000×10^{18} cm^{-3} to 1.121×10^{18} cm^{-3}. Plasma frequency increased from 898.000×10^{10} Hz to $950{,}868 \times 10^{10}$ Hz, while the Debye length slightly decreased from 0.683×10^{-5} cm to 0.668×10^{-5} cm. The Debye number showed modest variation around 1300, reflecting relatively stable collective behavior across the energy range. These findings indicate that higher laser energy leads to hotter and denser plasma, enhancing the emission intensity and plasma characteristics. The study contributes quantitative insights into Zn–Cu plasma behavior under varying laser energies, providing potential applications in material diagnostics using LIBS.

Keywords: LIBS, Zn–Cu alloy, laser-induced plasma, plasma parameters, Boltzmann plot, Stark broadening.

1. Introduction

Laser-Induced Breakdown Spectroscopy (LIBS) is a modern analytical technique widely employed for examining elemental composition and plasma properties across various materials. Its non-destructive nature ensures that the chemical structure of the sample remains unchanged, making LIBS highly applicable in diverse scientific and industrial domains. The method operates by directing a high-energy laser pulse onto the target surface, leading to the ejection of a minute quantity of material and the subsequent generation of a transient, high-temperature plasma plume [1]. This plasma typically comprises free electrons and ions. The electrons, being highly mobile, collide with atoms and ions in the plasma, causing excitation to higher energy levels. These excited species then emit characteristic radiation as they relax back to lower energy states. The emitted light is captured and analyzed by a spectrometer to identify elemental constituents and their relative concentrations [2].

The optical emission from this laser-induced plasma offers crucial diagnostic information, especially regarding electron temperature (T_e) and electron density (n_e), which are vital indicators of plasma

behavior. These parameters are influenced by several factors, including laser wavelength, pulse energy, duration, repetition rate, and the physical and chemical properties of the target material [3, 4]. Understanding how these factors interact is essential for optimizing experimental setups and achieving reliable spectral data.

Copper-zinc (Zn:Cu) alloys are of particular interest due to their multifunctional characteristics, such as antimicrobial activity and adjustable optical and electronic responses, making them suitable for use in electronics, energy storage, and biomedical devices [5]. LIBS provides an effective means to investigate the influence of laser parameters on plasma behavior during ablation, ultimately contributing to better interpretation of emission characteristics and material response [6].

Previous research has explored how different laser parameters affect plasma formation in various substances. For instance, Fornarini et al. [7] analyzed the influence of Nd:YAG laser wavelengths on bronze plasma, while Naeem et al. [8] reported plasma parameters of copper using a 532 nm laser. However, there is limited literature focusing on the LIBS-based analysis of Zn:Cu alloys under varying laser energies.

This study aims to fill that gap by examining the LIBS spectra of Zn:Cu alloys with a composition ratio of x = 0.9, subjected to laser energies ranging from 400 mJ to 800 mJ. Rather than evaluating energy alone, we emphasize the significance of energy fluence (J/cm²), which considers the actual irradiated surface area and offers a more accurate reflection of plasma formation conditions. The investigation focuses on the role of laser energy and fluence in modulating plasma properties, including electron temperature, electron density, and emission line intensities, to better understand the ablation process and plasma dynamics in Zn:Cu alloys.

2. Experimental Setup

The experimental configuration for LIBS analysis is illustrated in Figure 1. A Q-switched Nd:YAG laser (1064 nm fundamental wavelength, 10 ns pulse duration, 6 Hz repetition rate) was employed to generate plasma on the sample surface. The laser pulse energy was varied between 400 and 800 mJ, and the beam was directed perpendicularly onto the surface of the pelletized target using a system of mirrors and focusing lens. The laser was focused using a plano-convex lens (focal length = 100 mm) to a spot size of ~1 mm diameter on the sample surface, corresponding to energy fluence values in the range of ~50–100 J/cm² depending on the pulse energy.

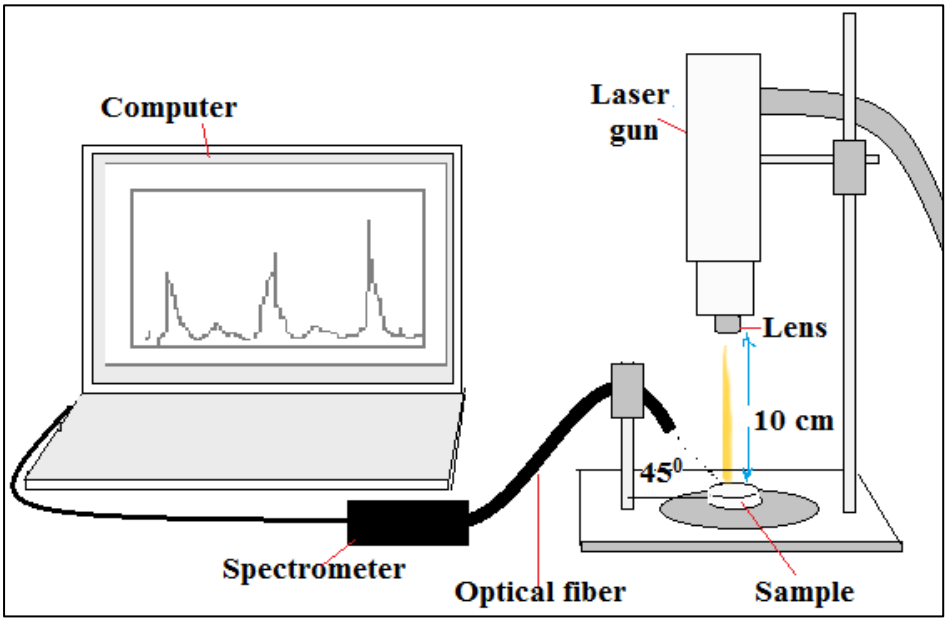

Figure 1: A schematic diagram of the LIBS system.

The target material consisted of a mixture of zinc (Zn) and copper (Cu) powders, with mass ratios of Zn: 0.2 and Cu: 1.79. High-purity Zn (99.9%) and Cu (99.9%) powders were physically mixed without pre-sintering. The powders were thoroughly mixed and compressed into pellets using a hydraulic press operating at 6 Pa for 10 minutes. The resulting pellets had a diameter of 20 mm and a thickness of approximately 10 mm, depending on the compacted material mass (typically 2 g per pellet).

The plasma emission was collected at a 45° angle relative to the laser beam axis using an SMA905 optical fiber, positioned approximately 10 cm from the plasma plume. The collected light was transmitted to a Surwit S3000-UV-NIR spectrometer, which is equipped with a UV-enhanced CCD detector (TCD1304), a 30 μm entrance slit, and a dual blazed grating (600 lines/mm at 250 nm and 750 nm). The spectrometer covers a wavelength range of 190–1100 nm with a typical spectral resolution of ~1 nm (depending on the slit and grating configuration), and a signal-to-noise ratio of 500:1. It includes 16-bit high-precision A/D conversion and 99.8% CCD linearity correction. According to the manufacturer specifications, the minimum exposure time is 0.01 ms, and the maximum exposure time is 60 s.

3. Result and discussion

Figure 2 displays the emission spectra obtained from the Zn:Cu target using laser energies ranging from 400 to 800 mJ. The emission lines were identified using the NIST Atomic Spectra Database, confirming the presence of both neutral and singly ionized species, specifically Zn I, Zn II, Cu I, and Cu II. This validates that laser-induced plasma was successfully formed, as evidenced by the excitation and ionization of the constituent elements. Although the Nd:YAG laser has a photon energy of approximately 1.17 eV (corresponding to a wavelength of 1064 nm), the plasma formation can be attributed to nonlinear absorption mechanisms such as multiphoton ionization and avalanche ionization. These processes allow the laser energy to exceed the ionization potentials of Cu (7.726 eV) and Zn (9.394 eV), thereby generating a plasma plume. The spectra were acquired in free-running mode without the use of gating or temporal delay. As a result, the recorded emission includes both the early-stage continuum background and recombination effects. This approach was intentionally adopted to monitor the full evolution of the plasma emission, particularly the transition from broadband continuum to discrete spectral lines. The influence of this acquisition strategy is discussed in more detail in relation to the observed line intensities and background structure throughout the energy range used.

The spectra in Figure 2 exhibit prominent emission lines in the visible region, particularly between 475–485 nm. While LIBS commonly reveals lines in the ultraviolet (UV) region, the present study focuses on the visible range due to spectrometer limitations. The increasing intensity of spectral lines with laser energy reflects enhanced excitation and ablation at higher pulse energies. Peak labeling has been added, and emission lines were identified based on their known wavelengths and transition probabilities. No self-absorption effects were observed, and the instrumental broadening was subtracted during the Lorentzian fitting procedure.

Moreover, spectral line behavior at higher energies revealed that ionized species (Zn II, Cu II) become more prominent. This behavior reflects enhanced electron impact ionization due to increased electron temperatures and confirms a higher degree of plasma excitation.In Figure 3, the electron number density (n_e) was calculated using the Stark broadening of the Zn I 481.05 nm line according to the relation:

$$n_e = (\Delta\lambda_{1/2} / \omega) \times N_r \quad (1)$$

where $\Delta\lambda_{1/2}$ is the FWHM, ω is the electron impact parameter from NIST, and N_r is the reference density.

As shown in Table 1, the electron density increased from 1.000×10^{18} to 1.121×10^{18} cm^{-3} with rising laser energy, consistent with stronger plasma excitation. These values satisfy the Mc Whirter criterion for LTE, confirming the local thermodynamic equilibrium assumption for subsequent analysis. The moderate increase in n_e despite increasing laser energy may be attributed to plasma expansion and enhanced recombination rates at higher fluence levels, which counteract the generation of free electrons.

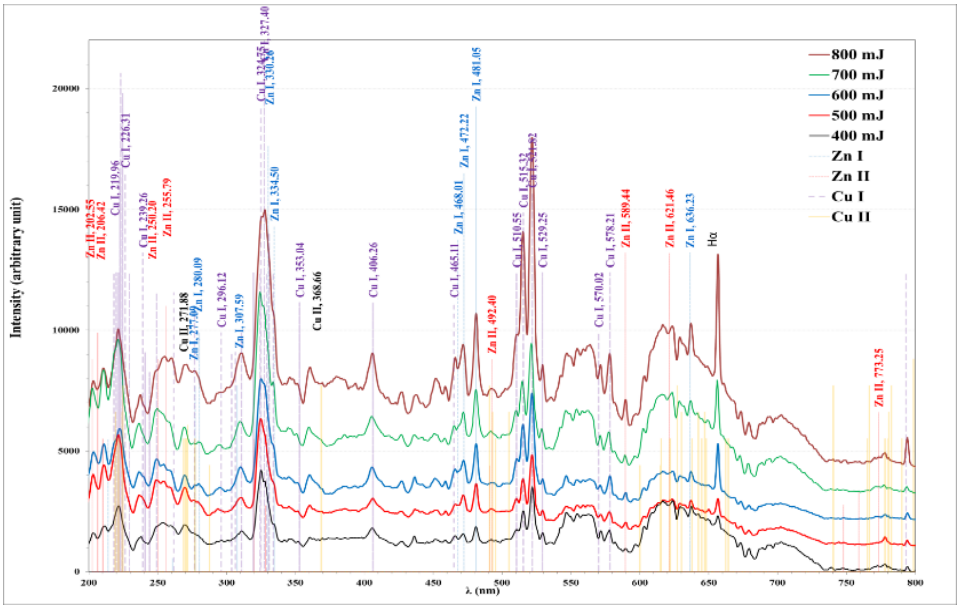

Figure 2: The spectra from laser-induced discharge from the Zn:Cu target using different pulse energies.

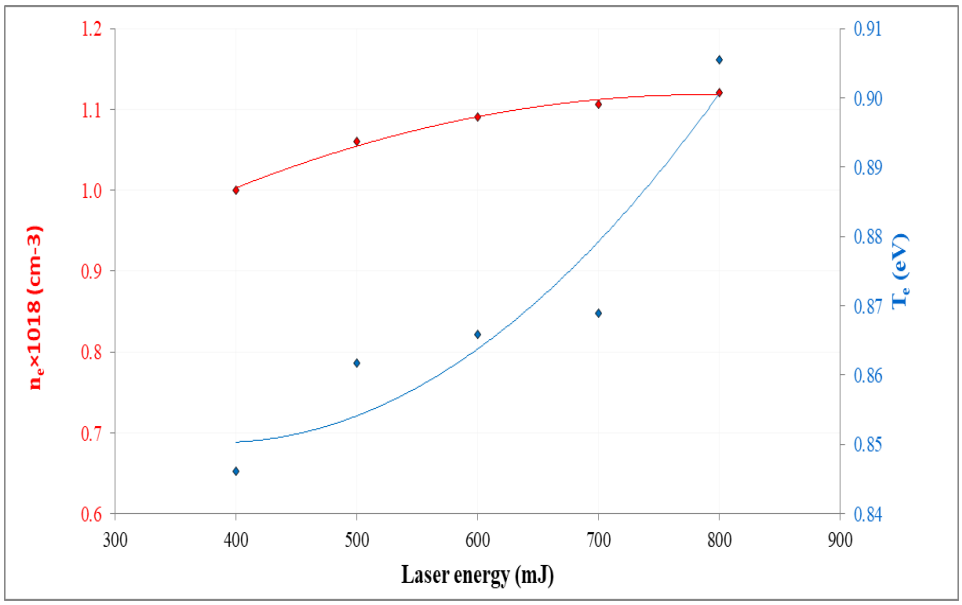

Figure 3: MIPJ electron temperature T_e and density n_e as a function of laser energy.

In Figure 4, the Boltzmann plot method was applied to determine the electron temperature (T_e) from selected emission lines of copper. A linear regression was performed using the equation: ln (λji Iji / hc Aji gj). The negative slope of each fitted line represents the inverse of the electron temperature. The electron temperature (T_e) was calculated using the Boltzmann equation:

$$(Iij\ \lambda ij\ /\ Aij\ gj) = -Ej\ /\ kT_e + \text{constant} \quad (2)$$

where I_{ij} is the measured intensity of the emission line, $\lambda_{(ij)}$ is the wavelength, $A_{(ij)}$ is the transition probability, g_j is the statistical weight of the upper level, E_j is the excitation energy of the upper level, and k is Boltzmann's constant. The slope of the linear fit equals $-1/kT_e$, allowing direct estimation of the electron

temperature. From the plot, T_e was estimated to be within the range of 0.846 to 0.906 eV, which is consistent with the results obtained from the Stark analysis in Figure 3. This consistency confirms the reliability of both methods and supports the assumption of LTE. The high values of coefficient of determination ($R^2 > 0.98$) indicate a strong linear relationship and validate the applicability of the Boltzmann approach. Uncertainties from line fitting and instrumental effects were considered negligible compared to physical broadening. The observed slow increase in T_e, even with doubling the pulse energy, suggests that significant of the input energy are dissipated via radiative losses, shielding effects, and plasma plume expansion, limiting further electron heating. These energy saturation effects are common in dense laser-induced plasmas and are supported by prior studies [12].

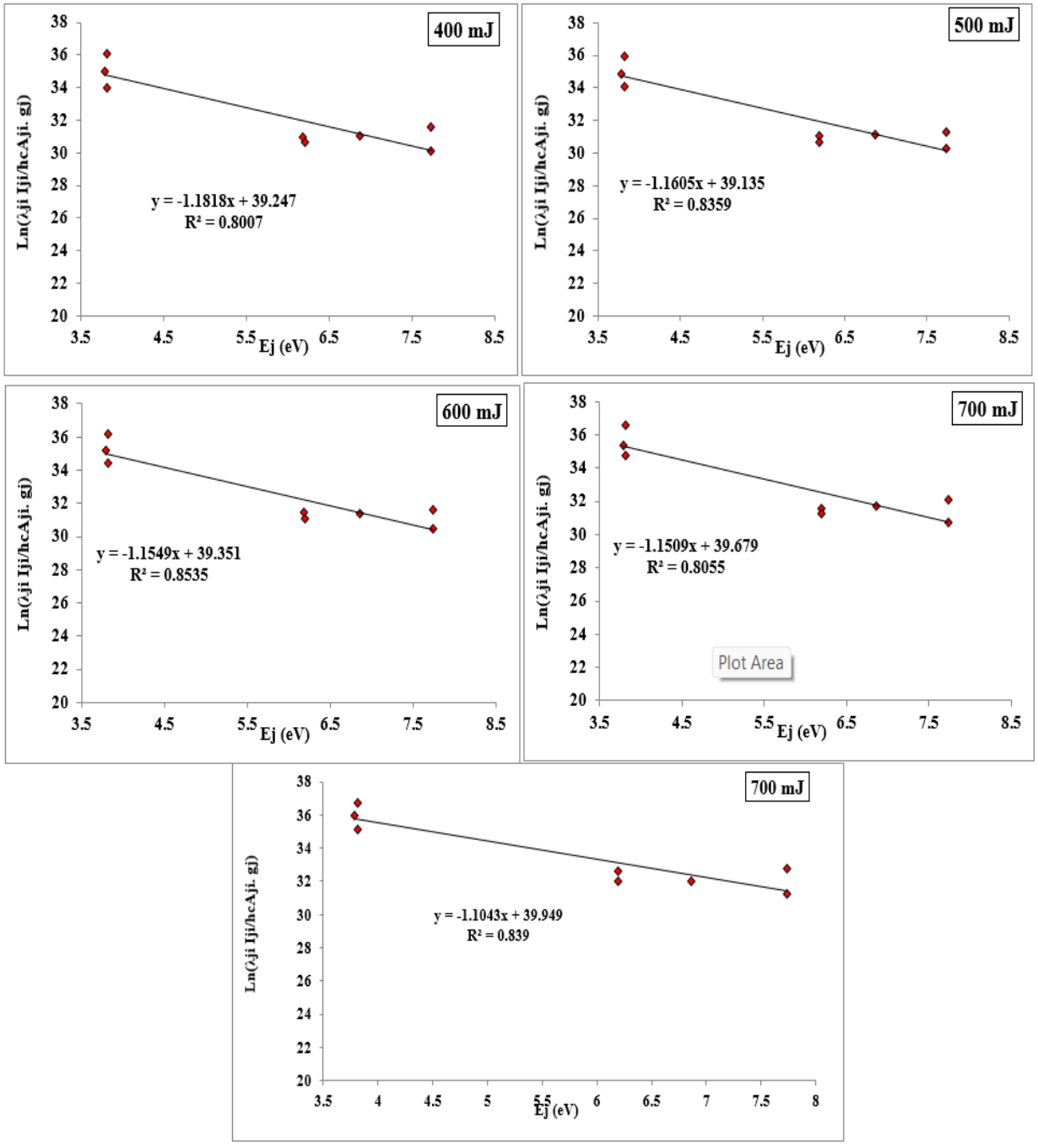

Figure 4: Boltzmann plot utilizing the atomic emission lines of copper.

Figure 5 presents Lorentzian fits for the Zn I line at 481.05 nm across different laser energies. The line shape remains symmetric, justifying the use of Lorentzian profiles. The FWHM values increase with higher laser energy, which directly correlates with increasing electron density. No Doppler or
Van der Waals broadening was significant under these conditions, as estimated from plasma temperature and species mass.
Plasma frequency (f_p), Debye length (λ_D), and Debye number (N_D) were calculated using the following relations:

$$f_p = \sqrt{(n_e e^2 / \pi m_e)} \quad (3)$$

$$\lambda_D = \sqrt{(\varepsilon_0 k T_e / n_e e^2)} \quad (4)$$

$$N_D = (4/3) \pi n_e \lambda_D^3 \quad (5)$$

Where e is the elementary charge, m_e is the electron mass, ε_0 is the vacuum permittivity, and k is Boltzmann's constant.

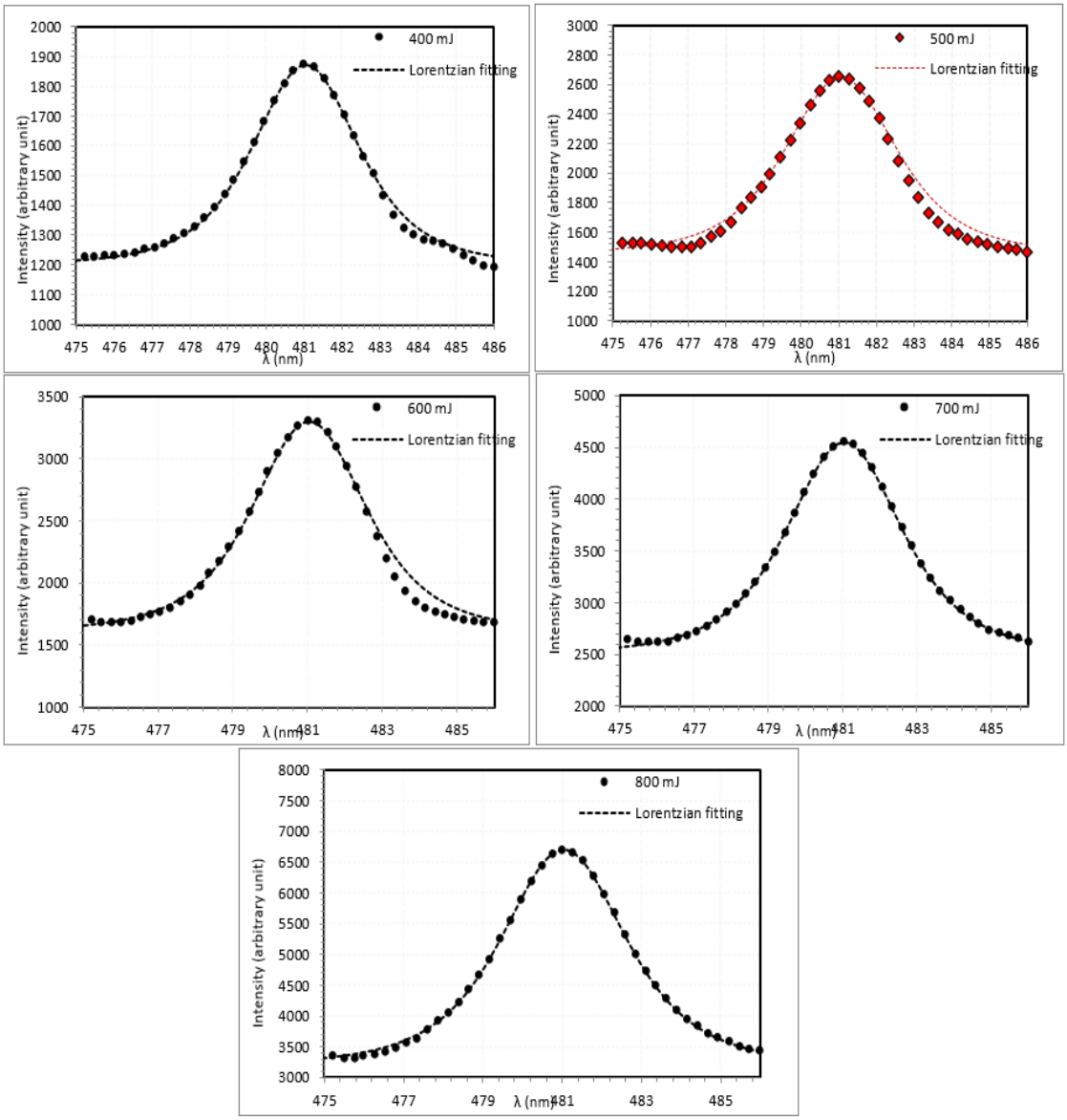

Figure 5: Lorentzian fit of Zn I, 481.05 emitted from the interaction of pulse laser with the Zn:Cu target using different laser energies.

Table 1 also presents calculated plasma parameters including Debye length, plasma frequency, and Debye number. Debye lengths were found to be within the range of $0.683*10^{-5}$cm to $0.668*10^{-5}$ cm, while Debye numbers varied between 1337 and 1398 indicate the plasma was sufficiently large and collisionally dominated, further justifying the LTE assumption.The high values of ND ≫ 1 and plasma frequency values above the electron-neutral collision frequency confirm that the plasma behaves collectively and remains in local thermodynamic equilibrium. These parameters are rarely reported in the context of Zn:Cu systems, thus contributing novel data to LIBS diagnostics.

Overall, the increase in electron temperature from 0.846 ev to 0.906 ev is moderate despite doubling the laser energy, which is explained by energy losses due to expansion and radiation, as reported in similar LIBS studies [12]. This trend aligns with other published work on Zn-based alloys, confirming that most of the excess energy is used for plasma expansion rather than electron heating. Additionally, the consistency of the measured Te and ne with previously reported values for pure Zn, Cu, and other alloys supports the reliability of our measurements and suggests the behavior is characteristic of this material class under nanosecond laser irradiation.

The findings in this study are not only relevant for fundamental plasma physics but also carry implications for LIBS optimization. For instance, understanding the dependence of Te and ne on laser energy allows for tuning ablation conditions to maximize signal intensity and reduce shot-to-shot variation in industrial alloy diagnostics.

Limitations and uncertainties include lack of error bars in the figures and absence of a full spectrometer calibration, which may introduce minor inaccuracies in line position and intensity. Future work should include instrumental error estimation, line overlap correction, and advanced modeling (e.g., Saha-Boltzmann equilibrium).

Table 1: Plasma parameters of LIBS from Zn:Cu targets at different laser energies.

E (mJ)	T_e (eV)	$n_e \times 10^{18}$ (cm^{-3})	f_p (Hz) $\times 10^{10}$	$\lambda_D \times 10^{-5}$(cm)	N_d
400	0.846	1.000	898.000	0.683	1337
500	0.862	1.061	924.812	0.670	1335
600	0.866	1.091	937.930	0.662	1325
700	0.869	1.106	944.421	0.659	1323
800	0.906	1.121	950.868	0.668	1398

The spectral lines used for the Boltzmann and Stark analyses are summarized in Table 2, including their wavelengths, upper-level energies, transition probabilities (A_{ij}), statistical weights (g_i), and Stark broadening constants (ω_s), all obtained from the NIST Atomic Spectra Database.

Table 2: Spectral lines used in Boltzmann and Stark broadening analysis

No.	Element	Wavelength (nm)	Upper Energy Level E_i (eV)	Einstein Coefficient A_{ij} (s^{-1})	g_i	Stark Width ω_s (nm)
1	Zn I	481.05	5.797	1.0×10^8	3	0.032
2	Cu I	510.55	6.19	3.6×10^7	2	0.025
3	Cu I	515.32	6.19	4.5×10^7	4	0.027
4	Cu I	521.82	6.19	3.9×10^7	6	0.03

4. Conclusions

This study demonstrated that increasing the laser pulse energy from 400 mJ to 800 mJ during the ablation of a Zn:Cu (x = 0.9) target led to noticeable changes in plasma characteristics. The electron temperature (Te) increased from 0.846 eV to 0.906 eV, while the electron number density (ne) rose from $1.000*10^{18}$ cm^{-3} to $1.121*10^{18}$ cm^{-3}. These parameters were diagnosed using the Boltzmann plot method for temperature estimation and Stark broadening of emission lines for electron density, ensuring a solid diagnostic foundation.

From a spectral perspective, there was a clear enhancement in the intensity of neutral Zn I lines, along with the emergence of ionized Zn II lines at higher energies, indicating stronger excitation and ionization processes as laser energy increased.

In addition, the Debye length (λD) decreased from $0.683*10^{-5}$ cm to $0.668*10^{-5}$cm, while the Debye number (Nd) increased, implying a transition toward a more compact and quasi-equilibrated plasma state. These changes also support the assumption of local thermodynamic equilibrium (LTE) under the studied conditions.

It is important to note that this work relied on time-integrated spectra, which limits the ability to track the temporal evolution of plasma parameters. Furthermore, the analysis was conducted under the LTE assumption, which may not fully hold across all spatial and temporal domains of the plasma plume.

These findings emphasize the critical role of laser energy in tuning plasma properties and provide a quantitative framework for optimizing Laser-Induced Breakdown Spectroscopy (LIBS) performance. The observed trends can be instrumental in enhancing the analytical sensitivity, repeatability, and reliability of LIBS, especially for alloy characterization and material diagnostics.

In conclusion, this study confirms that plasma characteristics can be deliberately controlled by adjusting laser pulse energy, reinforcing the value of LIBS as a powerful tool for elemental analysis and real-time process monitoring in both scientific and industrial applications.

References

[1] P. Li, Z. Xiong, Z. Ma, J. Guo, and C. Wang, "Analysis of Cu and Zn contents in aluminum alloys by femtosecond laser-ablation spark-induced breakdown spectroscopy", Open Physics, 21, 113–123 (2023).
[2] S. F. Khaleel and K. A. Aadim, "Investigation study of the plasma parameters for bronze produced by Nd:YAG laser at wavelength 1064 nm: effect of laser energies", Journal of Optics, 54, 256–266 (2025).
[3] Z. M. Abbas and Q. A. Abbas, “Characterization of magnetized-plasma system induced by laser,” Iraqi Journal of Physics, vol. 21, no. 4, pp. 45–55, 2023, doi: 10.30723/ijp. v21i4.1148.
[4] R. S. Mohammed, K. A. Aadimi, and K. A. Ahmed, "Spectroscopy diagnostic of laser intensity effect on Zn plasma parameters generated by Nd: YAG laser," Iraqi Journal of Science, vol. 63, no. 9, pp. 3711–3718, 2022, doi: 10.24996/jjs.2022.63.9.5.
[5] F. H. Salih, S. S. Mahdi, A. H. Ali, “Employment of laser induced breakdown spectroscopy to determine elements of human hair,” Baghdad Science Journal, vol. 22, no. 3, pp. 946–954, 2025 (published online first 20 Oct 2024), doi: 10.21123/bsj.2024.10388.
[6] D. A. Cremers and L. J. Radziemski, Handbook of Laser-induced breakdown spectroscopy, 2nd ed., Wiley (2021).
[7] D. W. Hahn and N. Omenetto, "Laser-induced breakdown spectroscopy (LIBS), part II: Review of instrumental and methodological approaches", Applied Spectroscopy, 66, 347–419 (2012).
[8] F. F. Chen, Introduction to plasma physics and controlled fusion, 2nd ed., Springer, 2012.
[9] E. Mal, R. Junjuri, M. K. Gundawar, and A. Khare, "Optimization of temporal window for application of calibration free-laser induced breakdown spectroscopy (CF-LIBS) on copper alloys in air employing a single line", Journal of Analytical Atomic Spectrometry, 34, 319–330 (2019).
[10] M. S. Mahde, A. H. Ali, M. H. Hussein, “Diagnostic study of copper plasma in air by laser induced breakdown spectroscopy (LIBS),” Engineering & Technology Journal, vol. 33, Part A, no. 5, pp. 1002-1008, 2015, doi: 10.30684/etj.33.5A.18.
[11] J. Iqbal, T. A. Alrabdi, A. Fayyaz, H. Asghar, S. K. H. Shah, and M. Naeem, "Elemental study of Devarda’s alloy using calibration free-laser induced breakdown spectroscopy (CF-LIBS)", Laser Physics, 33, 025701 (2023).
[12] C. Aragón and J. A. Aguilera, "Characterization of laser induced plasmas by optical emission spectroscopy: a review of experiments and methods", Spectrochimica Acta Part B: Atomic Spectroscopy, 63, 893–916 (2008).

[13] G. Cristoforetti, S. Legnaioli, L. Palleschi, and V. Palleschi, "Local thermodynamic equilibrium in laser-induced breakdown spectroscopy: beyond the McWhirter criterion", Spectrochimica Acta Part B: Atomic Spectroscopy, 65, 86–95 (2010).
[14] Z. Hou, Y. Zhang, and X. Li, "A calibration-free model for laser-induced breakdown spectroscopy using non-gated detectors", Frontiers of Physics, 17, 115 (2022).
[15] A. Kramida, Y. Ralchenko, J. Reader, and NIST ASD Team, "NIST Atomic Spectra Database (ver. 5.3)", National Institute of Standards and Technology, Gaithersburg, MD (2015).

تقييم كمي لتأثير طاقة نبضة الليزر على خصائص بلازما Zn–Cu باستخدام تشخيصي بولتزمان وستارك

سنا عبد اللطيف صالح[1]،* و كاظم عبدالواحد عادم[2]

[1] قسم الفيزياء، كلية العلوم، جامعة بغداد، بغداد، العراق
[2] معهد الليزر للدراسات العليا ،جامعة بغداد، بغداد، العراق

البريد الالكتروني للباحث: Sanaa.Abd2304@sc.uobaghdad.edu.iq

الخلاصة: في هذه الدراسة، تم استخدام التحليل الطيفي لانهيار البلازما الناتج بالليزر (LIBS) لتحليل البلازما المتولدة من سبيكة الزنك والنحاس (Zn:Cu) بنسبة (x = 0.9)، باستخدام ليزر Nd:YAG بطول موجي 1064 نانومتر. تم توليد البلازما عند طاقات نبض ليزر مختلفة تتراوح من 400 إلى 800 ميلي جول. تم تحديد درجة حرارة الإلكترونات (Te) باستخدام طريقة مخطط بولتزمان، بينما تم حساب كثافة الإلكترونات (ne) باستخدام ظاهرة اتساع ستارك. كما تم تقييم معلمات بلازما أخرى، بما في ذلك تردد البلازما (fp)، وطول ديباي (λD)، وعدد ديباي (Nd).
أظهرت النتائج أن درجة حرارة الإلكترونات ارتفعت من 0.846 إلكترون فولت عند 400 ميلي جول إلى 0.906 إلكترون فولت عند 800 ميلي جول، كما ارتفعت كثافة الإلكترونات من 1.000×10^{18} سم$^{-3}$ إلى 1.121×10^{18} سم$^{-3}$. وازداد تردد البلازما من 898.000×10^{10} هرتز إلى 950.868×10^{10} هرتز، في حين انخفض طول ديباي قليلاً من 0.683×10^{-5} سم إلى 0.668×10^{-5} سم. وأظهر عدد ديباي تغيراً طفيفاً حول القيمة 1300، مما يعكس سلوكاً جماعياً مستقراً نسبياً عبر نطاق الطاقة المستخدم.
تشير هذه النتائج إلى أن زيادة طاقة الليزر تؤدي إلى توليد بلازما أكثر حرارة وكثافة، مما يعزز شدة الانبعاث وخصائص البلازما. وتُسهم هذه الدراسة في تقديم رؤى كمية حول سلوك بلازما Zn–Cu تحت تأثير طاقات ليزر مختلفة، مما يوفر تطبيقات محتملة في تشخيص المواد باستخدام تقنية LIBS.

IJL, Issue 2, Vol. 24, 2025
https://doi.org/10.31900/ijl.v24i2.526

Research Article

IRAQI JOURNAL OF LASER

The Penetration of Sealer into Coronal Third After Irradiated by Er, Cr: YSGG Laser: A confocal Microscope Study

Nawras Rashid Rasool*, Hussein Ali Jawad

Institute of Laser for Postgraduate Studies, University of Baghdad, Baghdad, Iraq
**Email address of the Corresponding author*: nouras.rashed2202m@ilps.uobaghdad.edu.iq

Article history: Received 10 Mar. 2025; Revised 29 Jul. 2025; Accepted 3 Aug. 2025; Published online 15 Dec. 2025

Abstract:

Objectives: This study aims to detect the penetration of the AH Plus sealer in the coronal third using a pulsed (Er, Cr: YSGG) laser with a short pulse duration when the SWEEPS was used to activate irrigation (Shock wave Enhanced Emission Photoacoustic Streaming). **Methods:** A total of 28 single-rooted mandibular premolars. The laser used is pulsed Er, Cr: YSGG assisted by the SWEEPS technique. There are four groups of samples (n = 7) for each: Group 1: Traditional syringe irrigation using 5 mL of 17% EDTA**.** Group 2: passive ultrasonic irrigation using mL of 17% EDTA. Group 3: Er, Cr: YSGG laser-induced SWEEPS using 5 mL of 17% EDTA. Group 4: Er, Cr: YSGG laser-induced SWEEPS using 5 mL of 5.25% NaOCl and 5mL of 17% EDTA**.** The laser parameters were selected according to the pilot study (Air and water 1%, 0.75 W, 5 Hz, and a short pulse duration of 60μs). The irradiated teeth were obturated by AH plus sealer mixed with Rhodamine B, and the weight percentage was 0.001. Horizontal sectioning was performed at 9mm lengths away from the apex. Four different sites (lingual, distal, mesial, and buccal) were used to determine the depth of sealer penetration. A confocal laser scanning microscope was used to detect the deepest penetration of the sealer. Statistical analysis was conducted using Dunnett t-tests with a significant level set at $p \leq 0.05$**. Results:** The obtained results revealed that AH plus sealer reached the wall of canals in four positions (lingual, distal, mesial, and buccal) at G4 in comparison to G3 and G2 for the selected laser parameters (Air and water 1%, 0.75 W, 5 Hz, and a short pulse duration of 60μs). The data are summarized as follows (mean ± standard deviation in μm) in G1 is 206.20±16, G2 is 593.02±131.67, G3 is 818.58±97.99, G4 is 986.94±27.9 for the lingual side. **Conclusion:** it is concluded that the pulse duration(60μs) of Er, Cr: YSGG laser was authorized successfully upon irrigation activation to achieve the deepest point in the root canal for four positions (lingual, distal, mesial, and buccal), so the lingual side was the best values of the sealer penetration. The best parameters are used in G4. These results suggest that the use of Er, Cr: YSGG laser with SWEEPS technique enhance the penetration of endodontic sealers into dentinal tubules thereby improving the seal quality.

Keywords: Er, Cr: YSGG, SWEEPS, irrigations, confocal laser microscope, endodontic.

1. Introduction

Irrigation plays a fundamental role in endodontic treatments, serving various critical functions, it helps remove organic debris, flushes debris away from the root canal system, and disinfects the canal system to promote tissue healing. Sodium Hypochlorite (NaOCl) is an effective antibacterial irrigation. Ethylenediaminetetraacetic Acid (EDTA), a chelator that effectively removes inorganic debris, the

combination of both is particularly effective in the complete removal of the smear layer, especially in the middle and coronal thirds of the root canal. Addressing anatomical complexity despite their effectiveness, the apical third of the root canal often remains incompletely cleaned due to its intricate anatomy, making it more challenging to achieve thorough disinfection[1]. The effectiveness of irrigation solutions varies based on several factors anatomical variations, such as curved canals or multiple branches, can hinder the effectiveness of irrigation, the ability of the irrigation to penetrate dentinal tubules is crucial for effective cleaning and disinfection, and the method of activation influences how effectively the irrigation removes debris and disinfects the canal [2]. During endodontic instrumentation, a smear layer forms on the dentinal walls, the presence of this layer can weaken the bond between filling materials and the dentin, it leads to inadequate sealing of the root canal, increasing the risk of microleakage, effective removal of this layer is essential to achieve an airtight (air-tight) seal during obturation. Additionally, disinfection is vital for the healing of the periradicular tissues, preventing post-treatment complications [3].

Historically, traditional needle irrigation (NI) has been the standard method for delivering irrigation. The introduction of ultrasonic irrigation, developed by Martin et al., represents a significant advancement in the field. This technique enhances irrigation activation and facilitates better penetration of irrigation into complex root canal systems. Various factors, including duration of activation, type, and size of the ultrasonic tip, and power of the ultrasonic device, influence the effectiveness of ultrasonic activation.

Applications in endodontics, the pulsed Er, Cr: YSGG laser, when used in conjunction with PIPS, effectively eliminates mature Enterococcus faecalis biofilms in complex root canal systems, this is particularly important for ensuring thorough disinfection in challenging anatomical areas [4]. Research has also explored the efficiency of the pulsed Er, Cr: YSGG laser for debonding lithium disilicate laminates, varying pulse durations and exposure times were tested, indicating the versatility of this laser in restorative procedures. Other applications of Er, Cr: YSGG laser, power, and pulse duration are both vital parameters in the surface roughness of zirconia ceramic for enhancement of the bonding strength to the resin cement[5,16,7]. Laser-assisted irrigation, especially when combined with the Shock Wave Enhanced Emission of Photoacoustic Streaming (SWEEPS) technique, has demonstrated superior effectiveness to traditional irrigation methods. Utilizing the pulsed Er, Cr: YSGG laser at a wavelength of 2780 nm, this approach leverages the unique properties of lasers to enhance root canal cleaning and disinfection, the pulsed Er, Cr: YSGG laser is highly absorbed by water, and the energy from the laser causes quick vaporization of the irrigation, this vaporization generates bubbles within the irrigation, which play a crucial role in cleaning, the alternating laser pulses create shock waves that push the irrigation deeper into dentinal tubules, efficiently removing the smear layer from even distant regions of the root canal.[8-10]. Studies, including those by Ozbay et al., have confirmed that this laser method is particularly effective in removing the smear layer, highlighting its advantages in endodontic procedures [11].

The SWEEPS technology brings several distinct advantages to endodontic treatment; the cavitation source can be positioned within the pulp chamber at a safe distance from the apex, reducing the risk of apical extrusion of irrigation. Simultaneous, the SWEEPS technique allows for continuous irrigation throughout the entire root canal system, regardless of its anatomical complexity, this includes effective delivery to lateral canals, isthmuses, and other irregularities [12]. To assess the effectiveness of irrigation and sealer penetration into dentinal tubules, various advanced imaging techniques are employed: confocal laser microscopy, stereomicroscope, and scanning electron microscopy (SEM). These methods provide detailed insights into the extent of sealer penetration, crucial for evaluating the success of endodontic procedures [13].

This study aims to determine the pulsed Er, Cr: YSGG laser parameter in activation on irrigation using the SWEEPS technique on the penetration of AH plus root canal sealer using confocal laser microscopy.

2. Materials and Methods

A total of 28 single-rooted, straight human mandibular premolars were selected randomly distributed from patients undergoing orthodontic or periodontic procedures. Each tooth was clinically and radiographically inspected to confirm the lack of root resorption, open apices, and fractures. After collection, the teeth were instantly washed with distilled water to remove any debris or blood. The cleaned teeth were then placed in a plastic container containing 0.1% thymol solution to prevent microbial contamination, and each tooth was standardized to a uniform length of 12 mm from the anatomical apex, teeth were secured in a bench vice, a double-faced diamond disc was utilized to split the roots perpendicular to the long axis. The cleaning and shaping of the root canals were done using Pro Taper Gold rotary Ni-Ti files, the following: SX, S1, S2, F1, F2, F3, and F4. The canals were irrigated with 2 mL of 5.25% sodium hypochlorite (NaOCl) between each rotary file to improve disinfection and remove debris. Any remaining NaOCl was neutralized by flushing the canals with 5 mL of distilled water. A passive fitting of the ultrasonic activator tip into the canal followed. At 2780 nm, the pulsed Er, Cr: YSGG laser irradiates the teeth in laser groups. The pilot study was done to determine the suitable power and pulse repetition rate for the SWEEPS technique. Ten samples were optimized for a pilot study into two groups (n=5) for each:

GA (n=5): Er, Cr: YSGG laser 2780 nm+17% EDTA (0.25 W, 0.5 W, 0.75 W1, W, 1.25 W).
GB (n=5): Er, Cr: YSGG laser 2780 nm+17% EDTA+5.25Naocl (0.25 W, 0.5 W, 0.75 W1, W, 1.25 W).

From the pilot study, the suitable parameter (Air and water 1%, 0.75 W, 5 Hz, and a short pulse duration of 60μs) according to those parameters, there are randomly assigned four groups of samples (n = 7) for each:

Group 1: Control group

A side-vented irrigation needle was positioned 2 mm shorter than the working length and used to irrigate the samples for one minute with 5 mL of 17% EDTA.

Group2-Ultrasonic activation

After injecting 5 mL of 17% EDTA into the root canal, the ultrasonic activator tip was passively inserted 2 mm shorter than the working length. Each root canal was irrigated three times, taking 20 seconds each time.

Group 3: Er, Cr: YSGG laser-induced SWEEPS using 5 mL of 17% EDTA

The samples were agitated using the pulsed Er, Cr: YSGG laser 2780 nm with 5 ml of 17% EDTA. The fiber tip was placed directly into the canal orifice, and each fiber tip was used in only one canal. Then, five mL of distilled water were placed in each sample and dried using a paper point.

Group 4: Er, Cr: YSGG laser-induced SWEEPS using 5 mL of 5.25% NaOCl and 5 mL of 17%

The samples were agitated using the pulsed Er, Cr: YSGG laser 2780 nm with 5 mL of 17% EDTA+5.25% NaOCl. The fiber tip was placed directly into the canal orifice. Each fiber tip was used for a single canal before being removed. Then, five mL of distilled water were placed in each sample and dried using a paper point. All specimens were obturated with AH plus sealer, which was mixed with Rhodamine B at a weight percentage of 0.001. The obturation method is a cold lateral technique; the chosen master cone was X4, and the sealer was placed inside the canal using a paper tip. After the master cone was inserted and fitted, a finger spreader was employed 1-2 mm shorter than the measured length. After that, additional gutta percha with a 0.02 tapering was inserted until the root canal was completely sealed. Radiographs were collected to evaluate obturation. The root samples were then coronally sealed using glass ionomer cement. After that, the samples were kept in an incubator set at 37 °C for a week. The roots were separated from their tubes, and the samples were mounted in polyester resin. Then, horizontal sectioning was performed for each root at 9mm lengths away from the apex. Sectioning was done using a

diamond saw with a continuous water jet and a spinning speed of 500 rpm. Then, the surfaces of the samples were polished using sandpaper discs (P1000) installed on a polishing apparatus. A confocal laser scanning microscope operating at 532 nm was used to examine the sectioned root slices, and each slice's depth of sealer penetration was assessed at four different locations (lingual, distal, mesial, and buccal). Ten times the magnification was employed. And photographs with a resolution of 1,024_1,024 pixels.

3. Statistical Analysis

Image analysis was done using Adobe Photoshop 7.0. At each site, the greatest depth of sealer penetration in the dentinal tubules, beginning from the canal wall, was measured and recorded on ten distinct lines, as shown in Figure 1.

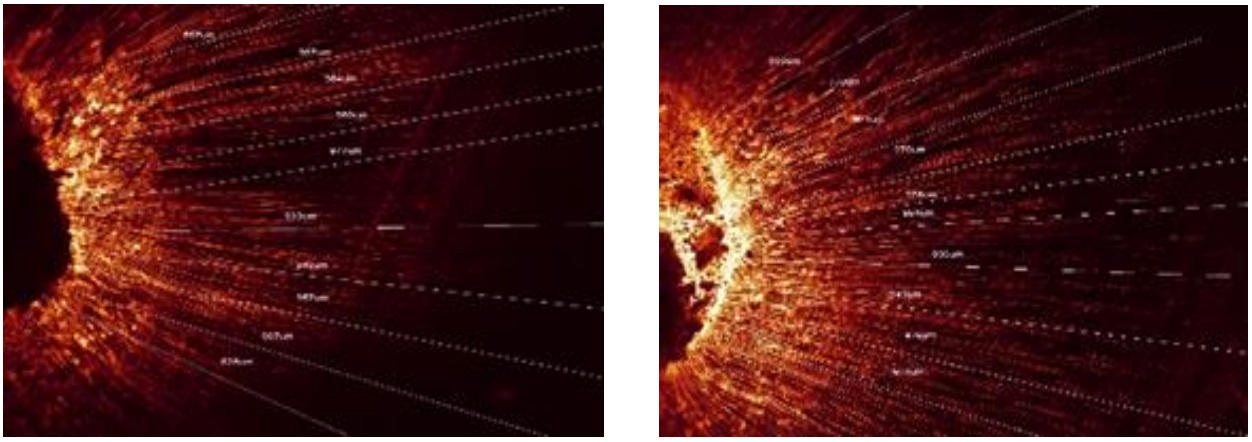

Figure 1: The calculation in ten distinct lines in each site, the sealer's maximum penetration depth into dentinal tubules, beginning from the canal wall, was recorded.

The t-test was used to analyze repeated measures of the tested and control groups—data expressed as mean±SD and other descriptive statistics. The normal distribution of all values was assessed using the Tests of Normality, including the Kolmogorov-Smirnov and Shapiro-Wilk tests. Dunnett t-tests made multiple comparisons between the tested groups and the control group. LSD test was used to calculate the significant differences between the tested mean, the letters (A, B, C, D), LSD represented the levels of significance, highly significant start from the letter (A) and decreasing with the last one. A power analysis was conducted prior to the study using G*Power software, confirming that a sample size of n = 7 per group provided a statistical power of 80% to detect significant differences in sealer penetration depth between groups. Values of $p>0.05$ were considered statistically non-significant, while $p\leq0.05$ were considered significantly different. The statistical analysis was carried out by SPSS (v 20).

4. Safety and Clinical Application

This study was conducted entirely in vitro. Rhodamine B was used exclusively as a fluorescent tracer and is not approved for clinical use due to its toxicity. While the Er,Cr:YSGG laser is FDA-approved for dental applications, its clinical use in endodontic irrigation should be approached with caution. Care must be taken to avoid apical extrusion, minimize thermal damage, and ensure safe fiber positioning to reduce the risk of periapical complications.

5. Results and discussion

The results illustrate the descriptive statistics of the penetration depth of AH plus sealer for four locations (lingual, distal, mesial, and buccal) of the coronal third, with the lingual side having the highest values of

penetration, as shown in Table 1. Pulse duration (60µs) was approved effectively in activation of irrigation; better results were obtained in G4 when compared with G1 (pair3) and also when compared between tested groups themselves, with high results in G4 (pair5). G4 has the highest values of penetration (P value =0.0001), as shown in Table 2. Mean± standard deviation of sealer penetration in **µm** in four direction-coronal third as shown in Table 3. As seen in Figure 2, the bar chart shows the mean (um) value of sealer penetration in four groups of a coronal third (lingual side).

Table 1. Comparison of three groups, G2, G3, and G4, with a control group for the coronal third (lingual side), and between them

Paired Samples t Test

Control group vs Tested groups Coronal third Lingual		Paired Differences					t	Df	Sig. (2-tailed)
		Mean	Std. Deviation	Std. Error Mean	95% Confidence Interval of the Difference				
					Lower	Upper			
Pair1	G1CL - G2CL	-386.81857	102.45196	38.72320	-481.57083	-292.06631	-9.989	6	0.0001
Pair2	G1CL - G3CL	-384.70143	49.63216	18.75919	-430.60352	-338.79934	-20.507	6	0.0001
Pair3	G1CL - G4CL	-612.38143	98.26834	37.14194	-703.26449	-521.49837	-16.488	6	0.0001
Pair4	G1CL - G5CL	-780.74571	79.11534	29.90279	-853.91520	-707.57623	-26.109	6	0.0001

Tested groups Coronal third Lingual	Paired Differences					t	Df	Sig. (2-tailed)
	Mean	Std. Deviation	Std. Error Mean	95% Confidence Interval of the Difference				
				Lower	Upper			

Pair1	G2CL - G3CL	2.11714	105.75723	39.97248	-95.69198	99.92627	.053	6	0.959
Pair2	G2CL - G4CL	-225.56286	139.07085	52.56384	-354.18194	-96.94377	-4.291	6	0.005
Pair3	G2CL - G5CL	-393.92714	140.63266	53.15415	-523.99066	-263.86363	-7.411	6	0.0001
Pair4	G3CL - G4CL	-227.68000	77.35783	29.23851	-299.22406	-156.13594	-7.787	6	0.0001
Pair5	G3CL - G5CL	-396.04429	72.89616	27.55216	-463.46199	-328.62658	-14.374	6	0.0001
Pair6	G4CL - G5CL	-168.36429	89.94507	33.99604	-251.54960	-85.17897	-4.952	6	0.003

Table 2. Statistical results for four groups in the On-Way ANOVA.

	Statistics/One-way ANOVA				P value
Coronal third Lingual	**G1CL**	**G2CL**	**G3CL**	**G4CL**	
N	7	7	7	7	0.003
Mean/µm	D	C	B	A	
	206.20±70.85	593.02±131.67	818.58±97.99	986.94± 27.91	

LSD test was used to calculate the significant differences between the tested mean, the letters (A, B, C, and D) indicate statistically significant differences ($p \leq 0.05$) according to the LSD test. Group "A" shows the highest significant value, while "D" shows the lowest. Groups sharing the same letter are not significantly different.

Table 3. Mean± standard deviation of sealer penetration in µm in four direction-coronal third.

Group	Lingual	Buccal	Mesial	Distal
G1	206.20±16	322.14±57.02	218.09±41.75	202.32±48.26
G2	593.02±131.67	414.05±21.67	513.12±11.40	448.27±139.86
G3	818.58±97.99	703.11±52.85	772.47±93.97	693.46±79.04
G4	986.94±27.91	969.33±75.94	929.21±59.76	969.25±57.22

G4 exhibited the highest penetration values in all aspects, with statistically significant differences compared to G1–G3 ($p < 0.05$).

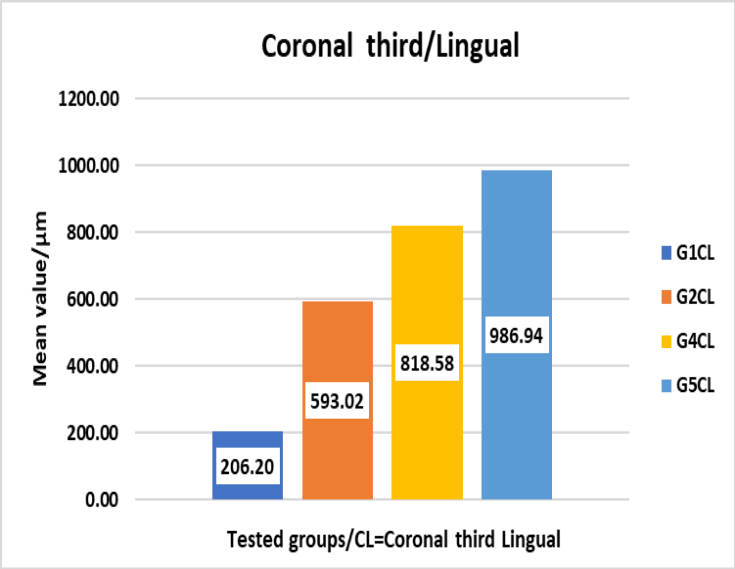

Figure 2: Bar chart showing the mean depth of sealer penetration (µm) on the lingual aspect of the coronal third in groups G1 to G4. The Y-axis shows penetration depth in micrometers (µm), and the X-axis lists the group numbers.

In this study, the best outcomes were observed in (G4), especially on the lingual side, the efficacy of this group can be attributed to the combination of NaOCl (sodium hypochlorite) and EDTA (ethylenediaminetetraacetic acid), this dual approach effectively targets both organic and inorganic materials due to the antibacterial properties. Additionally, the short pulse duration (60µs) of the laser led to a high energy density, resulting in effective shock waves that enabled the irrigation to access remote regions inside the root canal [14-16]. The increased penetration in the pulsed Er, Cr: YSGG laser group is likely due to the photomechanical effects of the pulsed Er, Cr: YSGG laser. This laser has a high absorption rate in water, which generates bubbles in the irrigation, enhancing fluid dynamics and creating a more effective push of the irrigation into the dentinal tubules, this mechanism helps improve the distribution and activation of the irrigation, leading to high sealer penetration. These findings are consistent with the work of Ayca Yilmaz et al. (2020), who reported greater sealer penetration in laser-assisted irrigation groups using confocal laser scanning microscopy [17-19]. Research indicates that the irrigation flow rate is more critical than its concentration. Factors that contribute to effective irrigation include the volume of the irrigation, proximity to the apex, the temperature of the solution, and activation methods used [20]. Different sealers have varying physicochemical properties, including viscosity, flowability, and setting time, which can influence their ability to penetrate the tubules. Sealers designed

for better flow characteristics tend to achieve greater penetration depth. To facilitate a detailed assessment of sealer penetration, 0.1% Rhodamine B dye was added to the Ah Plus sealer, this approach enhances visibility when using confocal laser microscopy, allowing for precise measurement of sealer depth within dentinal tubules [21].

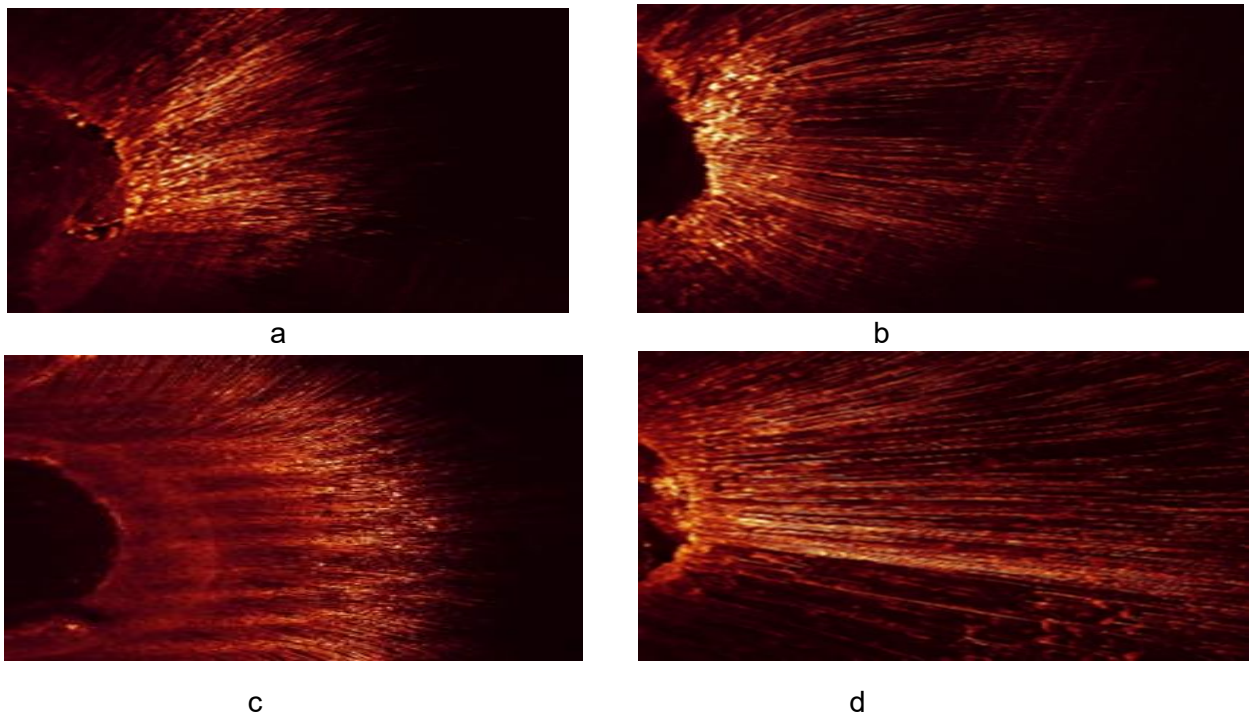

Figure 3: Confocal laser microscopic images showing the sealer's penetration into the coronal third lingual side of four groups. b.G2, c.G3, d.G4, and a.G1.

In this study, the diameter of dentinal tubules varies between different regions of the tooth. Generally, coronal tubules are larger in diameter compared to apical tubules, which are narrower, the greater permeability of coronal dentin allows for more effective sealer penetration in this area compared to the apical region, the apical region of teeth often exhibits narrower tubules, and the presence of sclerotic dentin, which can significantly reduce permeability. It was noted that sealer penetration was generally greater in the buccolingual direction compared to the mesiodistal one, this may be attributed to the (butterfly effect) which suggests that increased sclerosed dentin in the mesial and distal areas of the root canal impedes sealer flow, the anatomical configuration and the presence of variations in dentin density can contribute to these directional differences in sealer penetration. CLSM was preferred over scanning electron microscopy (SEM) due to it is ability to provide devices to detect detailed images of the specimen at lower magnification without disturbing the flow properties of the sealers, this method proved to be a quick and efficient evaluation of the sealer penetration. CLSM represents a versatile method in the study of dentin and provides adequate information on the adaptation and distribution of the sealer within dentinal tubules [22-24]. The effectiveness of the pulsed Er, Cr: YSGG laser in removing the smear layer and disinfecting the root canal system can improve the overall quality of the procedure, leading to better long-term results, the use of pulsed Er, Cr: YSGG laser can potentially reduce the number of visits required for root canal therapy. The development of flexible fiber tips has made the pulsed Er, Cr: YSGG laser even more versatile and effective in endodontic treatment. These tips allow the laser to be used in the narrow spaces of the root canal, ensuring more cleaning and disinfection, this study indicate that using SWEEPS technology together with the Er,Cr:YSGG laser enhance irrigation efficiency and sealer penetration, especially in complex root canal anatomies [25].

6. Limitation

The study's limitations included the possibility of microscopic residues forming during the cutting stage and these remain on the sample surfaces causing artifacts of confocal images, this has been dealt by a polishing device used to polish the surfaces of samples. Another constraint was the physical properties of the sealer, high-viscosity materials may not flow effectively into the tubules, even when aided by laser activation, and sealers may undergo setting reactions that limit further penetration after initial application, so we use AH plus sealer which is characterized by good handling and superior physical properties.

7. Conclusion

From the obtained results. It is concluded that the pulse duration(60μs) of Er, Cr: YSGG laser successfully activates irrigation to reach the root canal's deepest point in four different places (lingual, distal, mesial, and buccal). The SWEEPS technique is based on the pulsed Er, Cr: YSGG laser with certain parameters (Air and water 1%, 0.75 W, 5 Hz, and a short pulse duration of 60μs), so the lingual side was the best value of the sealer penetration. The best parameters are used in G4.

8. Suggestion for future work

1. Using another laser to compare the same objectives during the SWEEPS procedure.
2. Utilizing alternative irrigants.
3. Comparing various types of sealers regarding their penetration.

References

[1] Rasheed SS, Jawad HA, “Permeability of radicular dentine after using different irrigant activation techniques, including photo-induced photoacoustic streaming technique”, Iraqi J. Laser, 20(1), 43–50 (2021).
[2] Rasheed SS, Jawad HA, “Smear layer removal from the apical third using the Er, Cr: YSGG photon-induced photoacoustic streaming”, Iran. Endod. J., 16(4), 238–244 (2021).
[3] Shaheed AA, Jawad HA, Hussain B, Said AM, “Healing of Apical Periodontitis after Minimally Invasive Endodontics therapy using Er, Cr: YSGG laser: A Prospective Clinical Study”, Syst. Rev. Pharm., 11(2), 1–7 (2020). doi:10.5530/srp.2020.2.21
[4] Ibrahim GI, Jawad HA, “In vitro study of the effect of laser photon-induced photoacoustic streaming on the Enterococcus faecalis biofilm in complicated root canal system”, Iraqi J. Laser, 23(1), 58–70 (2024). https://doi.org/10.31900/ijl.v23i1.418
[5] Al-Karadaghi SS, Jawad HA, Al-Karadaghi T, “The influence of pulse duration and exposure time of Er, Cr: YSGG laser on lithium disilicate laminate debonding, an in vitro study”, Heliyon, 9(3), e14600 (2023). https://doi.org/10.1016/j.heliyon.2023.e14600
[6] Al-Karadaghi SS, Jawad HA, “Debonding of LDSVs utilizing Er, Cr: YSGG laser irradiation with fractional technique: An in vitro study”, Aust. Dent. J., 68(2), 125–134 (2023). https://doi.org/10.1111/adj.12958
[7] Muhammed FS, Jawad HA, “Pulsed Er, Cr: YSGG laser for surface modification of dental zirconia ceramic”, Iraqi J. Laser, 20(1), 21–29 (2021).
[8] Bago I, Đurin A, Kanižaj D, et al., “The efficacy of a novel SWEEPS laser-activated irrigation compared to ultrasonic activation in the removal of pulp tissue from an isthmus area in the apical third of the root canal”, Lasers Med. Sci., 38, 189–197 (2023). https://doi.org/10.1007/s10103-023-03857-4
[9] Jordana J, Tandean JN, Salim JF, Cahyani F, Sampoerno G, “Shock wave enhanced emission photoacoustic streaming (SWEEPS): An alternative to conventional irrigation in endodontic treatment”, Conserv. Dent. J., 12(2), 68–72 (2022). doi:10.20473/cdj.v12i2.2022.68-72
[10] Kaplan F, Erdemir A, “Evaluating the effect of different irrigation activation techniques on the dentin tubules penetration of two different root canal sealers by laser scanning confocal microscopy”, Microsc. Res. Tech., 86(7), 791–802 (2023). doi:10.1002/jemt.24339
[11] Blanken J, De Moor RJG, Meire M, Verdaasdonk R, “Laser-induced explosive vapor and cavitation result in effective irrigation of the root canal. Part 1: a visualization study”, Lasers Surg. Med., 41(7), 514–519 (2009). https://doi.org/10.1002/lsm.20798

[12] Rödig T, Westbomke V, Haupt F, et al., "Effect of preparation size on the removal of accumulated hard-tissue debris from the mesial root canal system of mandibular molars using SWEEPS technology", Clin. Oral Invest., 27, 2787–2796 (2023). https://doi.org/10.1007/s00784-023-04862-1
[13] Toursavadkohi S, Zameni F, Afkar M, "Comparison of tubular penetration of AH26, EasySeal, and SureSeal Root Canal Sealers in Single-Rooted Teeth Using Scanning Electron Microscopy", J. Res. Dent. Maxillofac. Sci., 3(3), 27–32 (2018). doi:10.29252/jrdms.3.3.27
[14] Pereira TC, Neelakantan P, Vula J, et al., "Biofilm removal from a simulated isthmus and lateral canal during syringe irrigation at various flow rates: a combined experimental and Computational Fluid Dynamics approach", Int. Endod. J., 54(3), 427–438, (2021). doi:10.1111/iej.13420
[15] Vatanpour M, Toursavadkouhi S, Sajjad S, "Comparison of three irrigation methods, SWEEPS, ultrasonic, and traditional irrigation, in smear layer and debris removal abilities in the root canal beyond the fractured instrument", Photodiagn. Photodyn. Ther., 37, 102707 (2022). https://doi.org/10.1016/j.pdpdt.2021.102707
[16] Widbiller M, Keim L, Schlichting R, et al., "Debris removal by activation of endodontic irrigants in complex root canal systems: A standardized in-vitro-study", Appl. Sci., 11(16), 7331 (2021). https://doi.org/10.3390/app11167331
[17] Kareem R, Jawad HA, "Cavity Disinfection Using Er, Cr: YSGG Laser-Induced Photoacoustic Streaming Technique", Iraqi J. Laser, 21(2), 41–47 (2022). https://doi.org/10.31900/ijl.v21i2.349
[18] Keles A, Askerbeyli Ors S, Purali N, Kucukkaya Eren S, "Effect of different sealer activation techniques on dentinal tubule penetration", Aust. Endod. J., 49(3), 470–475 (2023). doi:10.1111/aej.12738
[19] De Bem IA, de Oliveira RA, Weissheimer T, et al., "Effect of ultrasonic activation of endodontic sealers on intratubular penetration and bond strength to root dentin", J. Endod., 46(9), 1302–1308 (2020). https://doi.org/10.1016/j.joen.2020.06.014
[20] Yilmaz A, Yalcin TY, Helvacioglu-Yigit D, "Effectiveness of various final irrigation techniques on sealer penetration in curved roots: a confocal laser scanning microscopy study", Biomed. Res. Int., 2020, Article ID 8060489 (2020). https://doi.org/10.1155/2020/8060489
[21] Shaheed AA, Jawad HA, Hussain BMA, Said AM, "Penetration depth of AH-plus Sealer in dentinal tubules following ErCr:YSGG laser or EDTA application: A confocal laser microscopic study", Test Eng. Manag., 82, 10154–10161 (2020). https://www.researchgate.net/publication/348976401
[22] Ozasir T, Eren B, Gulsahi K, Ungor M, "The effect of different final irrigation regimens on the dentinal tubule penetration of three different root canal sealers: A confocal laser scanning microscopy study in vitro", Scanning, 2021, 1–9 (2021). doi:10.1155/2021/8726388
[23] Pérez-Alfayate R, Mercade M, Algar-Pinilla J, et al., "Root canal filling quality comparison of a premixed calcium silicate endodontic sealer and different carrier-based obturation systems", J. Clin. Med., 10(6), 1271 (2021). https://doi.org/10.3390/jcm10061271
[24] Pérez-Alfayate R, Algar-Pinilla J, Mercade M, Foschi F, "Sonic activation improves bioceramic sealer's penetration into the tubular dentin of curved root canals: a confocal laser scanning microscopy investigation", Appl. Sci., 11(9), 3902 (2021). https://doi.org/10.3390/app11093902
[25] Schoop U, Goharkhay K, Klimscha J, et al., "The use of the erbium, chromium: yttrium-scandium-gallium-garnet laser in endodontic treatment: the results of an in vitro study", J. Am. Dent. Assoc., 138(7), 949–955, (2007). https://doi.org/10.14219/jada.archive.2007.0291

تغلغل مانع التسرب الى الثلث التاجي بعد تعرضه الى ليزر الايربيوم: دراسة بالمجهر البؤري

نورس راشد رسول*, حسين علي جواد

معهد الليزر للدراسات العليا، جامعة بغداد، بغداد، العراق

البريد الالكتروني للباحث:nouras.rashed2202m@ilps.uobaghdad.edu.iq

الخلاصة: تهدف هذه الدراسة إلى تقييم مدى تغلغل مادة الاغلاق AH-Plus في الثلث التاجي من الجذر باستخدام ليزر نبضي (Er, Cr: YSGG) بمدة نبضة قصيرة عند استخدام SWEEPS لتنشيط عملية الغسيل (Shock wave Enhanced Emission

Photoacoustic Streaming) تم إجراء ما مجموعه 28 ضرسًا سفليًا أحادي الجذر. الليزر المستخدم هو ليزر نبضي الاربيوم كروميوم SWEEP.بمساعدة تقنية .هناك أربع مجموعات من العينات (ن = 7) لكل منه المجموعة 1:
المجموعة 2: الري بالموجات فوق الصوتية السلبية باستخدام مل من 17 EDTA الري بالمحقنة التقليدية باستخدام 5 مل من 17% EDTA%
المجموعة 3 :Er, Cr : المسح الضوئي المستحث بالليزر YSGG باستخدام 5 مل من 17 .المجموعة 4 Er, Cr :المسح الضوئي المستحث بالليزر YSGG باستخدام 5 مل من 5.25 NaOCl %و5 مل من EDTA17 % تم اختيار معلمات الليزر وفقًا للدراسة التجريبية (الهواء والماء 1%، 0.75 واط، 5 هرتز، ومدة نبضة قصيرة 60 ميكروثانية). تم سد الأسنان المشعة بواسطة مانع تسرب AH plusمخلوطًا مع روداميين ب، وكانت النسبة المئوية للوزن 0.001. تم إجراء التقطيع الأفقي على أطوال 9 مم بعيدًا عن القمة. تم استخدام أربعة مواقع مختلفة (لساني، بعيد، أوسط، وخدي) لتحديد عمق اختراق المادة المانعة للتسرب. تم استخدام مجهر مسح ليزري بؤري للكشف عن أعمق اختراق للمادة المانعة للتسرب. تم تحليل البيانات إحصائيًا بواسطة اختبارات Dunnett t وكانت قيمة $p\leq0.05$. أظهرت النتائج التي تم الحصول عليها أن مادة مانعة التسربG4 بالإضافة إلى المادة المانعة للتسرب وصلت إلى جدار القنوات AHفي أربعة مواضع (لساني، بعيد، أوسط، وخدي) عند بالمقارنة مع G3 و G2 لمعلمات الليزر المحددة (الهواء والماء 1٪، 0.75 وات، 5 هرتز، ومدة نبضة قصيرة 60 ميكروثانية). استنتج أن مدة النبضة (60 ميكروثانية) من ليزر Er، Cr: YSGG تم ترخيصها بنجاح عند تنشيط الري لتحقيق أعمق نقطة في قناة الجذر لأربعة مواضع (لساني، بعيد، أوسط، وخدي)، لذلك كان الجانب اللساني هو أفضل قيم لاختراق المادة المانعة للتسرب. يتم استخدام أفضل المعلمات في G4 وبما ان هذه دراسة مختبرية يوصى باجراء دراسات سريرية مستقبلية لتأكيد فعالية التقنية وتحسين نتائج المعالجة اللبية.

IJL, Issue 2, Vol. 24, 2025
https://doi.org/10.31900/ijl.v24i2.530

Research Article

Removing Bioceramic Sealer Remnants using Er,Cr:YSGG laser Irradiation with PIPS Process: In Vitro Study

Sara Zanzal Sami*, Hussein Ali Jawad

Institute of Laser for Postgraduate Studies, University of Baghdad, Baghdad, Iraq
** Email address of the Corresponding Author*: sara.sami2202m@ilps.uobaghdad.edu.iq

Article history: Received 8 Apr.2025, Revised 15 Jul. 2025, Accepted 8 Aug. 2025, Published 15 Dec. 2025

Abstract: Background: This vitro study investigated the effectiveness of Er,Cr:YSGG laser-activated irrigation in removing root canal filling remnants during endodontic retreatment. The technique used photon-induced photoacoustic streaming (PIPS) at 700 µs pulse duration to activate 2.5% sodium hypochlorite (NaOCl) and 17% EDTA. **Materials and methods:** Twenty-one extracted human maxillary and mandibular premolars with single roots were instrumented and obturated using gutta-percha and a bioceramic root canal sealer. After retreatment using nickel-titanium rotary files (XP-endo Retreatment), the specimens were randomly assigned into three groups (n=7 per group) according to the irrigation technique: Group 1: conventional syringe irrigation (control), Group 2: passive ultrasonic irrigation, Group 3: laser-activated irrigation using Er, Cr:YSGG laser (2780 nm, 700 µs pulse duration, 5 Hz, 1 W, RFT2 tip, with no air or water spray). All samples were sectioned longitudinally and examined under a scanning electron microscope (SEM) to assess the presence of residual filling materials in the coronal, middle, and apical thirds. Cleanliness scores were assigned by two calibrated endodontists based on a 4-grade scoring system and were statistically analyzed using one-way ANOVA followed by Tukey's post hoc test. The significance level was set at $\alpha = 0.05$. Statistical analysis revealed a significant difference among the groups ($P < 0.05$). Group 3 showed significantly lower residual debris compared to Groups 1 and 2 across all root thirds, while the difference between Groups 1 and 2 was not statistically significant ($P > 0.05$).
Results: Group 3 (n = 7) exhibited significantly lower residual debris compared to Groups 1 and 2 across all canal thirds ($P < 0.05$). The mean cleanliness scores were highest in the coronal third, followed by the middle and apical thirds. No statistically significant differences were observed between Group 1 and Group 2 ($P > 0.05$), suggesting limited effectiveness of ultrasonic irrigation compared to laser activation.
Conclusion: The use of Er,Cr:YSGG laser-activated irrigation with PIPS at a 700 µs pulse duration, combined with 2.5% NaOCl and 17% EDTA, significantly improved the removal of root canal filling remnants during retreatment. These findings suggest that laser-activated irrigation may serve as an effective adjunct to conventional retreatment protocols, offering enhanced cleaning efficacy across all canal levels.

Keywords: Er,Cr:YSGG, PIPS, pulse duration, retreatment. irrigants.

1. Introduction

Thorough cleaning of the endodontic therapy to be successful, the root canal system must be obturated in three dimensions [1]. This includes the dentinal tubule system and proper filling of the canal. Nevertheless, treatment may still fail even when appropriately performed [2]. Gutta-percha remains the most commonly used obturation material in conjunction with various sealers [3]. However, large voids between the filling material and the canal walls may increase the risk of post-treatment disease [4]. In the event of failure, nonsurgical root canal retreatment is often considered the most viable solution,

particularly when technical errors are the cause. This process involves removal of the old root canal filling material, followed by disinfection and re-obturation of the canals [5]. According to the American Association of Endodontists' Glossary of Endodontic Terms, nonsurgical retreatment includes complete removal of the original root filling material, reinstrumentation, and refilling of the canal system [6].
Total Fill BC Sealer (FKG, Switzerland) is a pre-mixed, injectable, radiopaque, hydrophilic bioceramic sealer that relies on dentinal tubule moisture to initiate and complete its setting reaction [7]. The removal of root filling materials can be achieved using a wide range of instruments and techniques, including hand files, Gates-Glidden burs, heat carriers, nickel-titanium (NiTi) rotary systems, ultrasonics, lasers, and various solvents [8]. Recently, specialized NiTi instruments have been developed for this purpose, such as the XP-endo Finisher R (FKG Dentaire, Switzerland), which changes shape in response to body temperature due to its MaxWire alloy [9].

Effective irrigation is another critical component of successful retreatment. Passive ultrasonic irrigation (PUI) has proven effective in removing tissue remnants, debris, and medicaments from the canal system [10]. A combination of irrigants is typically required, as no single solution is adequate on its own [11]. Sodium hypochlorite (NaOCl) has been widely used as an endodontic irrigant since the mid-20th century due to its antimicrobial properties and ability to dissolve organic tissue [12].
In recent years, laser-activated irrigation has been introduced to enhance irrigant effectiveness [13]. Photon-induced photoacoustic streaming (PIPS) is one such innovation, utilizing laser-generated shockwaves to improve fluid dynamics within the canal [14]. The Er,Cr:YSGG laser (2780 nm) exhibits high absorption in water, making it suitable for activating irrigants. Compared to other lasers like Er:YAG, it produces efficient energy absorption (400 mm^{-1} for Er,Cr:YSGG vs. 1200 mm^{-1} for Er:YAG) with minimal heat generation due to its pulsed emission mode [15].

Additionally, it has been demonstrated that veneer surfaces can be safely and repeatedly heated with this laser type without causing fractures [16, 17]. Histological studies report that pulpal responses to Er,Cr:YSGG laser exposure are minor and reversible, comparable to those seen with high-speed rotary instruments [18]. PIPS uses a laser fiber tip placed in the pulp chamber, reducing the risk of heat transmission to periapical tissues [19]. When used with 17% EDTA, Er,Cr:YSGG laser activation (5 Hz, air/water off, short pulse duration) effectively removes smear layers [20, 21].
Scanning electron microscopy (SEM) is a standard method to evaluate root canal cleanliness, allowing assessment of remaining filling materials and smear layer removal [22]. Yang et al. [23] demonstrated that activating 2.5% NaOCl and 17% EDTA with PIPS significantly improved the removal of iRoot SP sealer and gutta-percha compared to PUI and conventional syringe irrigation (CSI). Similarly, Almohareb et al. [24] evaluated the efficacy of diode laser and ultrasonic irrigation for retreatment of BC sealer and gutta-percha-filled canals, noting no added benefit from surfactants.Despite promising findings, the optimal laser parameters for PIPS using the Er,Cr:YSGG laser remain unclear, particularly regarding the removal of BC sealer and gutta-percha from complex root canal systems.

Thus, the aim of in vitro study was to determine the most effective laser settings for Er,Cr:YSGG PIPS irrigation to improve the removal of residual filling materials during root canal retreatment, in comparison with conventional syringe irrigation and passive ultrasonic irrigation.

2. Materials and Methods

This investigation followed the Declaration of Helsinki. Ethical approval for the procedures of the present study was obtained (10-2023-462).

2.1 Sample selection

A total of 21 extracted human single-rooted premolars with mature apices, straight canals (curvature ≤ 5°), and standardized root length of 12 mm were selected based on radiographic evaluation in both buccolingual and mesiodistal directions. Teeth with root caries, fractures, internal/external resorption, previous endodontic treatment, calcifications, or complex root anatomy were excluded.

Following extraction, all teeth were stored at 25 ± 1 °C in 0.1% thymol solution for no longer than two weeks to prevent microbial growth while maintaining tooth integrity.

2.2 Preparation of samples

All specimens were decoronated at the cementoenamel junction using a diamond disk under constant water cooling to obtain standardized root segments (12 mm). A size #10 K-file was introduced until it was visible at the apical foramen to confirm patency. The working length (WL) was determined by subtracting 1 mm from this measurement.

The 21 teeth were randomly divided into three experimental groups (n = 7) using simple randomization via an online software tool (www.randomizer.org). Allocation concealment was ensured through sealed opaque envelopes, and group assignment was performed by an independent operator not involved in the experimental procedures. All instrumentation, irrigation, and evaluation steps were performed under the same environmental conditions (room temperature: 25°C; relative humidity ~60%).
A closed system was created by sealing the canal apex with softened wax to prevent irrigant extrusion during activation and to ensure stable positioning of the specimens within the custom-made acrylic mold. While this method may slightly alter apical fluid dynamics, it is a commonly accepted practice in in vitro studies to maintain consistent internal conditions and focus the evaluation on intracanal efficacy.
Root canal preparation was performed using the Race Evo rotary system (FKG Dentaire SA, Switzerland) with a crown-down technique. The working length (WL) was established by inserting a #10 K-file (Dentsply Maillefer, Switzerland) into the canal until visible at the apical foramen, then subtracting 1 mm. All instrumentation procedures were performed in a room-temperature-controlled environment (25 ± 1 °C) with adequate lighting.

The canal was shaped up to size 30, taper 0.06. Throughout preparation, each canal received copious irrigation using a 30-gauge side-vented needle (NaviTip, Ultradent, USA) positioned 2 mm short of WL. Irrigants used included:
2.5% Sodium Hypochlorite (NaOCl) (Cerkamed, Poland): 5 mL per canal during shaping.
The pH of the sodium hypochlorite solution was approximately 12.
17% EDTA (Cerkamed, Poland): 2 mL after shaping.
Sterile saline (Pioneer, Iraq): 5 mL as a final rinse.

The total irrigation time per canal was approximately 90 seconds. Each irrigant was delivered slowly over 15–20 seconds per mL to allow optimal contact time. After irrigation, canals were dried using three sterile absorbent paper points (Diadent X3, Korea). Canals were obturated using the single-cone technique with size 30/.06 gutta-percha cones (Dentsply Maillefer, Switzerland) and TotalFill BC Sealer (FKG Dentaire SA, Switzerland). The sealer was introduced into the canal using a Lentulo spiral, and a pre-fitted GP cone was inserted to full WL. Excess GP was seared at the orifice using a heated instrument and vertically compacted with a plugger. To prevent coronal leakage, flowable composite (Filtek Z350 XT, 3M ESPE, USA) was applied over the canal orifice and light-cured for 20 seconds. All specimens were then stored in a humidor (KEWEIYIQI, China) at 37°C and 100% relative humidity for 3 weeks to ensure complete setting of the bioceramic sealer. To ensure outcome assessor blinding, the coded specimens were anonymized by an independent operator prior to the retreatment and SEM evaluation stages.

2.3 Retreatment technique

The root canal retreatment was performed using the XP-Endo RISE NiTi rotary retreatment system (FKG Dentaire SA, Switzerland) with a crown-down technique following the manufacturer's instructions. Initially, the bulk of the root filling was removed using the retreatment files, then final shaping was completed with a Race Evo file size 30 and 0.04 taper to the full working length. Retreatment was considered complete when no visible filling material remained on the canal walls as confirmed under magnification. Following instrumentation, samples were randomly allocated into three groups (n=7 per group) according to the final irrigation and activation protocol used.

Group 1: Manual Syringe Irrigation (Control)

Canals were irrigated using a 30-gauge side-vented needle placed 2 mm short of the working length. After each file, 2 mL of 2.5% NaOCl was delivered over approximately 20 seconds, followed by drying with paper points. Subsequently, 1 mL of 17% EDTA was introduced and left in the canal for 60 seconds to allow adequate chelation. Finally, 2 mL of sterile distilled water was used to flush out residual irrigants [25].

Number of irrigation cycles: 3 per canal
Total irrigation time: ~3 minutes
Temperature and humidity: Room temperature (~25°C), humidity controlled.
Group 2: Passive Ultrasonic Irrigation (PUI)
Following conventional irrigation as in Group 1, the canals were activated ultrasonically using an ultrasonic device (Woodpecker U6 LED, China) set at 25% power in E mode (28 kHz). A size 20 ultrasonic tip (taper 0.02) was inserted 1 mm short of the working length without contacting canal walls and activated for 20 seconds per cycle.
Irrigants: 2 mL 2.5% NaOCl + 1 mL 17% EDTA
Number of activation cycles: 3 per canal
Total activation time: 60 seconds
Environmental conditions: Controlled at room temperature (~25°C)

2.4 Pilot study for laser group

An acrylic mold was used to set the teeth in to be used in a pilot study to determine the ideal laser settings, such as power and pulse repetition rate (PRR), that produce the PIPS effect without having any negative side effects. Five roots of teeth were used, and a range of laser characteristics, such as PRR 5 Hz, 1% air, 1% water, and laser power (0.1 W, 0.25 W, 0.5 W, 0.75 W, and 1.0 W), were used to evaluate the Er.Cr:YSGG laser parameters. Following radiation exposure, the best view was acquired at various magnifications (500X, 1000X, 1500X, 2000X, 2500X, and 3000X) using an AxiaTM ChemiSEMTM Scanning Electron Microscope operating at 3 KV voltages and 100 pA pressure settings. SEM images of at least three randomly selected areas (coronal, middle, and apical) from each specimen were obtained. The pilot study test results were used to define the final laser settings for the Er.Cr:YSGG laser, which were (1w), PRR 5 Hz, Air: 1%, and Water: 1%. When using more than 1 watt, carbonization of the sample is noticed.

Group 3 (laser-activated irrigation with Er,Cr:YSGG 2780 nm for 700 us pulse duration):
Laser parameters for group 3
Power =1 W
Frequency = 5 Hz
Air= 1%
Water=1%
Pulse duration = 700 us
Energy = 200 mm Joules
Energy density =71 ×104 mm Joules
Dose=1065 ×105 Joules
Irradiation time = 30 seconds
Number of total pulses = 150 pulse/sec.
Peak power =2.8×10 2 watts
Power density =1×105 watts/cm2

A 2,780 nm Er, Cr: YSGG laser (Waterlase iPlus Biolase, San Clemente, CA, USA) was used to pulse the samples. Its settings were 1 watt, 700 µs of pulse duration, 5 Hz repetition frequency, 1% air, and 1% water level. Using a 600 µm tip diameter (Biolase, San Clemente, CA, USA), samples were exposed to radiation for thirty seconds in this examination before an irrigant was placed into the canal. The tip was parallel and 2 mm distant from the root surface and perpendicular to it. Following the tooth's longitudinal

sectioning, it was separated into the coronal, middle, and apical thirds. The tooth's portion with the root canal space was kept, while the region with the faint canal was discarded. The root specimen was then sent for SEM examination. All specimen allocations and irrigation procedures were performed by an operator blinded to the study hypothesis. Post-treatment, the samples were coded and assessed by two independent endodontic specialists who were blinded to group assignment. The entire procedure was conducted in a laboratory environment controlled for temperature (25 ± 1 °C) and relative humidity (50–60%) to minimize variability and ensure reproducibility.

2.5 Power Analysis Justification

A post hoc power analysis was conducted using G*Power software (version 3.1.9.7) to evaluate the adequacy of the sample size used in this study. The analysis focused on the comparison between the control group (G1) and the Laser 700 microseconds group (G3) at the coronal third level, where the mean difference was 2.00 with a standard deviation of 0.577 (n = 7 per group). The resulting post hoc power for this comparison was calculated to be 0.98 (98%), which exceeds the commonly accepted threshold of 0.80. This indicates that the study had sufficient statistical power to detect significant differences and minimize the risk of Type II error.

3. SEM analysis

Thermo Fisher Scientific's (Waltham, USA) scanning electron microscopy (SEM) equipment was used to prepare the samples for examination. After dehydrating the samples, they were put in an ion sputter vacuum system coating apparatus (Ngstrom Advanced) and sprayed with a layer of gold 10–15 nm thick. This created a conductive metal layer on the sample, which helped to restrict charging, reduce heat damage, and boost the secondary electron signal required for SEM topographic analysis [26]. The coronal, middle, and apical thirds of each sample were then subjected to SEM analyses at 10 kV and 1000× magnification [27]. A total of 4 images per third of the sample were taken. SEM images were captured at various magnifications (×500, ×1000, ×2000, and ×3000) to allow detailed observation of the canal wall cleanliness and dentinal tubule exposure. The same magnification was used consistently across samples for each corresponding canal third (coronal, middle, apical) to enable accurate and standardized visual comparison. To determine a blind score for the SEM images [23], two endodontists adapted criteria based on Bernardes et al. and Pirani et al. [23] as follows: Score 1: Less than 75% of the tubules are visible due to debris in the smear layer and filler material in some areas. Score 2, with less than 50% of tubules visible in a limited area, and score 3, with a smear layer and infill debris usually present. Tubules are not apparent; all dentin has a smear layer and filling debris. Score 0: In case zero, more than 75% of the tubules are visible and open, and no smear layer or filler material is present.

In addition to the visual scores, a quantitative analysis of residual contamination was performed using ImageJ software (NIH, USA). Each SEM image was analyzed to calculate the percentage of the canal wall area covered by residual sealer or debris relative to the total observed dentinal area. This provided a numerical contamination index for each image, supplementing the visual scores with objective data. All SEM findings were compiled into comparative tables presenting both the mean qualitative scores and quantitative contamination percentages for each group across the coronal, middle, and apical thirds. These tables allowed for detailed visual and statistical comparisons.

Representative SEM images are presented in Figure 1, showcasing typical canal surfaces from each third and treatment group. For instance, Figure 1A (Group I, apical third) exhibits heavy coverage with residual sealer and no visible tubules, indicating a score of 3 and a high contamination percentage. In contrast,

Figure 1B (Group II, coronal third) shows a surface with mostly open tubules and minimal debris, corresponding to a score of 0. The cleaning efficacy observed in this study, especially with laser-assisted protocols, is in agreement with previous SEM analyses reported by Bernardes and Pirani et al. [23], who noted enhanced smear layer removal in the apical third using Er:YAG laser techniques and emphasized the limitations of conventional irrigation in reaching the apical third.

A-control group

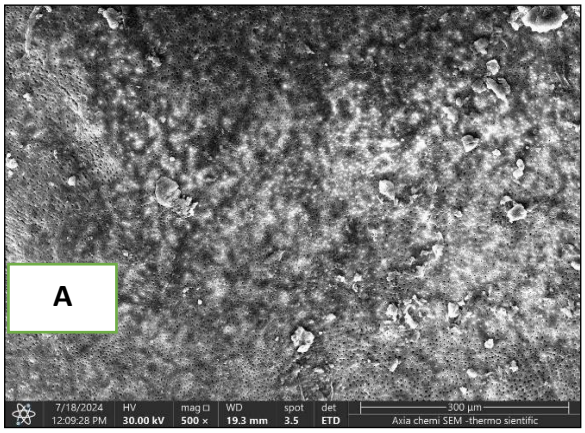

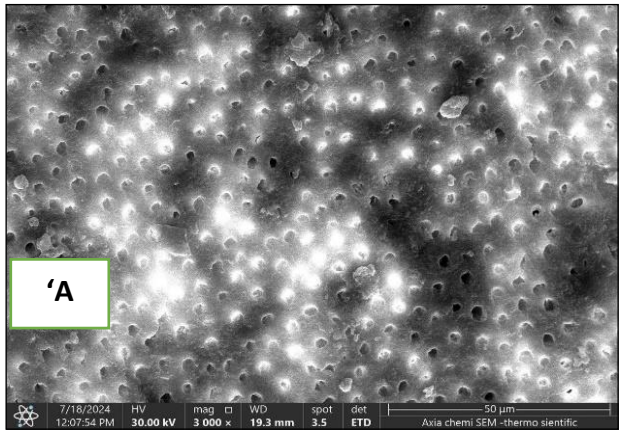

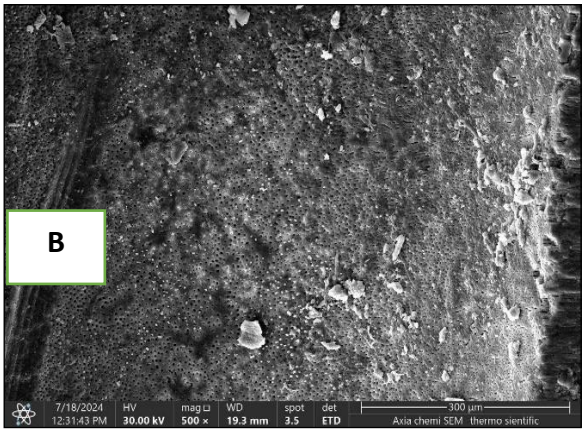

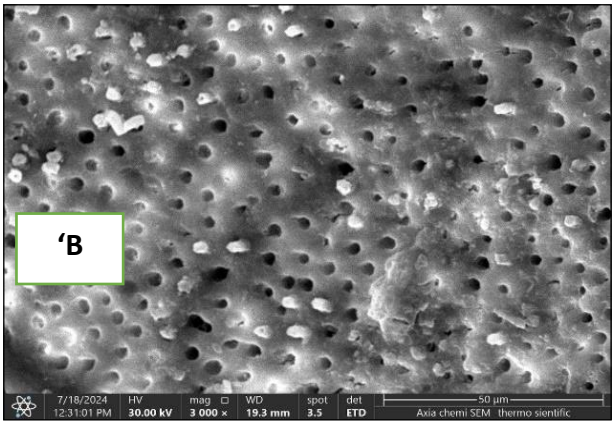

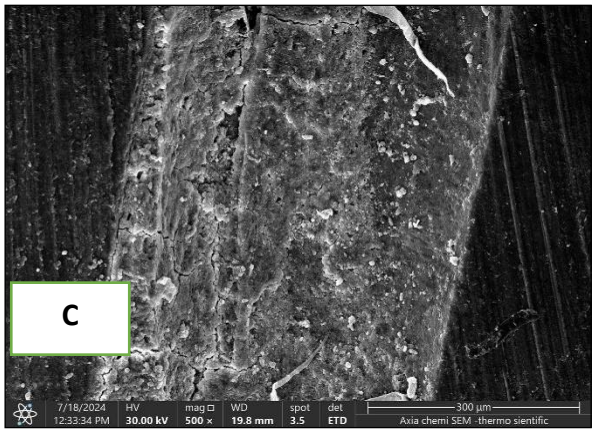

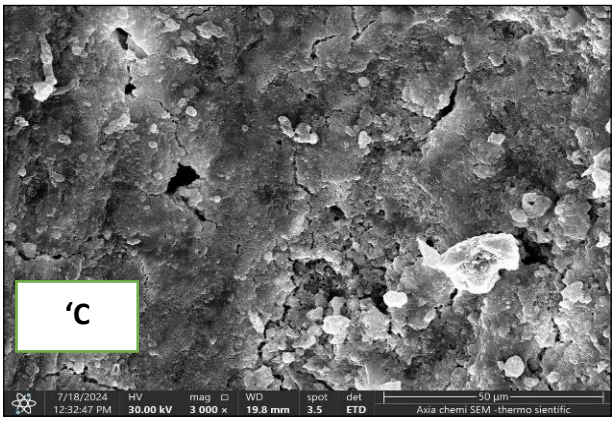

B-Ultrasonic activation group

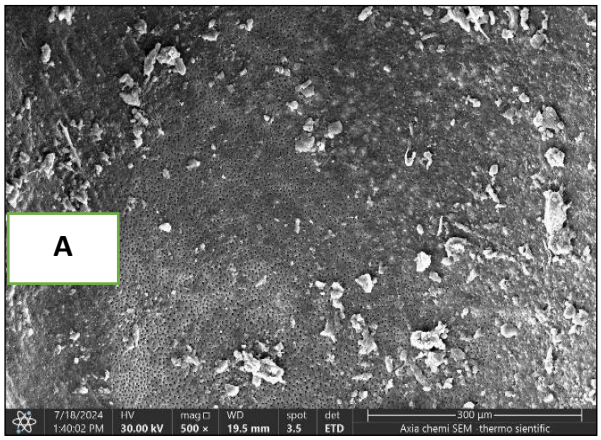

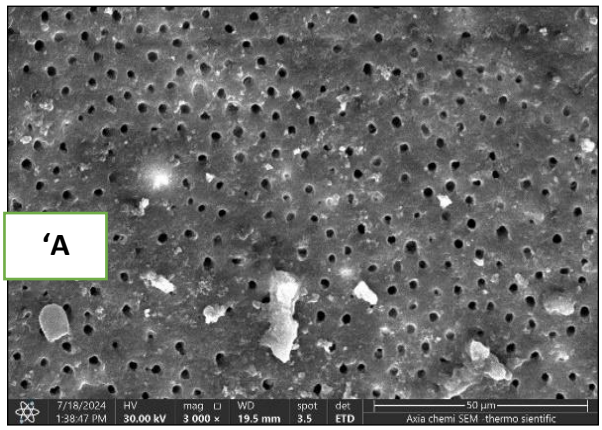

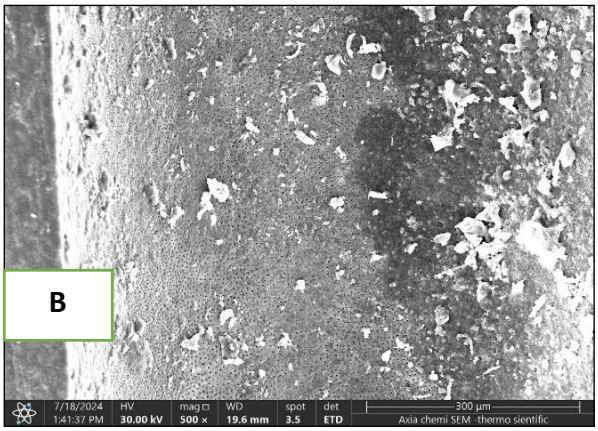

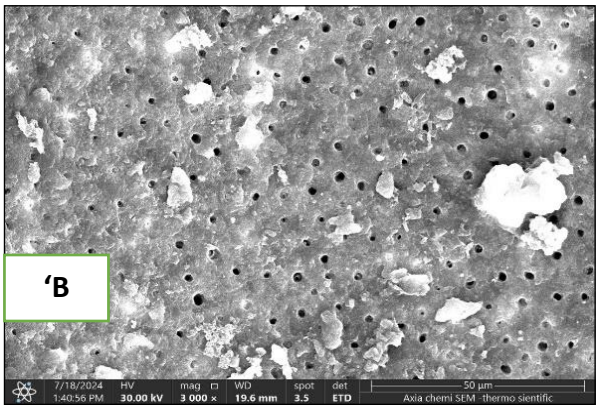

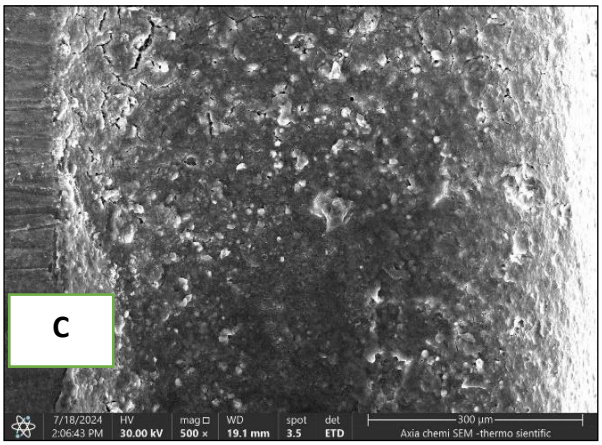

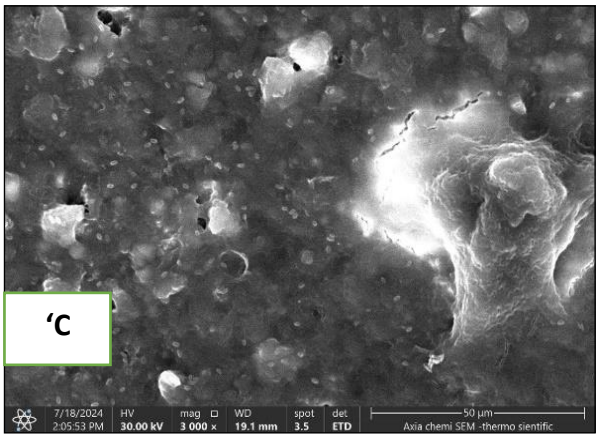

C-laser activated irrigation at 700 us group

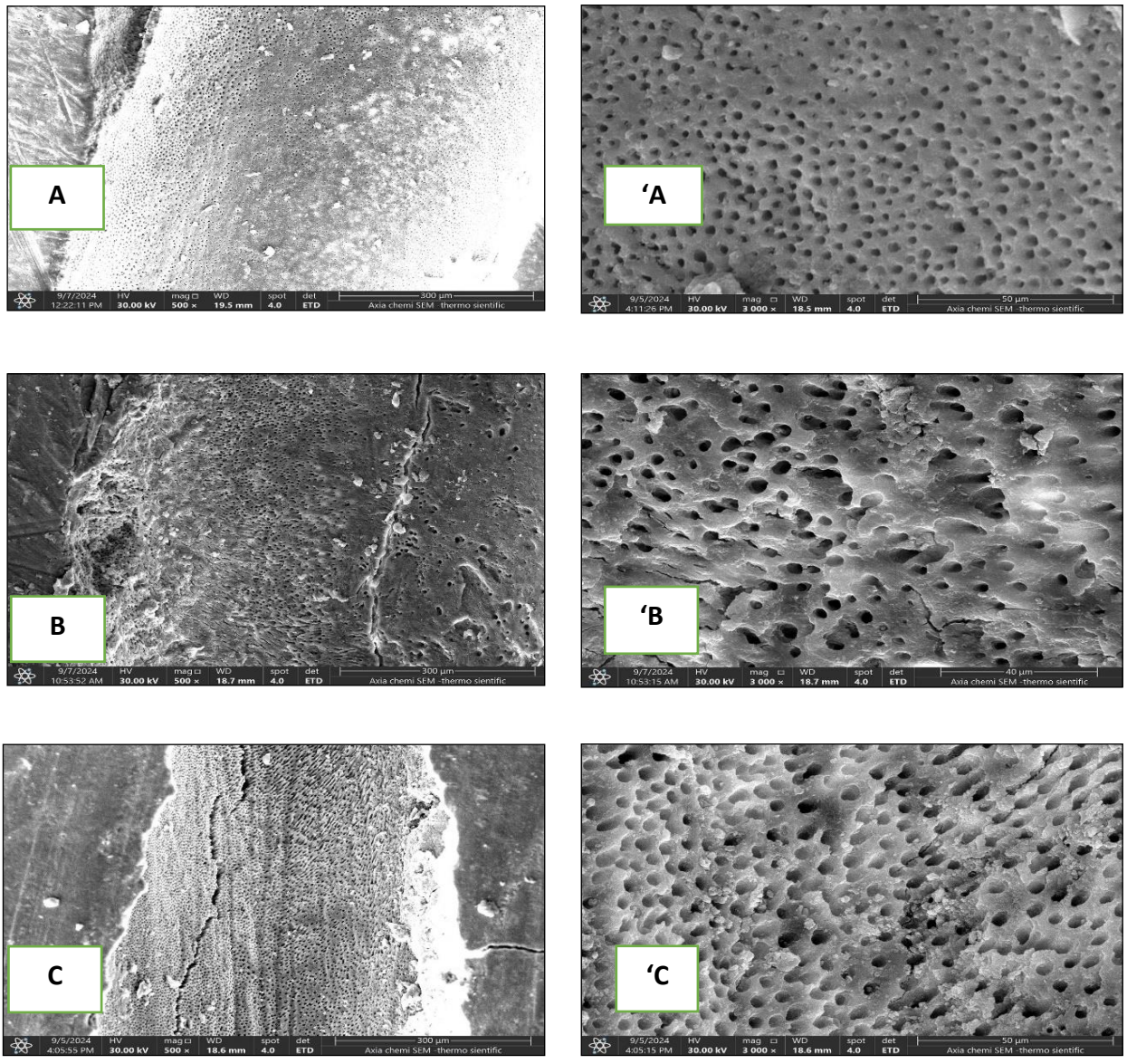

Figure 1: SEM images of the obturation materials remnants after retreatment A. Coronal third at (500x) 'A coronal third at (3000x), B. Middle third at (500x) 'B middle third at (3000x), Apical third at (500x) 'C apical third at (3000x).

4. Statistical Analysis

Statistical analysis was performed using SPSS software (version 3.1.9.7). The normality of the data distribution was assessed using both the Shapiro-Wilk and Kolmogorov-Smirnov tests. All variables were normally distributed ($P > 0.05$), justifying the use of parametric tests. Descriptive statistics including the mean, standard deviation, median, minimum, and maximum values were calculated for all experimental groups at the coronal, middle, and apical thirds of the root canal. These values provided a clear quantitative profile of the residual sealer in each region, allowing for precise comparisons across

interventions. Paired sample t-tests were conducted to assess intra-group and inter-group differences between the control group and each of the tested groups (Ultrasonic, Er,Cr:YSGG laser with 700 µs pulse duration) at each canal third. One-way ANOVA followed by post-hoc tests (LSD and Dunnett's tests) was used to determine statistically significant differences between groups. The LSD test assigned significance letters (A, B, C) to indicate homogeneous subsets, while Dunnett's test compared each experimental group with the control group. A p-value ≤ 0.05 was considered statistically significant. All data were expressed as mean ± standard deviation (SD).

Table 1. Residual filler material's mean and standard deviation (SD) for each group in the coronal third of the root canal.

Coronal third	G 1 Control	G2 Ultrasonic	G3 laser 700 us
N	7	7	7
Mean±SD	B	B	A
	2.43±0.54	2.43±0.78	0.57±0.78

P value 0.001

LSD test was used to calculate the significant differences between the tested mean, the letters (A and B) represented the levels of significance, similar letters mean there are no sig differences between the tested mean.
p≤0.05 were considered significantly different

Table 2. Residual filler material's mean and standard deviation (SD) for each group in the middle third of the root canal.

Middle third	G 1 Control	G2 Ultrasonic	G3 laser 700 us
N	7	7	7
Mean±SD	B	B	A
	2.14±0.96	2.57±0.78	0.7±0.75

P value 0.001

LSD test was used to calculate the significant differences between the tested mean, the letters (A , B) represented the levels of significance, similar letters mean there are no sig differences between the tested mean.
p≤0.05 were considered significantly different

Table 3. Residual filler material's mean and standard deviation (SD) for each group in the apical third of the root canal.

Apical third	G 1 Control	G2 Ultrasonic	G3 laser 700 us
N	7	7	7
Mean±SD	B	B	A
	2.43±0.78	2.85±0.37	0.86±1.46

P value 0.001

LSD test was used to calculate the significant differences between the tested mean, the letters (A, B) represented the levels of significance, Similar letters mean there are no sig differences between the tested means.
p≤0.05 were considered significantly different

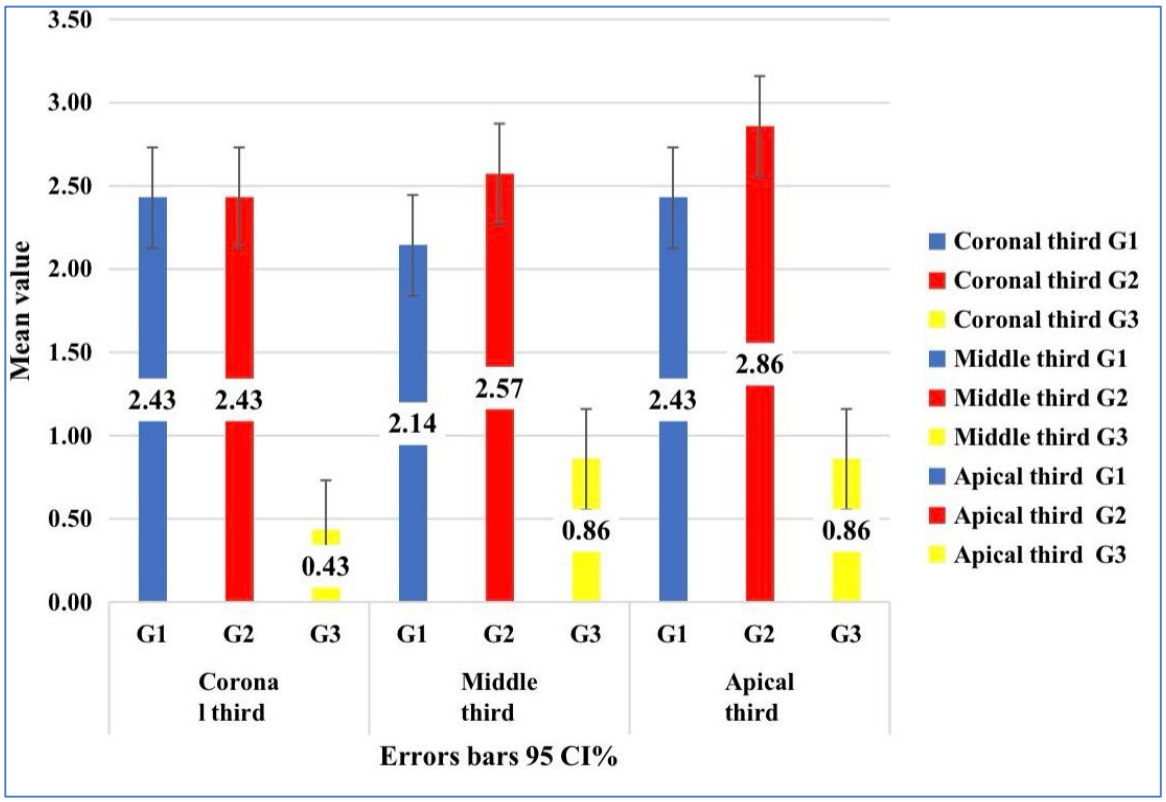

Figure 2: Bar chart represents the mean values of sealer remnants in the coronal, middle, and apical thirds for the three groups.

3. Result and discussion

Scanning Electron Microscope (SEM) Analysis:
Representative SEM images for the coronal, middle, and apical thirds are shown in figure 1, demonstrating varying amounts of residual filling material among the groups.
In group 1 (control), all three thirds of the root canal continuously showed a thick smear layer and a sizable amount of sealer residue. With residual material covering estimated to be over 80% and cleaned tubules in several areas falling below 35%, the apical third was most damaged, with the majority of dentinal tubules appearing entirely blocked. In the middle and coronal thirds, similar circumstances were noted, including restricted tubule exposure and enduring debris coatings. These results are consistent with Table 1, higher mean values for the remaining material.

In group 2 (ultrasonic activation), moderate improvement in canal cleanliness was observed. The coronal third showed the best outcome, with SEM images and ImageJ analysis indicating approximately 85% of the dentinal tubules were open. The middle third had a moderate smear layer and cleaner surfaces, with an estimated 65% of tubules being patent. However, the apical third remained problematic, where fewer than 50% of the tubules were open and thick layers of sealer residue persisted. The cleaning efficacy in this area, based on the SEM images and confirmed by table 2, was relatively low—around 10%.

Group 3 (laser activation via PIPS) continuously attained the greatest level of cleanliness. SEM pictures showed extensive tubular openness and canal walls in the coronal third that were almost completely clear of material. There were several open dentinal tubules and little remains in the middle third. Notably, more than 50–75% of the tubules were revealed in the apical third, despite the fact that some filling remains were still discernible. This indicates that even in the most difficult area of the root

canal system, there is a superior cleaning impact. The effectiveness of laser-activated irrigation is confirmed by the much lower mean values of residual material reported in table 3 ($P < 0.05$), which statistically support these results.

The SEM images and quantitative analyses (tables 1-3) taken together show that laser-activated irrigation using the PIPS technique performs better than both ultrasonic activation and conventional irrigation, especially when it comes to opening dentinal tubules in the apical region and eliminating root-filling remnants.

Quantitative Analysis:
As illustrated in Figure 2 and detailed in Tables 1–3, the mean values of residual filling material differed significantly among groups and across canal thirds.

1. Coronal third (table 1):

Ultrasonic (G2): 2.43 ± 0.78
Control (G1): 2.43 ± 0.54
Laser (G3): 0.57 ± 0.78
P value: <0.001
There was a statistically significant reduction in residue in the laser group compared to both control and ultrasonic groups.

2. Middle third (table 2):

Ultrasonic (G2): 2.57 ± 0.78
Control (G1): 2.14 ± 0.96
Laser (G3): 0.70 ± 0.75
P value: <0.001
The laser group again demonstrated the lowest residue, with statistically significant differences from both other groups.

2. Apical third (table 3):

Ultrasonic (G2): 2.85 ± 0.37
Control (G1): 2.43 ± 0.78
Laser (G3): 0.86 ± 1.46
P value: <0.001
A significant reduction in debris was observed in the laser group, indicating its enhanced cleaning effect even in the apical third.

These findings support the superior efficacy of Er,Cr:YSGG laser-activated irrigation (PIPS) compared to conventional and ultrasonic methods, particularly in reducing residual filling material across all thirds of the canal. Endodontic retreatment is often necessary in cases of persistent periapical pathology, inadequate debridement, or complex root canal anatomy that compromises the initial outcome [22]. Numerous studies have investigated the success rates of retreatment, suggesting that outcomes can be comparable to primary treatment when appropriate protocols are followed [28]. One of the primary challenges in retreatment is the complete removal of previous root canal filling materials, particularly bioceramic sealers, due to their high adhesion and potential for deep dentinal tubule penetration [29, 30].
In the present study, the ability of Er,Cr:YSGG laser-activated irrigation using PIPS technology was assessed in comparison to passive ultrasonic irrigation and conventional methods for removing bioceramic sealer remnants. Direct visual assessment under SEM was employed, which has been established as a reliable approach to evaluate canal cleanliness [31]

Our results demonstrated statistically significant differences among the three groups in all root levels (p=0.001). Laser-activated irrigation (Group 3) exhibited significantly lower residual filling material than both ultrasonic (Group 2) and the control group (Group 1), particularly in the middle and apical thirds. For example, in the apical third, the laser group recorded a mean residue of 0.86 ± 1.46, compared to 2.85 ± 0.37 in the ultrasonic group and 2.43 ± 0.78 in the control. These differences suggest that PIPS significantly enhances removal efficiency in deeper and more anatomically complex areas

Similar findings were reported by Yang et al. [23], who showed that neither ultrasonic nor laser activation alone was sufficient to completely eliminate iRoot SP and gutta-percha, though laser-based methods showed superior effectiveness. This supports our findings, which indicate that while complete removal remains challenging, laser-activated irrigation using PIPS achieves significantly cleaner canal walls.

The enhanced performance of PIPS may be attributed to its unique mechanism of action. Unlike conventional irrigation, PIPS employs low-energy, long-pulse laser bursts that generate secondary cavitation effects through rapid vapor bubble formation and collapse. These micro-explosions facilitate deep penetration of irrigants and disrupt the smear layer and debris [33, 34]. Galler et al. [35] demonstrated that laser-activated irrigants reach deeper into dentinal tubules than conventional or ultrasonic methods, especially in the apical third where accessibility is most limited. SEM analysis in this study confirmed these outcomes. In Group 3, the dentinal tubules appeared significantly cleaner across all thirds, with the apical and middle thirds showing open tubules and minimal residual debris. This is in contrast to the control and ultrasonic groups, where smear layer and filling remnants were more abundant, particularly in the apical third, where access is most difficult.

Interestingly, some samples in the laser group showed unexpected accumulation of debris in the coronal third, while the apical third appeared cleaner. This counterintuitive result may be explained by the physical dynamics of bubble propagation and fluid motion during PIPS activation. As described by Swimberghe et al. [36] and Gregorčič et al. [37], the primary vapor bubble generated within the pulp chamber expands coronally, and its collapse may induce a reverse flow of debris from the apical region to the coronal. Therefore, the accumulation observed in the coronal third may not be due to insufficient cleaning but rather to the backflow of loosened debris from deeper regions.

Another possible explanation is that the coronal third, being more accessible and already cleaned mechanically, may not have contained significant residue to begin with, and what was observed post-activation might be the redeposited material transported during irrigation. Regarding the irrigant protocol, the use of 2.5% NaOCl combined with 17% EDTA further enhanced cleaning effectiveness. Saquy et al. [38] and Zehnder [39] reported that EDTA remains effective in demineralizing dentin even in the presence of NaOCl, and this combination facilitates smear layer removal and exposes dentinal tubules for deeper irrigant penetration. This synergy is maximized by the activation from PIPS. The laser parameters used in this study (1 W, 5 Hz, 700 µs pulse duration, 1% air and water) were carefully selected to optimize activation without inducing thermal damage. The long pulse duration and low energy minimize carbonization risks while allowing sufficient energy transfer to the irrigant.

In comparison to the control group (G1) and the ultrasonic group (G2), the Er,Cr:YSGG laser group (G3) with a 700 µs pulse duration showed significantly reduced residual sealer values in the coronal, middle, and apical thirds [$p < 0.05$]. In the coronal and middle thirds, there were no discernible differences between the control and ultrasonic groups [$p > 0.05$]; however, the laser group continuously performed better than both. Due to the extended pulse duration's improved photoacoustic streaming and cavitation effects, it appears that laser-activated irrigation was more successful in penetrating and cleaning the canal walls. Deeper irrigant penetration and more effective destruction of residual materials are encouraged by these effects. Notably, the laser group also displayed noticeably fewer sealer remains in the apical third, which is usually the hardest region to clean, underscoring the effectiveness of this technology over traditional approaches. 2.5% sodium hypochlorite (NaOCl) was chosen as the irrigant concentration in this investigation because it has a well-established balance between acceptable cytotoxicity and efficient organic tissue breakdown. Even though larger concentrations (like 5.25%) have been used in earlier research, there is evidence that raising the concentration of NaOCl does not necessarily improve its

effectiveness, rather, it may raise the risk of dentinal erosion and periapical tissue irritation [39]. As a result, the chosen concentration supports the current movement to maximize safety without sacrificing cleaning capacity. Moreover, the irrigant concentration was the same for all groups in this study, so it wasn't a factor affecting comparisons across groups.

In light of the current study's findings, the efficacy of removing bioceramic sealer remnants using the PIPS technique supported by Er,Cr:YSGG laser aligns well with several recent systematic reviews. These reviews have highlighted the superiority of laser-activated irrigation in enhancing the penetration of irrigants into hard-to-reach areas of the root canal and in opening dentinal tubules compared to conventional methods such as ultrasonic activation, as reported by Badami et al. [34] and Galler et al. [35]. Such findings reinforce the potential of the PIPS technique as a promising option in endodontic retreatment, particularly when bioceramic sealers are involved. However, some studies report variations in effectiveness depending on irrigant concentration and application protocol, which may explain the observed differences in sealer removal efficacy between the coronal and apical thirds in our study. Therefore, further clinical investigations are recommended to validate the safety and effectiveness of this approach before widespread clinical adoption.

In summary, the findings of this study reinforce the effectiveness of laser-activated irrigation using the Er,Cr:YSGG laser with PIPS in endodontic retreatment. This method demonstrated superior removal of bioceramic sealer remnants compared to ultrasonic and conventional methods, particularly in the apical and middle thirds. While complete removal remains a challenge, the significant reduction in residual material and improved dentinal tubule cleanliness observed in the laser group highlight its potential as a valuable adjunct to traditional retreatment protocols. These results support the integration of PIPS into clinical practice to enhance outcomes in challenging retreatment cases.

7. Conclusion

This study aimed to evaluate the effectiveness of the PIPS technique using the Er,Cr:YSGG laser in removing bioceramic sealer remnants from root canals. The results showed that laser-activated irrigation significantly improved the removal of residual filling materials when compared to both syringe irrigation and passive ultrasonic activation ($p < 0.05$). The coronal and middle thirds of the canals showed the most noticeable improvement, while the apical third showed less pronounced differences. These findings can be attributed to the enhanced fluid dynamics achieved with the PIPS technique, which allows irrigants to reach more complex areas of the canal system. While the outcomes are encouraging and align with previous studies that support laser-assisted irrigation, it's important to note that this was an in vitro investigation. Therefore, clinical conditions such as anatomical variations and the presence of vital tissue were not simulated. Further clinical research is needed to confirm the safety and effectiveness of this approach in real-life settings. In conclusion, PIPS activation with Er,Cr:YSGG appears to be a promising adjunct for improving root canal cleanliness and could potentially be integrated into clinical practice, provided future in vivo studies validate its benefits and safety for routine use.

Acknowledgments

The authors would like to thank the staff at the University of Baghdad's Institute of Laser for Postgraduate Studies in Iraq.

References

[1] E. Schäfer and D. Lohmann, "Three-dimensional obturation of the root canal system", in Endodontics: Principles and Practice, 5th ed., M. Hülsmann and F. Barbakow, Eds. Elsevier, 2021, 265–277 (2021).
[2] M. Haapasalo, Y. Shen, W. Qian, and Y. Gao, "Irrigation in endodontics", Br Dent J, 216(6), 299–303 (2014).
[3] A. U. Eldeniz and A. Erdemir, "Materials and techniques for root canal obturation", in Endodontics: Principles and Practice, 6th ed., M. Torabinejad and R. E. Walton, Eds. Elsevier, 307–332 (2019).
[4] H. J. Al Shaarani, A. M. Mohammed, and A. S. Mahmood, "Efficiency of the Er:YAG laser and ultrasonic techniques in removing endodontic filling material from straight root canals: An in vitro study", Int J Laser, 21(1), 1–6 (2022). doi:10.31900/ijl.v21i1.445.

[5] K. Kfir, M. Tsesis, E. Yakirevich, Z. Matalon, and I. Kedem, "The efficacy of four irrigation techniques in removing root canal filling material: a cone-beam computed tomography study", Lasers Med Sci, 27(1), 115–120 (2012). doi:10.1007/s10103-011-0880-3.
[6] A. Zanza, R. Reda, and L. Testarelli, "Endodontic orthograde retreatments: challenges and solutions", Clin Cosmet Investig Dent, 15, 245–265 (2023). doi:10.2147/CCIDE.S397835.
[7] A. M. Naeem and I. M. Al-Zaka, "Different root canal irrigants influence the push-out bond strength of AH Plus and Bioceramic sealers", J Bagh Coll Dent, 33(2), 21–29 (2021).
[8] P. Agrawal, P. K. Ramanna, S. Arora, et al., "Evaluation of efficacy of different instrumentation for removal of gutta-percha and sealers in endodontic retreatment: an in vitro study", J Contemp Dent Pract, 20(11), 1269–1273 (2019).
[9] E. Karova, V. Dogandzhiyska, I. Tsenova-Ilieva, and M. Raykovska, "Endodontic retreatment with DRace NiTi Instruments Supplemented with XP-Endo Finisher R", EAS J Dent Oral Med, 4(3), 80–85 (2022).
[10] J. Tandon, R. K. Yadav, A. P. Tikku, V. K. Shakya, and S. K. Singh, "Comparative evaluation of different irrigating and irrigant activation system in removal of gutta-percha/sealer during retreatment: An in vitro Micro-CT study", J Oral Biol Craniofac Res, 12(4), 444–448 (2022). doi:10.1016/j.jobcr.2022.05.006.
[11] S. S. Rasheed and H. A. Jawad, "permeability of radicular dentine after using different irrigant activation techniques including photo induce photoacoustic streaming technique", IJL, 20(1), 43–50 (2021). doi:10.31900/ijl.v20i1.269.
[12] O. A. Peters, "Current challenges and concepts in the preparation of root canal systems: a review", J Endod, 30(8), 559–567 (2004).
[13] M. Mancini, et al., "FESEM evaluation of smear layer removal from conservatively shaped canals: laser-activated irrigation (PIPS and SWEEPS) compared to sonic and passive ultrasonic activation—an ex vivo study", BMC Oral Health, 21(1), 81 (2021). doi:10.1186/s12903-021-01427-0.
[14] G. I. Ibrahim and H. A. Jawad, "Investigating the effect of Er,Cr:YSGG laser agitation of sodium hypochlorite on the removal of mature biofilm in the complex root canal systems using atomic force microscopy", J Dent Res Dent Clin Dent Prospect, 17(3), 154–161 (2023). doi:10.34172/joddd.2023.40463.
[15] I. Papoulidou, et al., "Evaluation of Er,Cr:YSGG laser technique for fiber post removal of endodontically treated teeth using micro-computed tomography", Microsc Res Tech, 86(7), 803–812 (2023). doi:10.1002/jemt.24340.
[16] S. S. Al-Karadaghi and H. A. Jawad, "Debonding of LDSVs utilizing Er,Cr:YSGG laser irradiation with fractional technique: an in vitro study", Aust Dent J, 68(2), 125–134 (2023). doi:10.1111/adj.12958.
[17] S. S. Al-Karadaghi, H. A. Jawad, and T. Al-Karadaghi, "The influence of pulse duration and exposure time of Er,Cr:YSGG laser on lithium disilicate laminate debonding, an in vitro study", Heliyon, 9(3), e14600 (2023). doi:10.1016/j.heliyon.2023.e14600.
[18] T. S. Al-Qaradaghi, A. S. Mahmood, and R. N. Dayem, "The Efficacy of Er:YAG Laser on Intrapulpal Temperature Rise of Class V Cavity Preparation", IJL, 10(B), 9–14 (2011). doi:10.31900/ijl.v10iB.97.
[19] M. Suk, et al., "The efficacy of photon-initiated photoacoustic streaming in the removal of calcium silicate-based filling remnants from the root canal after rotary retreatment", Lasers Med Sci, 32(9), 2055–2062 (2017). doi:10.1007/s10103-017-2325-4.
[20] S. S. Rashid and H. A. Jawad, "Radicular dentine permeability using short pulsed Er,Cr:YSGG laser with PIPS technique", J Res Med Dent Sci, 9(7), 228–234 (2021).
[21] S.S. Rasheed, H.A. Jawad, "Smear Layer Removal from the apical third using the Er,Cr:YSGG photon-induced photoacoustic streaming", Iran Endod J, 16(4), 238–43 (2021).
[22] M.F. Scelza, J.M. Coil, A.C. Maciel, L.R. Oliveira., P. Scelza, "Comparative SEM evaluation of three solvents used in endodontic retreatment: an ex vivo study", J Appl Oral Sci, 16(1), 24–9 (2008).
[23] R. Yang, Y. Han, Z. Liu, et al, "Comparison of the efficacy of laser-activated and ultrasonic-activated techniques for the removal of tricalcium silicate-based sealers and gutta-percha in root canal retreatment: a microtomography and scanning electron microscopy study", BMC Oral Health, 21, 275 (2021).
[24] R.A. Almohareb, et al, "Efficiency of diode laser and ultrasonic-activated irrigation in retreatment of gutta percha and bioceramic sealer: An in vitro study", Aust Endod J, 49(2), 318–23 (2023).
[25] H.Y. Hassan, F.M. Hadhoud, A. Mandorah, "Retreatment of XP-endo shaper and r-endo files in curved root canals", BMC Oral Health, 23(1), 38 (2023).
[26] D.N. Abdulhussein, A.M.J.Al Haidar, "Preventive effect of combined Er,Cr:YSGG and fluoride gel on acid resistance of the permanent tooth enamel: An in vitro study", J Clin Exp Dent, 15(3), e225–32 (2023).
[27] P. Betancourt, et al, "Er,Cr:YSGG laser-activated irrigation and passive ultrasonic irrigation: comparison of two strategies for root canal disinfection", Photobiomodul Photomed Laser Surg, 38(2), 91–7 (2020).

[28] Y. L Ng., V. Mann, K.Gulabivala, "A prospective study of the factors affecting outcomes of nonsurgical root canal treatment: Part 1: Periapical health", Int Endod J, 44, 583–609 (2011).
[29] S. Friedman, A. Stabholz, Tamse A, "Endodontic retreatment–case selection and technique. Part 3: Retreatment techniques", J Endod, 16, 543-9 (1990).
[30] C. DeLong, J. He, K.F. Woodmansey, "The effect of obturation technique on the push-out bond strength of calcium silicate sealers", J Endod, 41, 385–8 (2015).
[31] F. Somma, G. Cammarota, G. Plotino, N.M. Grande, C.H. Pameijer, "The effectiveness of manual and mechanical instrumentation for the retreatment of three different root canal filling materials", J Endod, 34(4), 466–9 (2008).
[32] M.E. Zaghloul, T.Y. Abdelrahman, M.F. Obeid , "The Efficiency of passive ultrasonic activated irrigation on the retrievability of guttaflow bioseal: in vitro study", Future Dent J, 10(1), 9–14 (2024).
[33] A. Lloyd, J.P. Uhles, D.J. Clement, F. Garcia-Godoy, "Elimination of intracanal tissue and debris through a novel laser-activated system assessed using high-resolution micro-computed tomography: a pilot study", J Endod, 40(4), 584–7 (2014).
[34] V. Badami, et al, "Efficacy of laser-activated irrigation versus ultrasonic-activated irrigation: A Systematic Review", Cureus, 15(3), e36352 (2023).
[35] K.M Galler., et al, "Penetration depth of irrigants into root dentine after sonic, ultrasonic and photoacoustic activation", Int Endod J, 52(8), 1210–7 (2019).
[36] R.C.D. Swimberghe , et al, "Explaining the working mechanism of laser-activated irrigation and its action on microbial biofilms: a high-speed imaging study", Int Endod J, 55, 1372–84 (2022).
[37] P. Gregorčič, N. Lukač, J. Možina, and M. Jezeršek, "In vitro study of the erbium: yttrium aluminum garnet laser cleaning of root canal by the use of shadow photography", J Biomed Opt, 21, 15008 (2016).
[38] A. K. Airani, et al, "Ability of laser in removing gutta percha from root canal using chloroform and endosolv", Int J Health Sci, 6(S4), 4713–8 (2022).
[39] Z. Mohammadi, S. Shalavi, A. Moeintaghavi, H. Jafarzadeh, "A review over benefits and drawbacks of combining sodium hypochlorite with other endodontic materials", Open Dent J, 11, 661–9 (2017).

ازالة بقايا مادة البايوسيراميك سيلر باستخدام إشعاع ليزرEr,Cr:YSGG بتقنية PIPS في دراسة مختبرية

سارة سامي، حسين علي جواد

معهد الليزر للدراسات العليا ، جامعة بغداد، بغداد، العراق .

.

البريد الالكتروني للباحث: sara.sami2202m@ilps.uobaghdad.edu.iq

الخلاصة : هدفت هذه الدراسة المختبرية إلى تقييم فعالية استخدام الري المنشَّط بأشعة ليزر Er,Cr:YSGG في إزالة بقايا حشوات القناة الجذرية أثناء إعادة المعالجة اللبّية. اعتمدت التقنية على مبدأ التدفق الضوئي الصوتي المحفَّز بالفوتون (PIPS) باستخدام مدة نبضة تبلغ 700 ميكروثانية لتنشيط محلول هيبوكلورايت الصوديوم بتركيز 2.5% (NaOCl) ومحلول EDTA بتركيز 17%.
شملت الدراسة واحدًا وعشرين سنًا دائمًا مستأصلاً من الضواحك العلوية والسفلية أحادية الجذر. تم تنظيف القنوات وتشكيلها ثم حشوها باستخدام الجاتا بيركا وسيلر بيوسيراميكي. بعد ذلك، أُجريت إعادة المعالجة باستخدام ملفات النيكل-تيتانيوم الدوّارة (XP-endo Retreatment)، ثم قُسِّمت الأسنان عشوائيًا إلى ثلاث مجموعات (7 عينات لكل مجموعة) وفقًا لطريقة الري المستخدمة:
المجموعة الأولى: الري التقليدي بالحقنة (المجموعة الضابطة).
المجموعة الثانية: الري بالأمواج فوق الصوتية الساكنة.
المجموعة الثالثة: الري المنشَّط بالليزر باستخدام جهاز Er,Cr:YSGG بطول موجي 2780 نانومتر، مدة نبضة 700 ميكروثانية، تردد 5 هرتز، طاقة 1 واط، باستخدام رأس RFT2 وبدون رذاذ هواء أو ماء.

تم شطر العينات طوليًا وفحصها باستخدام المجهر الإلكتروني الماسح (SEM) لتقييم كمية بقايا الحشوات المتبقية في الثلث التاجي، الأوسط، والقِمي من القناة الجذرية. تم تقييم النظافة من قبل اثنين من أخصائيي علاج الجذور المعايرين باستخدام نظام تقييم مكون من أربع درجات. وقد أُجري التحليل الإحصائي باستخدام اختبار ANOVA وتحليل Tukey للمقارنات البعدية، مع تحديد مستوى الدلالة عند ($\alpha = 0.05$).

أظهرت النتائج وجود فروق ذات دلالة إحصائية بين المجموعات ($P < 0.05$)، حيث سجّلت المجموعة الثالثة انخفاضًا ملحوظًا في كمية البقايا المتبقية مقارنةً بالمجموعتين الأولى والثانية، في جميع مستويات القناة. بينما لم تُسجل فروق معنوية بين المجموعتين الأولى والثانية ($P > 0.05$)، مما يشير إلى محدودية فاعلية الري فوق الصوتي مقارنة بالتنشيط الليزري. كما لوحظ أن أفضل النتائج من حيث النظافة كانت في الثلث التاجي، تليها المنطقة الوسطى، ثم القِمية.

أظهر الري المنشط بالليزر باستخدام جهاز Er,Cr:YSGG مع تقنية PIPS ومدة نبضة 700 ميكروثانية، بالتزامن مع استخدام NaOCl بتركيز 2.5% وEDTA بتركيز 17%، فاعلية عالية في إزالة بقايا حشوات الجذر خلال إعادة المعالجة. وتشير هذه النتائج إلى أن استخدام هذه التقنية يمكن أن يُعد خيارًا فعالًا مساعدًا ضمن بروتوكولات إعادة المعالجة التقليدية، لما يوفره من كفاءة تنظيف محسّنة في جميع أجزاء القناة الجذرية.

IJL, Issue 2, Vol. 24, 2025
https://doi.org/10.31900/ijl.v24i2.542

Research Article

IRAQI JOURNAL OF LASER

Evaluation of Nd:YAG Laser Spot Welding for Dissimilar Joining of Nickel and Nickel-Coated Copper in Busbar Lithium-Ion Batteries

Vian Jabbar Jumaah[1,2,] *, Ziad Aeyad Taha[1], Levent Candan[3], Ersin Kayahan[3]

[1]*Institute of Laser for Postgraduate Studies, University of Baghdad, Baghdad, Iraq*
[2] *Department of Construction and Projects, Al-Nahrain University, Baghdad, Iraq*
[3]*Laser Technologies Research and Application Center (LATARUM), Kocaeli University, 41275, Yeniköy, Kocaeli, Turkey*
*****Email address of the Corresponding author*: vzangana@nahrainuniv.edu.iq

Article history: Received 17 Jun. 2025; Revised 29 Aug. 2025; Accepted 3 Sept. 2025; Published online 15 Dec. 2025

Abstract: This study aims to evaluate the feasibility of using pulsed Nd:YAG laser spot welding to join dissimilar metals consisting of nickel and nickel-plated copper in busbar joints for lithium-ion batteries. The effects of key operating parameters, namely laser energy, pulse repetition rate, and focal position, on the mechanical and structural properties of the weld were examined. The results showed that an energy of 13 joules achieved the highest peak shear force of approximately 273 N with a homogeneous melt zone and limited surface defects, while an energy of 10 joules recorded the highest hardness value (370HV0.300) due to the balance between energy input and cooling rate. It was also found that a repetition rate of 20 Hz and a focal position at 0 mm represent the optimal conditions for obtaining stable mechanical and microstructural properties. Although the results confirm the possibility of obtaining high-quality welds using this technique, full reliability verification requires further analysis through scanning electron microscopy (SEM), phase analysis (EDS/XRD), and fracture pattern studies to determine failure locations. The study also recommends conducting additional experiments to assess long-term performance under various operating conditions such as vibration, temperature fluctuations, and humidity. Thus, this work contributes a scientific basis that can be relied upon to develop more reliable manufacturing processes in modern battery applications.

Keywords: Nd: YAG laser, spot laser welding, Nickel-coated copper, Lithium-ion batteries, mechanical properties.

1. Introduction

Lithium-ion batteries (LIBs) have become the leading technology in energy storage for a wide range of applications, from portable electronic devices to electric vehicles, due to their high energy density, long service life, and excellent efficiency [1]. In such batteries, the electrical connection process between the busbar and the electrode tabs represents a crucial element in ensuring the system's reliability, safety, and long-term performance, as weak or failed weld joints lead to increased electrical resistance, localized hot spots, and possibly premature battery failure. Laser welding techniques have become fundamental methods in modern manufacturing, enabling high speed with limited thermal distortion and minor metallic degradation compared to traditional methods [2,3]. Furthermore, the advancements in laser welding and robotics have provided greater accuracy, flexibility, and higher speed in industrial applications [4]. Pulsed

Nd:YAG laser usage is among the most common choices due to its high efficiency in absorbing reflective metals such as nickel and copper, making it suitable for welding various alloys in battery and electrical applications [5-7].

In contrast, traditional welding methods such as resistance spot welding and ultrasonic welding are less costly and easier to operate, but face significant challenges when used with metals of high thermal conductivity like nickel and nickel-plated copper. Resistance spot welding suffers from electrode wear, poor weld stability, and heat accumulation, whereas ultrasonic welding may lead to weak interfacial bonding or delamination in thin metal sheets. These limitations justify resorting to laser welding despite its relatively higher cost. Nevertheless, welding nickel to nickel-plated copper remains a challenge due to differences in thermal properties, melting points, and reflectivity, which may cause asymmetric weld pools, formation of brittle intermetallic compounds, and development of cracks or porosity in the weld. Numerous studies have addressed dissimilar metal welding in battery applications such as Ni–Al, Cu–Al, and Ni–Cu joints, demonstrating the possibility of improving shear strength, microstructure, and defect control by selecting optimal operating conditions [8–17]. However, research directly focusing on welding nickel to nickel-plated copper remains limited, despite the widespread industrial use of these joints in tab-to-busbar connections in lithium-ion batteries.

Accordingly, this research aims to optimize the parameters of pulsed Nd:YAG laser spot welding for joining nickel to nickel-plated copper, focusing on identifying optimal conditions that achieve high mechanical strength while minimizing surface and structural defects. Through a systematic evaluation of the effects of pulse energy, repetition frequency, and focal distance on shear strength, microhardness distribution, and microstructure, this work seeks to bridge the existing research gap and provide a scientific and practical foundation that can be relied upon in industrial battery manufacturing.

2. Materials

In this study, nickel-coated copper with a thickness of 0.3 mm, sourced from Tata Steel, was utilized as the tab material, along with nickel having a thickness of 0.15 mm. The chemical compositions of these materials are presented in Table 1. The welds were produced in an overlap joint configuration, with the thinner nickel layer positioned on top of the nickel-coated copper layer. The dimensions of the nickel-coated copper and nickel materials were (50 mm × 10 mm × 0.3 mm) and (50 mm × 8 mm × 0.15 mm), respectively with the nickel side facing the laser source. As shown in Figure 1.

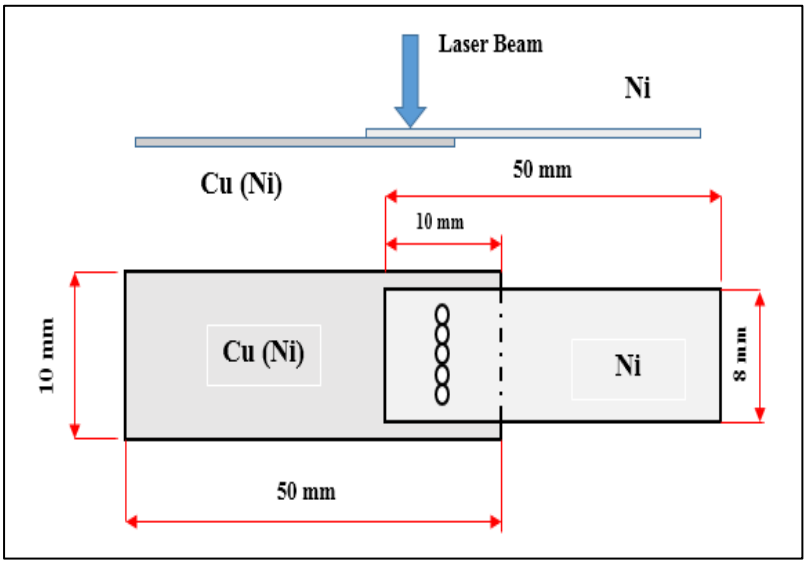

Figure 1: The spot-welding configuration.

Table 1: The chemical composition of Cu (Ni) and Ni materials is based on certifications of Tata Steel and Evek Gmbh, and represents the standard composition as supplied.

Cu (Ni)	Cu	Bi	Pb	Sg	Ni (coated)			
Ni	≥ 99,95 %	≤ 0,0005 %	≤ 0,005 %	≤ 0,030 %	≥ 99,99 %			
	Cu	C	Si	Mn	Ni	Ti	Mg	Fe
	≤0.25	≤ 0.1	≤0.25	≤0.35	≥ 99,2 %	≤0.1	≤0.15	≤0.4

3. Experimental setup and methods

The GSI Lumonics JK760TR Series Laser, an Nd:YAG industrial laser with a wavelength of 1.064 μm, turned into employed for welding. It operates with a mean power of 600 W, peak power of 10 kW, pulse duration of up to 50 ms, and a maximum repetition rate of 500 Hz.

To make sure unique alignment and minimize air gaps, the two plates were firmly secured in a custom clamp. In this setup, a nickel (Ni) plate becomes positioned over a nickel-coated copper (Cu (Ni)) plate, as illustrated in Figure 2. The laser spot at the focus into positioned at the surface of the nickel sheets with a standoff distance of 160 mm and 1.42 mm, the distance between the center of spot and other center and the diameter of the spot of the weld is 0.45mm. No protective shielding gas became used all through the welding process.

Figure 2: schematic of the experimental setup.

A systematic examination of diverse manner parameter units was conducted to gain great stitch welds. Multiple checks have been achieved to perceive the most reliable welding parameters for high-performance joints.

Tables 2 summarize the different parameter sets evaluated, focusing on the outcomes of power, frequency, and focal length with constant pulse duration at 5 ms.

Table 2: Parameters for three groups of welding using different parameters.

Sample No.	Energy (J)	Frequency (Hz)	Focal length (mm)
1	6	20	0
2	8	20	0
3	10	20	0
4	11	20	0
5	13	20	0
6	16	20	0
7	10	10	0
8	10	15	0
9	10	20	0
10	10	30	0
11	10	40	0
12	10	50	0
13	10	20	0
14	10	20	-1
15	10	20	-2
16	10	20	-3
17	10	20	-4
18	10	20	-5

4. Result and Discussion

4.1 Tensile shear test results

The weld joint's mechanical strength under shear loading was evaluated using a tensile shear test. For this evaluation, a uniaxial testing machine (INSTRON, max load capacity: 5 kN) was used. Data for the load displacement curves were obtained by continuously increasing the crosshead speed of the machine until the joint failed, while monitoring the load and displacement.

A. Effect of Energy

The tensile test results (Figure 3) and stress–strain curves (Figure 4) revealed a progressive improvement in weld performance with increasing laser energy. The minimum fracture force at 6 J (41.47 N) indicates a weak bond resulting from insufficient surface fusion (see Figure 5a). Only superficial fusion is observed, which explains the low strength. This low value is consistent with the literature, which suggests that sub-critical energy levels lead to the formation of weak mechanical joints due to inadequate thermal interaction between the surfaces [18].

With an increase in energy to 8 J, a significant improvement in strength is observed, reaching 181.74 N, indicating a notable enhancement in bonding quality (see figure 5 b). Higher energy leads to deeper and more stable fusion. At 10 J, the strength continues to increase to 264.02 N, which signals that the material has entered an effective energy window in which the melting depth balances with thermal conductivity without introducing significant structural defects and at the optimal condition of 13 J, the strength reaches the highest recorded value (273.15 N), indicating a thermally stable process. Studies show that in this range, deep and clean fusion is achieved without the formation of critical defects [19]. (see figure 5 c and e) the cross-sections show relatively deep fusion zones (~159 µm and 215 µm, respectively) corroborating the high mechanical performance.

However, at 11 J, a sudden drop in strength to 153.42 N is recorded despite the increase in energy. This is likely attributed to the initiation of microscopic defects such as porosity or microcracks. Multiple studies, including that of [20], confirm that exceeding a certain energy threshold causes instability in the keyhole regime, leading to gas entrapment and localized collapses that result in porosity formation. (see Figure 5 d) the images reveal signs of microscopic defects, particularly scattered porosity and cracking, which align with the recorded reductions in tensile strength. At 16 J, mechanical performance declines to

231.4 N despite the increase in laser energy. This is due to the increase in thermal porosity and surface shrinkage caused by rapid cooling-phenomena commonly observed in pulsed laser welding when the optimal energy threshold is exceeded [21].

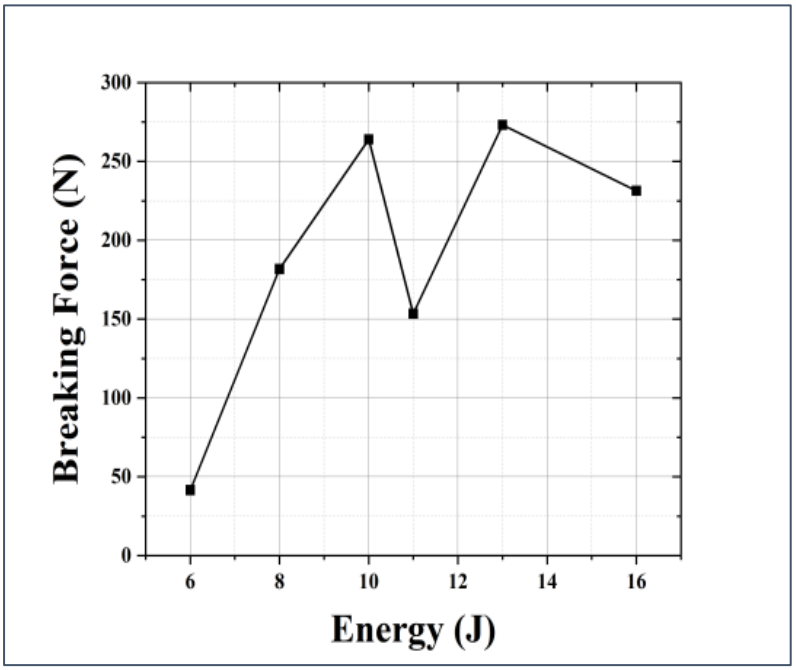

Figure 3: Breaking force versus work energy at constant pulse repetition rate and focal length.

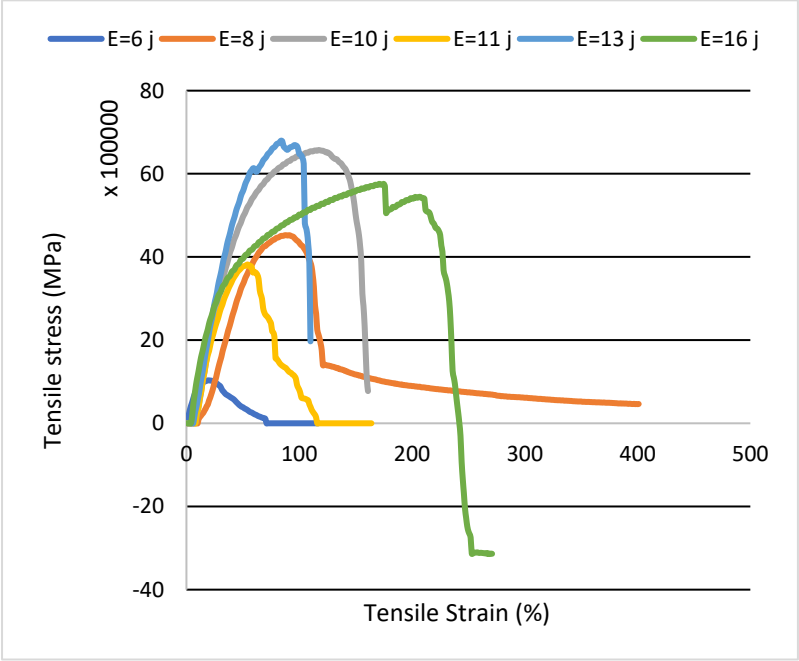

Figure 4: Stress-Strain diagram at different energies.

The stress–strain curve for the 6 J specimen shows a very brittle behavior with rapid failure upon minimal loading. Meanwhile, the curves for 10 J and 13 J display high tensile capacity and extended strain before failure, indicating a strong metallurgical bond capable of effective stress distribution.

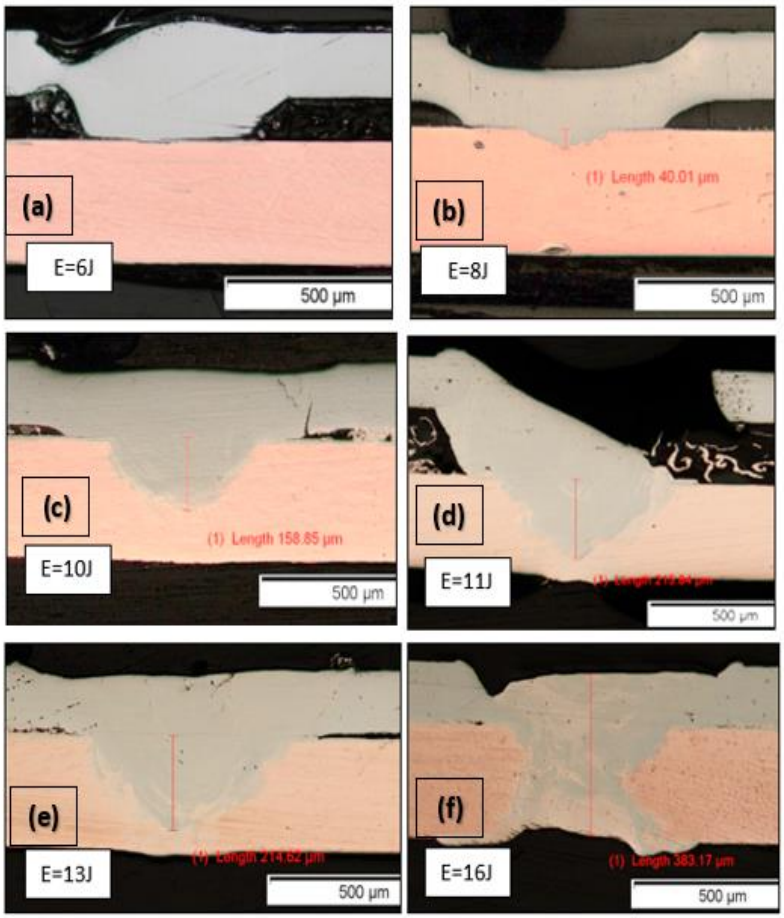

Figure 5: Microscopic images of the weld zones between Ni and Cu (Ni) at different laser energy levels, captured at 5x magnification.

The 11 J curve reveals evident weakness in ductility, reinforcing the assumption of internal defects causing premature failure. Similarly, the 16 J curve shows initially stiff behavior followed by abrupt failure, most likely due to the presence of pores acting as stress concentration points. These results confirm the presence of an "optimal energy window" in the range of 10–13 J, which is necessary to balance adequate penetration and minimize thermal defects, thereby enhancing the mechanical strength of the welded joint.

B. Effect of Pulse Repetition Rate

Figure 6 illustrates the relationship between PRR and fracturing force. At PRR = 10 Hz, the fracture force is at its lowest (70.73 N), indicating a weak bond. Low repetition rates fail to deposit sufficient thermal energy over time to form a stable weld pool, leading to surface-only fusion and likely incomplete bonding [22]. Increasing PRR to 15 Hz raises the force to 172.88 N, suggesting more uniform material fusion due to enhanced heat input and penetration .The peak fracture strength occurs at PRR = 20 Hz, reaching 264.02 N—a clear mechanical optimum. This supports a theory of optimal energy-time balance during welding, creating deep fusion zones without defects such as porosity or cracks [23]. Beyond this point, at PRR = 30 Hz, strength unexpectedly drops to 115.70 N. This decline is attributable to heat saturation in the weld zone,

causing keyhole instability, trapped gas, and micro-porosity [21, 24]. (see figure 7c) PRR = 20 Hz and 30 Hz have deeper weld penetration (≈159μm and 245 μm, respectively) compared to 10 Hz and 50 Hz. However, cracks and heterogeneity at 30 Hz explain its lower strength despite penetration depth.

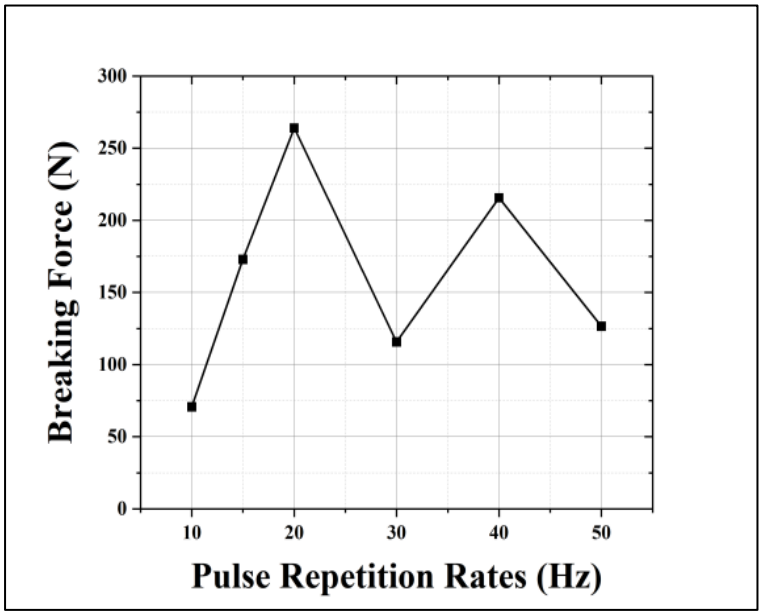

Figure 6: Breaking force versus work pulse repetition rate at constant energy and focal length.

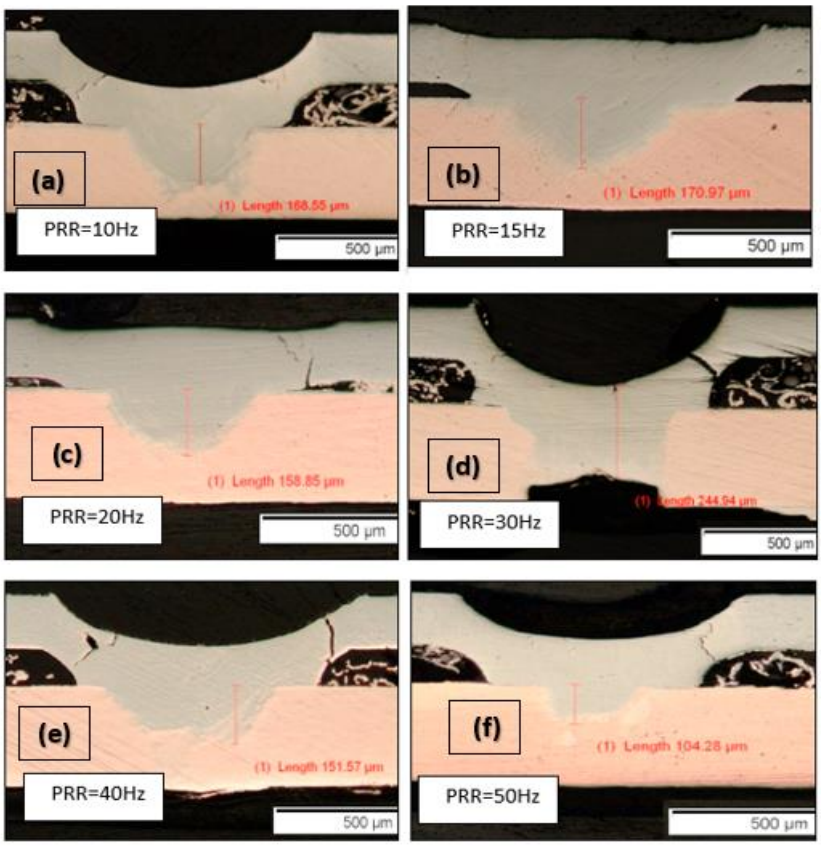

Figure 7: Microscopic images of the weld zones between Ni and Cu (Ni) at different pules repetition rate levels, captured at 5x magnification.

At PRR = 40 Hz, strength partially recovers to 215.60 N—suggesting some regained thermal stability though limited. However, at PRR = 50 Hz, strength falls again to 126.60 N due to unstable heat accumulation and thermally induced defects resulting from rapid thermal cycles (see figure 7 f), penetration is shallow (≈104 µm), confirming inadequate fusion.

This non-linear trend matches the stress–strain curves (Figure 8). PRR = 20 Hz produces the highest maximal stress and strain before fracture, indicative of a robust weld. PRR = 30 Hz and 50 Hz yield brittle behavior and early failure, confirming defect accumulation.

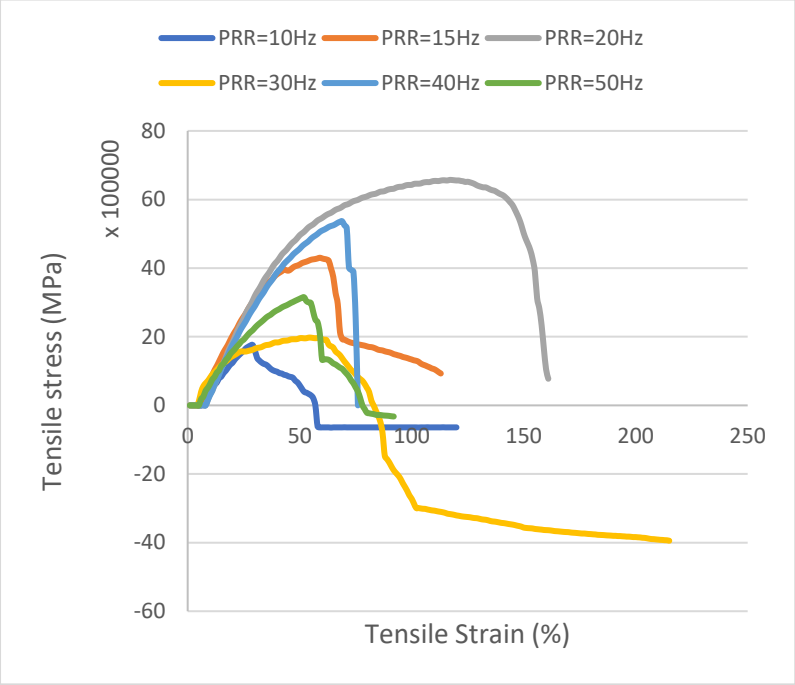

Figure 8: Stress Strain diagram at different pulse repetition rate**.**

Together, these results suggest an optimal PRR near 20 Hz, which balances heat input and dissipation to produce the highest mechanical and structural quality weld. Deviations from this rate in either direction result in defective microstructures and reduced performance.

C. Effect of Focal Length

Based on the data presented in Figure 9, it is evident that laser focal position is a critical factor in determining the mechanical performance of the welded specimen, particularly the maximum fracture force. At zero defocus (0 mm), i.e., when the laser focus is precisely positioned at the interface between the two parts, the highest recorded fracture force (264 N) is achieved. This reflects the formation of a strong metallurgical bond because of complete thermal fusion. The high strength is attributed to the uniform distribution of energy within the keyhole, enabling deep and stable melting followed by gradual solidification, which reduces residual thermal stresses. These findings align with those reported by who emphasized that surface-focused laser positions enhance keyhole stability and minimize disturbances, thereby reducing porosity formation [25].

As the laser focal point shifts downward into the material (negative defocus), the fracture strength decreases progressively: 235 N at –1 mm, 193 N at –2 mm, and finally 108 N at –3 mm. This sharp decline indicates a significant reduction in fusion efficiency due to the decreased power density at the joint interface, as the laser beam spreads over a larger area, lowering the effective energy per unit surface. The resulting

thermal dispersion leads to narrower and shallower fusion zones and increases the likelihood of structural defects, particularly porosity caused by trapped gases or evaporation of high-conductivity materials (see Figure 10). This interpretation is supported by multiple studies [26], who found that defocusing the laser from the optimal position significantly reduced shear strength in fiber laser welding of DP600 dual-phase steel, due to limited transverse thermal conduction and the emergence of fine cracks near the weld seam.

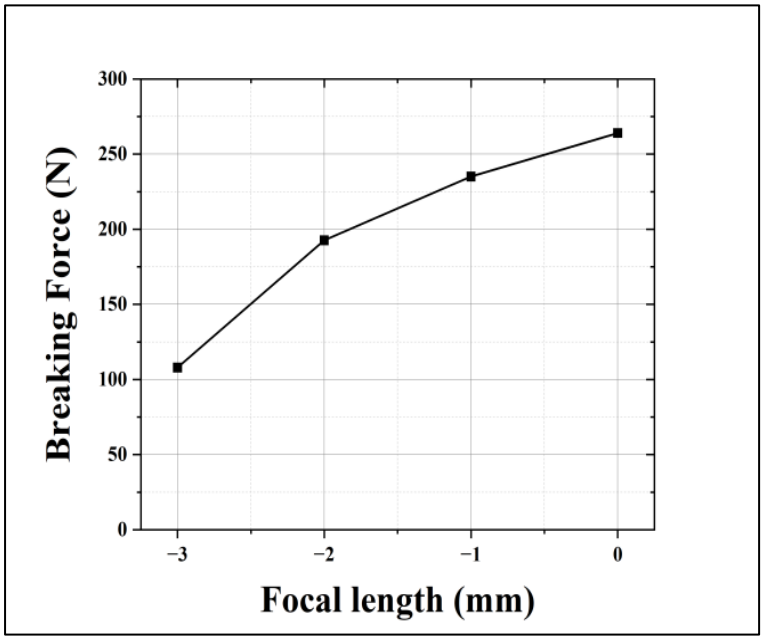

Figure 9: Breaking force versus focal length at constant energy and pulse repetition rate.

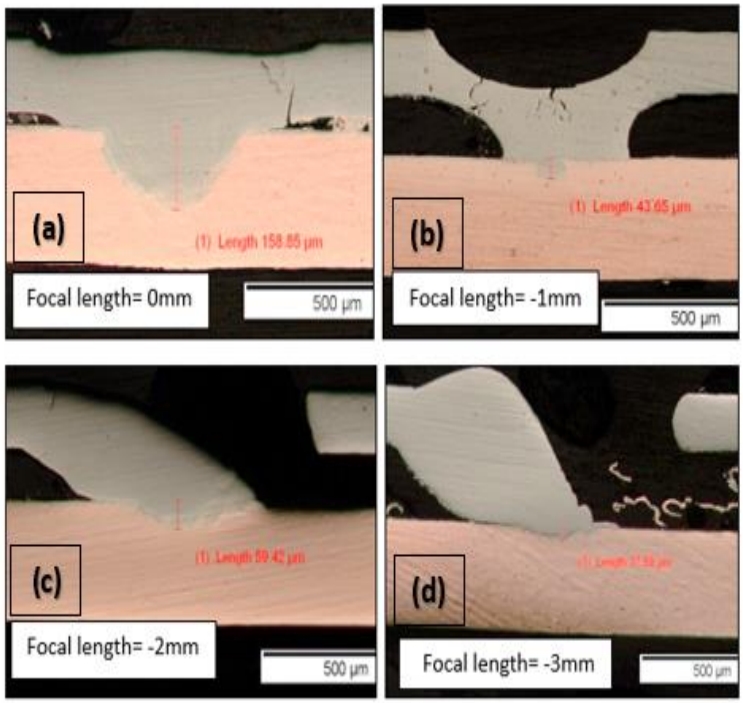

Figure 10: Microscopic images of the weld zones between Ni and Cu (Ni) at different focal length levels, captured at 5x magnification.

The tensile stress–strain curves in Figure 11 reinforce this mechanical analysis by illustrating the deformation behavior of the joint at different focal positions. At 0 mm, the curve exhibits extended strain with a peak stress of about 70 MPa, indicating a strong and ductile joint capable of accommodating significant deformation before failure. At –1 mm, the peak stress drops to around 60 MPa, while still maintaining moderate ductility. This trend continues at –2 mm with a peak of ~50 MPa and reduced elongation, showing early signs of brittle behavior. At –3 mm, the sample fails at ~30 MPa with negligible elongation, reflecting high porosity and microcracking caused by fusion instability. These observations are consistent with the findings who linked reductions in tensile strength and ductility in Cu–Ni alloy welds to porosity distributed along the weld line due to unstable thermal conditions [27].

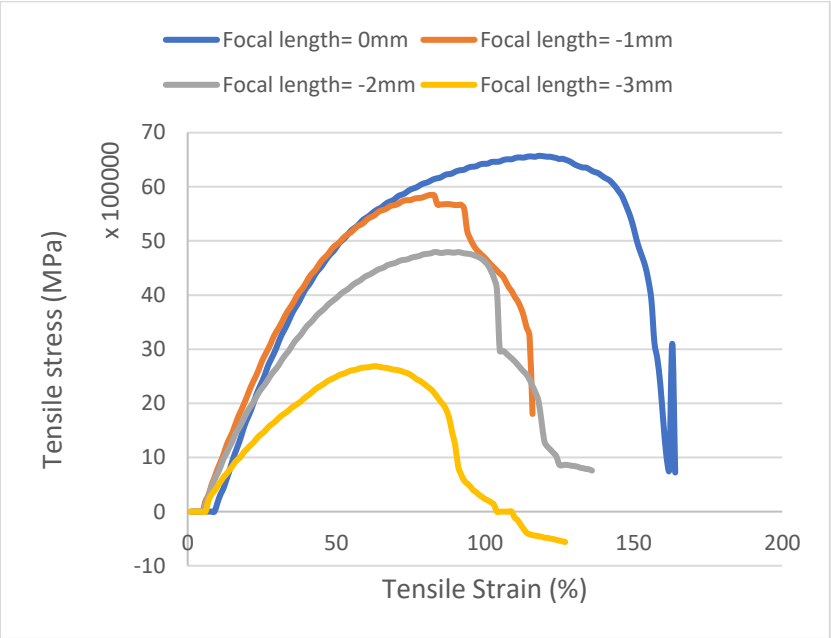

Figure 11: Stress-Strain diagram at different focal lengths**.**

4.2 Micro hardness test results

The hard distribution in the weld cross-section was evaluated using a HARDWAY HVD-1000 AD tester using a 300-gf load. Microhardness testing is a basic mechanical evaluation technique. This is necessary for material characterization following welding and other manufacturing processes. A measurement of resistance to deformation, which provides an important check on the strength and uniformity of a material's internal structure.

A. Effect of Energy

The microhardness graph (Figure 12) clearly shows that hardness is strongly influenced by the applied laser energy. At low energy (6 J), the sample exhibits relatively low hardness at the weld, with a sharp increase at the center line. This suggests a narrow fusion zone and weak metallurgical bonding between the materials, which is also confirmed by the corresponding microscopic image (see Figure 5 a), where the fusion zone appears very limited. Such limited fusion contributes to weaker mechanical properties due to incomplete mixing of Ni and Cu.

At 8 J, the hardness at the weld center improves, reaching over 350 HV. This improvement can be attributed to a greater amount of molten material and an increased cooling rate, resulting in the formation of fine-grained microstructures. This phenomenon has been documented in literature, where rapid solidification leads to grain refinement, thereby enhancing hardness [28].

The corresponding micrograph (see Figure 5 b) supports this, showing a slightly wider fusion zone (~40 µm) than at 6J.

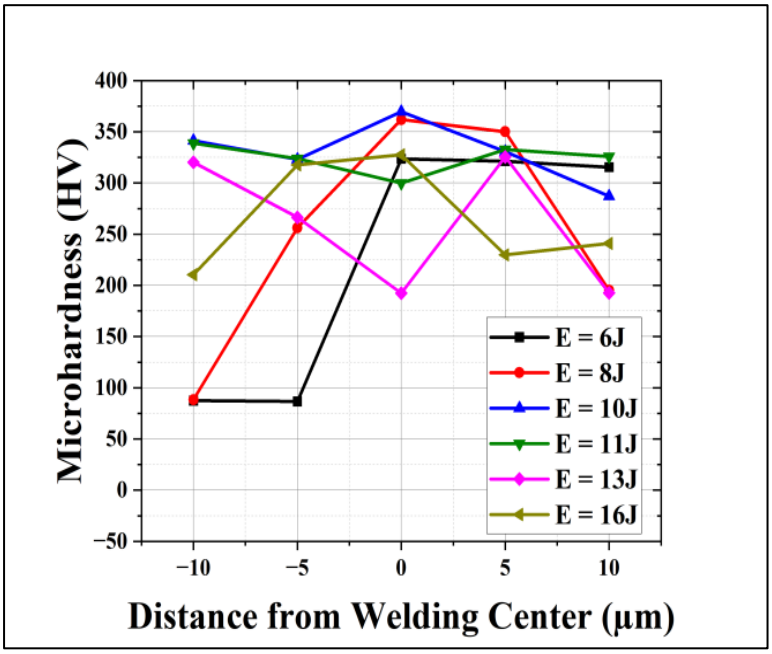

Figure 12: Micro hardness versus distance from welding center for different Energy level.

At 10 J, the highest microhardness (~370 HV) is recorded at the weld center, indicating an optimal balance between energy input and cooling rate, which results in a refined and cohesive weld structure. The microscopic image for this energy level (see Figure 5 c) shows a significantly wider fusion zone (~158.85 µm), which promotes better metallurgical bonding between Ni and Cu, and improves mechanical performance, particularly hardness. As the energy increases to 11 J, the hardness decreases; however, the micrograph reveals an irregular fusion boundary and signs of excessive melting, indicating the onset of thermal instability (see Figure 5 d). This aligns with findings in laser welding studies, where surpassing optimal energy levels leads to microstructural disturbances [21]. The variation in hardness at this stage suggests the emergence of zones with inconsistent mechanical properties.

On 13 J, there is a noticeable drop in hardness (~250 HV) at the weld center, with increased variability across the weld zone. This is likely due to overheating, which promotes the formation of coarse grains because of slower cooling rates. The corresponding microscopic image (see Figure 5 e) shows a clearly expanded fusion zone (~214.62 µm), with visible distortion at the weld interface.

At the highest energy level (16 J), hardness continues to decline to below 350 HV at the weld center. This degradation is attributed to negative effects of excessive heat, including microcracks and porosity caused by localized vaporization or over melting [29]. The micrograph for this condition (see Figure 5 f) reveals an extensively broadened fusion zone (~383.17 µm), with notable microstructural irregularities, which supports the observed decline in microhardness. Based on the graph and microstructural observations, 10 J appears to represent the optimal energy level, providing the best mechanical properties through balanced heat input and rapid solidification. Lower or higher energy levels result in poorer outcomes due to either insufficient fusion or excessive thermal effects, respectively.

B. Effect of Pulse Repetition Rate

Based on Figure 13, it is evident that the microhardness of Ni-Cu(Ni) laser welds is significantly influenced by the pulse repetition rate (PRR). Variations in PRR affect the thermal input, cooling rates, and consequently, the microstructure and presence of defects such as microcracks and porosity. The

microhardness trends correlate with the observed microstructural features, providing insights into the weld quality under different PRR conditions.

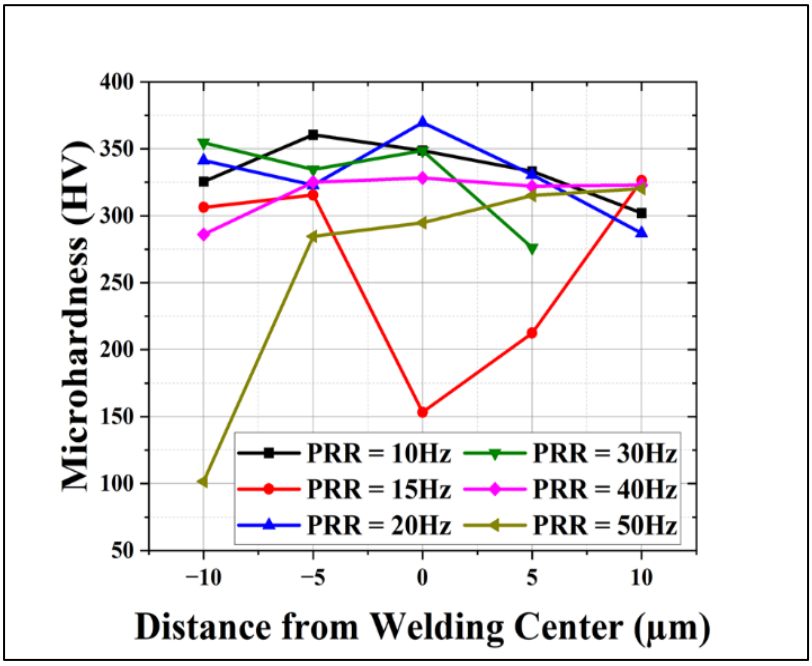

Figure 13: Micro hardness versus distance from welding center for different pulse repetition rate level.

At PRR = 10 Hz this repetition rate, the weld exhibited a high and uniform microhardness (~350 HV) at the weld center. The corresponding microscope (see figure 7 a) shows a homogeneous fusion zone approximately 168.5 μm wide, free from visible cracks or pores. The fine-grained microstructure suggests rapid cooling, leading to improved mechanical properties. This observation aligns with findings who noted that rapid cooling in laser welding promotes fine grain formation, enhancing hardness [28].

An increase in PRR to 15 Hz resulted in a decrease in microhardness at the weld center (~153HV). The micrograph reveals the initiation of micro-porosity within the fusion zone (see figure 7 b), likely due to gas entrapment during solidification. Such porosity can act as stress concentrators, reducing the mechanical strength of the weld. discusses the formation of porosity in laser welding because of rapid solidification trapping gases within the molten pool [21].

At 20 Hz, the weld achieved the highest microhardness (~370 HV) at the center. The fusion zone widened to approximately 158.85 μm (see figure 7c), displaying a fine-grained, defect-free microstructure. This optimal condition suggests a balanced thermal input and cooling rate, facilitating complete fusion and grain refinement. reported similar enhancements in microhardness due to refined microstructures achieved through controlled laser welding parameters [23].

Further increasing the PRR to 30 Hz led to a slight decrease in microhardness (~350 HV) the decrease in hardness at 30 Hz is not necessarily due to visible porosity or cracks, but may result from microscopic changes in the grain structure and cooling rate that depend sensitively on thermal conditions, which affect the hardness without causing obvious micro-defects in the microscopic images (see figure 7 d).

At 40 Hz, the microhardness stabilized at 325 HV. However, the microstructure exhibited increased porosity throughout the fusion zone, particularly near the fusion boundaries. The higher PRR likely led to insufficient time for gas escape, resulting in trapped pores. highlighted that higher laser parameters could increase porosity due to rapid solidification rates [30]. At the highest PRR of 50 Hz, the microhardness decreased to approximately 295 HV, and the fusion zone narrowed to about 104.28 μm (see figure 7f). The micrograph shows a combination of intensified porosity. These defects are attributed to excessive thermal

input leading to overheating, reduced cooling rates, and increased thermal stress. notes that excessive energy input in laser welding can cause such detrimental effects on weld integrity [21].
The analysis indicates that a PRR of 20 Hz offers the optimal balance between thermal input and cooling rate, resulting in the highest microhardness and a defect-free microstructure. Deviations from this optimal PRR, either lower or higher, lead to the formation of microstructural defects such as porosity and microcracks, adversely affecting the mechanical properties of the weld.

C. Effect of Focal Length

Figure 14 shows that the focal length plays a critical role in controlling the efficiency of laser welding for Ni + Cu (Ni) materials, as the mechanical properties and microstructure change significantly depending on the optical focus position. At FL = 0 mm, the highest microhardness (~369.6 HV) was recorded at the weld center, reflecting an ideal concentration of laser energy within the interaction zone. This led to the formation of a fine-grained structure because of a balanced melting and cooling rate (see figure 10a), the microscopic image that showed a clear and homogeneous fusion zone (~158.85 µm).

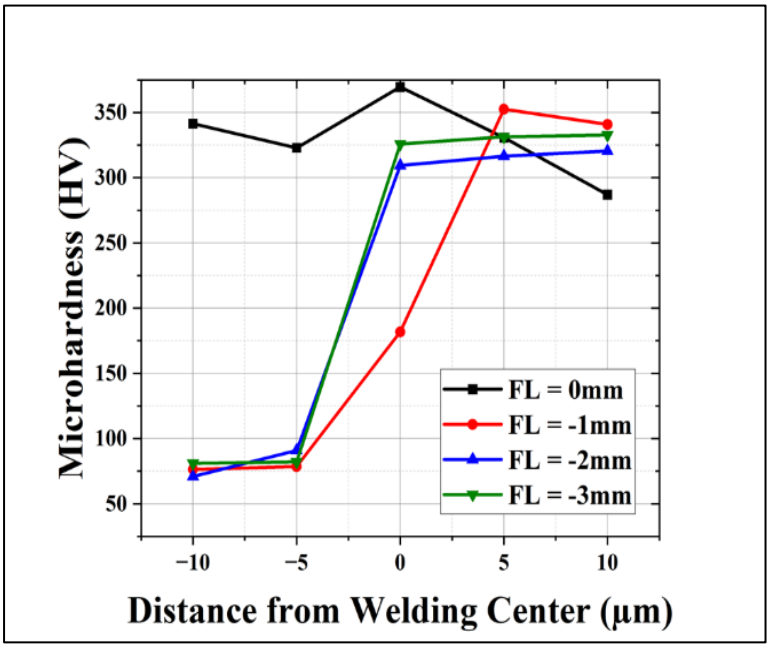

Figure 14: Micro hardness versus distance from welding center for different focal length level.

At FL = -1 mm, the hardness dropped sharply (~181.8 HV), which is attributed to the deviation of the laser beam from the optimal focal point, reducing thermal absorption efficiency and weakening the melting process. (see figure 10 b) The microscopic image for this condition supports the observed decrease in thermal interaction efficiency by showing a narrower fusion zone and a change in the solidification pattern. At FL = -2 mm and FL = -3 mm, a relative improvement in hardness was observed (~309.4 and 325.9 HV, respectively), indicating better distribution of deposited energy on the sample surface. However, the microscopic images revealed a change in the cooling pattern that may be associated with the buildup of internal thermal stresses, potentially leading to the formation of microcracks or microstructural changes at grain boundaries due to the physical interaction between Ni and Cu elements. It is noteworthy that at FL = -4 mm and -5 mm, no visible welding was achieved. This indicates that the laser beam failed to deposit sufficient energy at the interface, which aligns with the physical principle of decreasing power density as the beam moves away from the focal point. This confirms the existence of a critical focal window that must be maintained to ensure effective melting, as supported by previous studies on the influence of optical parameters on laser weld formation [21, 31].

These findings indicate a nonlinear relationship between focal length and welding efficiency, with FL = 0 mm emerging as the most suitable position for achieving stable welds and improved mechanical properties.

5. Conclusions

This study proved that the pulsed Nd:YAG laser welding technique represents a promising option for joining dissimilar metals (Ni/Cu (Ni)) in busbar joints for lithium-ion batteries, provided that operating parameters are precisely controlled. The results showed the following points:

1- Importance of operating parameters: It was concluded that laser energy is the most decisive factor in weld quality. An energy of 13 joules achieved the best mechanical performance (peak shear strength of 273 N) with a homogeneous melt zone and limited surface defects, while an energy of 10 joules achieved the highest hardness value (370 HV). This indicates the existence of an optimal operating window (10–13 joules) that balances melting depth and cooling rate.
2- Effect of pulse repetition rate (PRR): The results showed that 20 Hz is the optimal frequency, providing the highest shear strength and microhardness. Higher frequencies (30–50 Hz) led to thermal accumulation and instability in the weld pool, resulting in porosity and fine cracks, which explains the decline in mechanical performance despite increased penetration depth.
3- Role of focal position: It was found that the 0 mm focus position is optimal for achieving the highest weld strength and homogeneous hardness. Defocusing resulted in weakened metallurgical bonding and increased likelihood of structural defects due to energy dispersion.
4- Microscopic observations: Micrographs showed that the weld microstructure is directly affected by operating parameters; insufficient energy leads to inadequate surface melting areas, while exceeding the optimal energy limit results in porosity and cracks that reduce weld strength and durability.
5- Quality and reliability: Despite achieving high values of strength and hardness, establishing "high quality" welds requires supplementary analyses not included in this work, such as Scanning Electron Microscopy (SEM), elemental analysis (EDS/XRD), and fracture pattern study to determine failure locations. This was pointed out by the reviewer and is considered an essential step in future research.
6- Practical importance and recommendations: The results prove that pulsed Nd:YAG welding can provide reliable joints in battery applications, provided adherence to the optimal parameter window. Additional tests are recommended, including long-term performance under variable operating conditions (such as vibration, temperature fluctuation, and humidity), in addition to in-depth comparisons with previous studies to enhance scientific and practical reliability.

References

[1] M. C. Asirvatham, S. Collins, and I. Masters, "Laser wobble welding of steel to aluminium busbar joints for Li-ion battery packs", Optics and Laser Technology, 151, 108000 (2022).
[2] W. K. Hamoudi, A. K. Hamoudi, and S. A. Salih, "HAZ and melt limits of 3-D CO_2 laser welding", AQI J. Applied Physics, 6, 15-23 (2010).
[3] W. K. Hamoudi, A. K. Hamoudi, and S. A. Salih, "Modeling of 3-D keyhole CO_2 laser welding of steel", AQI J. Applied Physics, (ISSN 1813-2065), (2010).
[4] T. A. Tawfiq, Z. A. Taha, F. I. Hussein, and A. A. Shehab, "Spot welding of dissimilar metals using an automated Nd:YAG laser system", Iraqi J. Laser, Part A, 11, 1-5 (2012).
[5] T. A. Tawfiq, "Parametric optimization of pulsed Nd:YAG laser lap welding of stainless-steel ASTM A240/316L with carbon steel ASTM A570/Gr30", Al-Nahrain J. Engineering Sciences, 20, 27-35 (2017).
[6] A. K. Mahmoud, Z. A. Taha, and A. A. Shehab, "Temperature distribution simulation for pulsed laser spot welding of dissimilar stainless steel AISI 302 to low carbon steel AISI 1008", Advanced Materials Research, 445, 412-417 (2012).
[7] A. A. Shehab, S. K. Sadrnezhaad, A. K. Mahmoud, M. J. Torkamany, A. H. Kokabi, and M. Fakouri Hasanabadi, "Pulsed Nd:YAG laser dissimilar welding of Ti/Al 3105 alloys", Scientia Iranica B, 27, 1982-1994 (2020).
[8] A. Das, D. Li, D. Williams, and D. Greenwood, "Weldability and shear strength feasibility study for automotive electric vehicle battery tab interconnects", J. Brazilian Society of Mechanical Sciences and Engineering, 41, 54 (2019).

[9] N. Kumar, I. Masters, and A. Das, "In-depth evaluation of laser-welded similar and dissimilar material tab-to-busbar electrical interconnects for electric vehicle battery pack", J. Manufacturing Processes, 70, 78-96 (2021).
[10] E. Haddad, J. Helma, A. Olowinsky, and A. Gillner, "Nanosecond pulsed fiber laser as a tool for laser micro welding", Procedia CIRP, 94, 571-576 (2020).
[11] H.-M. Sung, S. Lee, D. Lee, H. Kim, S.-G. Kang, G.-D. Lee, K. Jeong, and N. Han, "Effect of the Ni plating on Al–Cu dissimilar metal laser welded joint", J. Materials Research and Technology, 31, 2473-2483 (2024).
[12] G. Horváth, A. Körmöczi, T. Szörényi, and Z. Geretovszky, "Laser welding and its implementation in the assembly of battery packs in aviation", Int. J. Sustainable Aviation, 6, 51-65 (2020).
[13] F. Yusof, Y. Miyashita, Y. Otsuka, Y. Farazila, W. Hua, and Y. Mutoh, "YAG laser spot welding of PET and metallic materials", (2015).
[14] A. A. Shehab, A. K. Mahmoud, S. K. Sadrnezhaad, M. J. Torkamany, and S. A. Jawad, "Pulsed Nd:YAG laser dissimilar welding of Grade 2 titanium alloy to 3105-O aluminum alloy using AlSi5 filler metal", (unpublished).
[15] A. Mannucci, I. Tomashchuk, V. Vignal, P. Sallamand, and M. Duband, "Parametric study of laser welding of copper to austenitic stainless steel", Procedia CIRP, 74, 450-455 (2018).
[16] G. Horváth, A. Körmöczi, T. Szörényi, and Z. Geretovszky, "Improvement of electrical and mechanical properties of laser welded lap joints via dimensional optimization", Int. J. Advanced Manufacturing Technology, 130, 1843-1854 (2024).
[17] N. Chen, H. Wang, J. Li, V. Liu, and J. Schroth, "Evolution of interfacial microstructure during resistance spot welding of Cu and Al with Ni-P coating", J. Manufacturing Science and Engineering, 144, 041001 (2021). [18] W. Meng, Z.G. Li, and F. Lu, "Porosity formation mechanism and its prevention in laser lap welding for T-joints", J. Mater. Process. Technol., 214, pp.1658–1664 (2014).
[19] Y. Shi, Z. Li, H. Sun, and X. Zhang, "Microstructural characteristics and mechanical properties of pulsed laser lap welded dissimilar joints", Opt. Lasers Eng., 131, 106002 (2020).
[20] B. Zhang and Y. Li, "Defect formation mechanisms in selective laser melting: a review", Chin. J. Mech. Eng., 30(3), pp.515–527 (2017).
[21] S. Katayama, Fundamentals of Laser Welding, Springer (2013).
[22] Y. Liu, Y. Wang, G. Chen, and J. Yang, "Effects of pulse laser parameters on weldability and mechanical performance of dissimilar metal joints", J. Manuf. Process., 35, pp.651–658 (2018).
[23] W. Zhang, H. Li, and D. Sun, "Effect of pulse frequency on microstructure and mechanical properties in pulsed laser welding of Ni–Cu dissimilar metals", Opt. Laser Technol., 139, 106943 (2021).
[24] M. Chludzinski, R.E. dos Santos, C. Churiaque, M. Ortega-Iguña, and J.M. Sánchez-Amaya, "Pulsed laser welding applied to metallic materials—A material approach", Metals, 11(4), 640 (2021).
[25] J. Xu et al., "Keyhole-induced porosity formation during laser welding", J. Mater. Process. Technol., 252, pp.720–727 (2017).
[26] E.S. Atmaca and A. Kurt, "The effects of welding speed and focal length on mechanical characteristic of fiber laser-welded structures of DP600 dual phase steel", GU J. Sci., Part A, 8(1), pp.146–156 (2021).
[27] M.P. Chakravarthy, N. Ramanaiah, and B.S.S. Rao, "Effect of laser welding on mechanical properties of 70/30 Cu-Ni alloy welds", Proc. Inst. Mech. Eng. Part B J. Eng. Manuf., 228(9), pp.1153–1161 (2014).
[28] S. Kou, Welding Metallurgy, 2nd ed., John Wiley & Sons, Hoboken, NJ (2003).
[29] J.R. Davis, ASM Handbook Volume 6: Welding, Brazing, and Soldering, ASM International (1993).
[30] Y. Zhang, H. Zhang, Y. Wu, and X. He, "Influence of laser welding parameters on the microstructure and mechanical properties of dissimilar joints", J. Manuf. Process., 35, pp.580–589 (2018).
[31] W.M. Steen and J. Mazumder, Laser Material Processing, 4th ed., Springer (2010).

تقييم لحام البقعة بالليزر Nd:YAG لربط المعادن غير المتشابهة من النيكل والنحاس المطلي بالنيكل في قضبان التوصيل لبطاريات الليثيوم-أيون

فيان جبار جمعة[1،2]*، زياد اياد طه[1]، ليفنت جاندان[3] ، إيرسن كاياهان[3]

[1]معهد الليزر للدراسات العليا، جامعة بغداد، بغداد، العراق
[2]قسم الاعمار والمشاريع، جامعة النهرين، بغداد، العراق
[3]مركز بحوث وتطبيقات تقنيات الليزر (LATARUM)، جامعة كوجايلي، 41275، ينيكوي، كوجايلي، تركيا

البريد الالكتروني للباحث: vzangana@nahrainuniv.edu.iq

الخلاصة: تهدف هذه الدراسة إلى تقييم جدوى استخدام لحام البقعة بالليزر النبضي نوع Nd:YAG في ربط المعادن غير المتشابهة المكونة من النيكل والنحاس المطلي بالنيكل ضمن وصلات قضبان التوصيل في بطاريات الليثيوم-أيون. تم فحص تأثير معلمات التشغيل الأساسية المتمثلة بطاقة الليزر، معدل تكرار النبضات، والبعد البؤري على الخواص الميكانيكية والبنيوية للحام. أظهرت النتائج أن طاقة 13 جول حققت أعلى قوة قص بلغت حوالي 273 نيوتن مع منطقة انصهار متجانسة وعيوب سطحية محدودة، في حين سجلت طاقة 10 جول أعلى قيمة للصلادة (370HV0.300) نتيجة توازن إدخال الطاقة مع سرعة التبريد. كما تبين أن معدل التكرار 20 هرتز والبعد البؤري عند 0 ملم يمثلان الشرط الأمثل للحصول على خصائص ميكانيكية ومجهرية مستقرة.

ورغم أن النتائج تؤكد إمكانية الحصول على لحامات عالية الجودة باستخدام هذه التقنية، إلا أن إثبات الموثوقية الكاملة يتطلب استكمال التحليل عبر الفحص بالمجهر الإلكتروني الماسح (SEM)، وتحليل الأطوار (EDS/XRD)، ودراسة أنماط الكسر لتحديد مناطق الفشل. كما توصي الدراسة بإجراء تجارب إضافية لتقييم الأداء طويل الأمد تحت ظروف تشغيل متنوعة كالاهتزاز وتغيرات الحرارة والرطوبة. وبذلك يساهم هذا العمل في توفير أساس علمي يمكن الاعتماد عليه لتطوير عمليات تصنيع أكثر موثوقية في تطبيقات البطاريات الحديثة.

IJL, Issue 2, Vol. 24, 2025
https://doi.org/10.31900/ijl.v24i2.528

Research Article

IRAQI JOURNAL OF LASER

The Clinical Efficiency of 980 nm Diode Laser in Management of Labial Mucocele: Case Report

Mortada Balkit Khudair [1,*], Hanan J. Taher [1], Afrah A Khalil[2]

[1]*Institute of Laser for Graduate Students, University of Baghdad, Baghdad, Iraq*
[2]*College of Dentistry, University of Anbar, Ramadi, Iraq*
** Email address of the Corresponding Author:* mortada.balkit2201m@ilps.uobaghdad.edu.iq

Article history: Received 15 Mar. 2025; Revised 1 Sept. 2025; Accepted 7 Sept. 2025; Published online 15 Dec. 2025

Abstract:

Introduction: A mucocele is a noncancerous abnormality of the mouth that develops when small salivary gland ducts become clogged or when the mouth is traumatized. Due to its many benefits, including less postoperative pain and bleeding and faster recovery, diode laser therapy has grown in popularity. In this particular instance, a 980 nm diode laser was used during a surgical procedure to remove a mucocele from the lower lip.

Case Presentation: The patient was a 23-year-old guy who complained of occasional, painless swelling of the lower lip. Officially, a mucocele was determined. Under local anesthetic, the lesion was removed using a 980 nm diode laser. This procedure allowed for the exact excision of tissue with little damage to adjacent structures. The patient experienced no major side effects or discomfort after the treatment, which indicates that it was well-tolerated. There were no indications of impaired healing during the following appointment.

Conclusion: This case study proves that the 980 nm diode laser is more effective than conventional surgical methods for treating mucoceles. Quick healing, less discomfort, and no incisions are all benefits of the diode laser. It provides a new option for treating oral mucoceles that has shown remarkable improvements in patient outcomes.

Keywords: Mucocele, lower lip, diode laser, 980 nm, oral lesion.

1. Introduction

Many diseases, both benign and cancerous, can impact the mouth. Different triggers, such as poor oral health, tobacco use, ill-fitting dentures, and certain daily habits, can cause reactionary problems and tumors. An accurate diagnosis can only be made with a thorough understanding of the patient's medical history as well as their symptoms and signs, such as the precise location, size, color, and morphology of the oral mucosal lesion [1]. The ducts of tiny salivary glands are the usual targets of mucocele, which is a common oral disease. It arises as a result of the “retention” of mucus or “extravasation” [2].

Trauma or blockage of the ducts of minor salivary glands causes an accumulation of saliva in the adjacent tissue, leading to the appearance of a mucocele. Nodules that are painless, round, soft, smooth, and translucent blue to pink are the clinical manifestations of oral mucoceles [3]. A mucocele happens in about 2.5 out of every 1,000 cases, which is a slightly high rate. They are most common in people in their 20s and 30s, especially kids and teens. They are very rare in kids younger than one year old [4].

In 90% of mucoceles, pseudocysts called mucus extravasation cysts are due to the absence of the epithelial layer. Saliva diffuses into tissues after salivary gland injuries, and an epithelial-lined cyst named a mucus retention cyst occurs 10% of the time when debris or calculi block the salivary duct or when the duct is twisted [5]. Among the several techniques used for treatment are “cryosurgery, sclerotherapy, micro-marsupialization, laser surgery, intralesional injection of corticosteroid or sclerosing agent,” and surgery. Though the most often employed technique is surgery, it has many drawbacks, including lip deterioration and injury to surrounding ducts with additional satellite lesion development [6].
The standard treatment typically involves surgical excision of the adjacent mucosa and glandular tissue down to the muscular layer. Even though the mucocele can be drained by making a small incision, the lesion has a chance for relapse after the wound healing. Treatment is unnecessary if superficial extravasation mucoceles resolve on their own. Small mucoceles can be entirely excised together with the adjacent glandular tissue prior to suturing. The marsupialization technique would protect vital structures from damage in case of big-sized mucoceles [7].

Usually, dental lasers are used in many different areas of dentistry. Patients and doctors both use lasers as standard tools for therapy and care because they are so effective at cutting out maxillofacial tumors while preserving as much of the healthy tissue as possible [8]. Laser therapy is an innovative technique for managing soft tissue lesions, especially diode lasers (with wavelengths between 800 and 980 nm), which are considered an effective alternative to a surgical procedure that can eliminate the lesion and reduce its chance for recurrence. [9]. Nowadays, lasers are incredibly useful for treating soft tissues. Several advantages of laser surgery over traditional scalpels include the ability to sterilize the surgical incision in an instant (bactericidal action), the creation of a hemostatic field (blood-free), effective tissue ablation, and satisfactory visual access. An additional benefit of laser treatment is reduced post- and during-ablation pain for soft tissues [10]. Accordingly, this study was designed to show whether the 980 nm diode laser provides superior clinical efficiency compared with conventional surgery in the management of labial mucocele.

The aim of this study is to evaluate the clinical efficiency of the 980 nm diode laser in the management of labial mucocele and to compare its clinical outcomes with those achieved by conventional surgical excision.

2. Case presentation

A 23-year-old male patient, who was admitted to Basra Teaching Hospital's Oral and Maxillofacial Surgery Department, complained of a soft, painless swelling on his lower lip. According to the patient, the lesion had been becoming bigger over the past several weeks. Lip biting was reported by the patient, which is considered one of the causes for lip mucocele. A dome-shaped, translucent, soft swelling was seen on the inside of the lower lip during the clinical examination. It was blue in color. With no evidence of infection, ulceration, or cancer, the non-tender lesion had a diameter of about 1.5 cm. A mucocele, which can be defined by the lesion's features, is most often produced by trauma that blocks or ruptures the small salivary gland ducts, as shown in Figure 1. We decided to use a 980 nm diode laser (Quicklase diode laser—UK) for laser excision after talking to the patient about their treatment possibilities.

A local anesthetic was used to carry out the operation. The patient was placed in a supine posture while a 0.12% chlorhexidine solution was used to sterilize the operative region. To ensure proper pain control and to decrease intraoperative bleeding, a local anesthetic was delivered using a mixture of 2% “lidocaine” and 1:100,000 “epinephrine.” The incision was performed around the lesion boundary using the Quicklase 980 nm diode laser set at 2 W in continuous mode with the 400-micron fiber tip in contact with the tissue. To reduce the likelihood of a recurrence, the laser enabled exact excision of the mucocele, removing all of the affected small salivary glands. No bleeding occurred during the process, and the whole procedure took around 15 minutes to finish, as shown in Figure 2. Surgical sites were irrigated with sterile saline after excision. No sutures were needed since the diode laser accomplished such remarkable hemostasis; this added to the advantages of a quicker and more comfortable healing process. Avoiding foods that are too hot or spicy, keeping up with satisfactory dental hygiene, and using chlorhexidine mouthwash twice a day to prevent infection were all part of the patient's comprehensive postoperative

recommendations. Furthermore, in order to avoid recurrence, the patient was instructed not to bite her lips.

Figure 1: Lower lip mucocele before excision.

Figure 2: immediately after mucocele excision.

A: one week after operation

B: 20 days after operation C: after one month

Figure 3: A. There was no evidence of infection or problems at the one-week follow-up, and the patient reported little discomfort at the surgery site, which had already begun to epithelialize. Proof of the benefits of laser-assisted surgery was the lack of substantial swelling and discomfort. **B.** Wound healing had progressed further, and there had been no return of swelling during the 20-day follow-up. No functional impairment, trouble speaking, or difficulties eating were reported by the patient. **C.** At the one-month follow-up, the mucosal healing had been fully accomplished. There was no recurrence or residual scarring in the treated area, and the patient was pleased with the results.

3. Discussion

Oral mucoceles arise in different sites on the oral mucosal surfaces overlaying accessory minor salivary glands. They manifest with greater frequency in specific locations. Mucoceles typically manifest on the bottom lip. In rare cases, mucoceles have been found in the "buccal mucosa, lingual frenum, dorsal tongue, retromolar region, upper lip, and palate." Ranula denotes mucoceles placed on the floor of the mouth [11]. Oral mucoceles can manifest at any age. It predominantly occurs in children and young adults (i.e., individuals under 30 years old), with a peak prevalence around the ages of 10 and 29. Individuals of this age are thought to be more susceptible to mechanical trauma, seen as the primary etiological reason underlying the phenomenon of mucus extravasation. Trauma causes the rupture of a salivary gland's excretory duct, leading to the extravasation of saliva into the surrounding connective tissue and the initiation of an inflammatory response [12]. In most cases, mucoceles do not result in substantial complications; however, they can make it difficult to speak, have difficulty chewing, and swallow. Some people may experience discomfort as a result of the mucocele, depending on its size and location [13].

This lesion can be removed using a variety of surgical techniques, such as micro marsupialization, conventional scalpel surgery, CO_2 laser ablation, or marsupialization. Considering potential complications including discomfort, lip deformation, postoperative bleeding, nerve damage, and harm to other anatomical structures, standard scalpel surgery remains the most commonly used method for treating this lesion. [14].

Dental lasers have been increasingly popular since their introduction in the 1990s. In dentistry, they are utilized either as a complementary or independent therapy technique. Using lasers as an alternative to traditional treatment is mostly done with the intention of overcoming the drawbacks that are associated with conventional treatment procedures [15].

Different laser kinds have been produced over time and applied in many branches of dentistry. Among the several types of lasers, the 980 nm diode laser is the most often utilized one. Indium, gallium, and arsenide make a solid-state semiconductor used as the active medium of the diode laser [16].

Diode lasers in oral surgery work in either continuous or pulsing mode, with wavelengths between 810 and 980 nm. By excision or ablation/vaporization, diode laser photothermal activity eliminates oral

mucosa lesions. In photothermal, tissue absorbs radiant light and transforms it to heat energy, therefore changing tissue structure. An appropriate dose of laser energy in contact with the tissue can cause responses ranging from coagulation to vaporization and incision. 980 nm Diode laser wavelengths are absorbed strongly by hemoglobin and melanin chromophores. It thus has selective action and can be used safely in “cutting, blood coagulation, ablation, or vaporizing” soft tissue near the dental structure with minimal injury and better recovery [17]. In this case, the lesion was removed using a diode laser that had a wavelength of 980 ± 10 nm and operated in continuous wave mode. A minimal infiltration of local anesthesia, with a concentration of 1:2,000,000 lidocaine, was administered, and a circumferential incision was made around the swelling, removing it [18].

Dentistry has developed less invasive techniques to lessen patients' pain and discomfort before, during, and after dental procedures. Lasers have thus far proven to be a safe and effective alternative in dental surgery. One of the main benefits of using a high-intensity laser for oral surgery operations is the reduction in the requirement for sutures. Another advantage is the ability to cut while coagulation and hemostasis are being performed. In all instances, this method completely eradicated transoperative bleeding and the necessity for sutures in the research that was part of this evaluation [19].

A diode laser effectively occludes small lymphatic vessels with a penetration depth of 2 mm in the tissue, hence diminishing postoperative edema. Due to the ability of lasers to enhance wound healing by forming a denatured protein coagulum referred to as "eschar" or a "biological bandage," we opted not to utilize sutures or surgical packs in our cases. the protein coagulum protects the wound against germs and friction [20].

Thermal injury to tissues can be caused by lasers. These effects on the target and adjacent tissues can be avoided or eliminated by fine-tuning parameters like power output, optic fiber type, emission patterns, and wavelength. Emission modalities, especially pulsed or continuous wave [CW] emission, must be carefully considered [21, 22]. The laser is well-suited for use with pediatric patients because of its many advantages, such as faster surgery times, better hemostasis, less inflammation, easier access, decontamination of the surgical site, precise incisions, less damage to surrounding tissues, faster healing, less pain, and overall patient satisfaction [23]. Since most laser light falls within the 600–1000 nm range of the red and near-infrared portions of the electromagnetic spectrum, the "Quicklase" 810–980 nm diode laser device was employed for this study [24]. Photo-thermal interaction between fibers allows a diode laser to deliver energy to soft tissues. To accelerate tissue incisions, the fiber optic tip needs to be activated so that the laser energy can be concentrated at the tip of the fiber optic and converted into thermal energy [25]. In this instance, we see how a 980 nm diode laser a minimally invasive method with better clinical results to remove mucoceles. Confirming the benefits of 980 nm diode laser technology in oral soft tissue procedures, the technique provided a speedy recovery, no bleeding during the operation, minimum postoperative discomfort only during the first two days, and great wound closure without suturing material.

4. Conclusion

A lower lip mucocele was removed less invasively and effectively with the 980 nm diode laser. The operation's key benefits were a bloodless surgical region, less postoperative pain, no suture, and a quick recovery. Follow-up showed no recurrence. According to these data, the 980 nm diode laser with 2W power may be an effective alternative to invasive surgery for mucocele lesion removal.

References

[1] Odah, Z. F., Taher, H. J., and AlAlawi, A. S. Evaluation of the efficacy of Er, Cr: YSGG laser in treating oral benign soft tissue lesions. Journal of Dental Research, Dental Clinics, Dental Prospects, 18(4), 291(2024).

[2] Besbes, A., Elelmi, Y., Khanfir, F., Belgacem, R., and Ghedira, H. Recurrent oral mucocele management with diode laser. Case reports in dentistry, 2020(1), 8855759(2020).

[3] Choi, Y. J., Byun, J. S., Choi, J. K., and Jung, J. K. Identification of predictive variables for the recurrence of oral mucocele. Medicina oral, patologia oral y cirugia bucal, 24(2), e231(2019).

[4] Mukundan, D., and R, R. pediatric oral mucocele management: a case series investigating different treatment approaches. Cureus, 16(6), e63342 (2024).
[5] Nagar, S. R., Fernandes, G., Sinha, A., and Rajpari, K. N. Mucocele of the tongue: A case report and review of literature. Journal of Oral and Maxillofacial Pathology, 25(l 1), S37-S41(2021).
[6] Gaikwad, T. V., Maini, A. P., Das, S., Lokhande, S., Patil, S. K., and Sarma, A. Nonsurgical management of oral mucocele occurring on a rare site. Contemporary Clinical Dentistry, 13(4), 389-391(2022).
[7] Ata-Ali, J., Carrillo, C., Bonet, C., Balaguer, J., Penarrocha, M., and Peñarrocha, M. Oral mucocele: review of the literature. J Clin Exp Dent, 2(1), e18-21(2010).
[8] Odah, Z. F., Taher, H. J., and AlAlawi, A. Effectiveness of the Er, Cr: YSGG Laser in the removal of oral plexiform neurofibroma (case report). Iraqi Journal of Laser, 23(2), 69-75(2024).
[9] Arafat, S., Mohsen, M., El-Tagy, G., and Saafan, A. Diode Laser 980 nm treatment of recurrent mucocele in the ventral surface of tongue in a 6 years old girl: A case report, IOSR Journal of Dental and Medical Sciences (IOSR-JDMS) e-ISSN: 2279-0853, p-ISSN: 2279-0861.Volume 20, Issue 11 Ser.5 (November. 2021), PP 43-46 .
[10] Al-Ani, A. J., Al-Alawi, A. S., and Taher, H. J. Analysis of the temperature elevation of the dual-wavelength diode laser and the Er, Cr: YSGG laser in oral soft tissue incisions. Journal of Lasers in Medical Sciences, 14 (2023).
[11] More, C. B., Bhavsar, K., Varma, S., and Tailor, M. Oral mucocele: A clinical and histopathological study. Journal of oral and maxillofacial pathology: JOMFP, 18(1), S72–S77(2014).
[12] Miranda, G. G. B., Chaves-Junior, S. C., Lopes, M. P., Rocha, T. B. D., Colares, D. F., Ito, F. A., Cavalcante, I. L., Cavalcante, R. B., Andrade, B. A. B., Nonaka, C. F. W., Alves, P. M., Albuquerque-Júnior, R. L. C., and Cunha, J. L. S. Oral mucoceles: A Brazillian Multicenter Study of 1,901 Cases. Brazilian dental journal, 33(5), 81–90(2022).
[13] Bansal, S., Verma, D. K., Goyal, S., and Rai, M. comparison of micromarsupialization and modified micromarsupialization for the management of mucocoele of lower lip: a prospective randomized clinical trial. Journal of maxillofacial and oral surgery, 16(4), 491–496(2017).
[14] Hashemi, M., Zohdi, M., Zakeri, E., Abdollahzadeh-Baghaei, T., and Katebi, K. Comparison of the recurrence rate of different surgical techniques for oral mucocele: A systematic review and Meta-Analysis. Medicina oral, patologia oral y cirugia bucal, 28(6), e614–e621(2023).
[15] Sadiq, M. S. K., Maqsood, A., Akhter, F., Alam, M. K., Abbasi, M. S., Minallah, S., Vohra, F., Alswairki, H. J., Abutayyem, H., Mussallam, S., and Ahmed, N. The effectiveness of lasers in treatment of oral mucocele in pediatric patients: A Systematic Review. Materials (Basel, Switzerland), 15(7), 2452(2022).
[16] Morsy, D. A., Negm, M., Diab, A., and Ahmed, G. Postoperative pain and antibacterial effect of 980 nm diode laser versus conventional endodontic treatment in necrotic teeth with chronic periapical lesions: A randomized control trial. F1000Research, 7, 1795(2018).
[17] Marhab, E. I., and Mahdi, Z. F. A comparison between diode laser 976 nm and conventional technique in treatment of gingival fibromatosis. Iraqi Journal of Laser, 23(1), 71-79 (2024).
[18] Gogoi, A., Pawar, M., Badarkhe, A., Vhatkar, B., Bagde, H., and Kharat, S. Diode Laser Approach for Excision of Solitary Mucocele. Journal of pharmacy and bioallied sciences, 14(l 1), S1066–S1069(2022).
[19] Protásio, A. C. R., Galvão, E. L., and Falci, S. G. M. Laser Techniques or Scalpel Incision for Labial Frenectomy: A Meta-analysis. Journal of maxillofacial and oral surgery, 18(4), 490–499 (2019).
[20] Ahad, A., Tandon, S., Lamba, A. K., Faraz, F., Anand, P., and Aleem, A. Diode laser assisted excision and low level laser therapy in the management of mucus extravasation cysts: a case series. *Journal of lasers in medical sciences*, *8*(3), 155(2017).
[21] Cercadillo-Ibarguren I, España-Tost A, Arnabat-Domínguez J, Valmaseda-Castellón E, Berini-Aytés L, Gay-Escoda C. Histologic evaluation of thermal damage produced on soft tissues by CO 2, Er,Cr:YSGG and diode lasers. Med Oral Patol Oral Cir Bucal. 6 (2010).
[22] Amaral FR, Ferreira MVL, Costa LAP, de Oliveira PAD, Soares BM, Souza PEA, et al. Use of surgical laser for excision of a neurofibroma associated with neurofibromatosis type-1. J Lasers Med Sci. 9(3), 219–22 (2018).
[23] Fioravanti, M., Zara, F., Vozza, I., Polimeni, A., and Sfasciotti, G. L. The Efficacy of Lingual Laser Frenectomy in Pediatric OSAS: A Randomized Double-Blinded and Controlled Clinical Study. International journal of environmental research and public health, 18(11), 6112 (2021).
[24] Haidar Flayyih Hasan, Layla M. H. Al-ameri, and Ammar Saleh Alalawi. Impact of low level laser therapy on mandibular range motion in temporomandibular joint disorder in iraqi patients. Iraqi Journal of Laser, 23(2), 107-114(2024).
[25] Bagher, S. M., Sulimany, A. M., Kaplan, M., and Loo, C. Y. Treating Mucocele in Pediatric Patients Using a Diode Laser: Three Case Reports. Dentistry journal, 6(2), 13(2018).

الكفاءة السريرية للدايود ليزر 980 نانومتر في معالجة الكيس المخاطي الشفوي: تقرير حالة

مرتضى بلكت خضير [1]، حنان جعفر طاهر [1] ، افراح عدنان خليل [2]

[1] معهد الليزر للدراسات العليا، جامعة بغداد، بغداد، العراق
[2] كلية طب الاسنان، جامعة الانبار، الرمادي، العراق

البريد الالكتروني للباحث: *Mortada.balkit2201m@ilps.uobaghdad.edu.iq*

الخلاصة : الكيس المخاطي هو آفة فموية حميدة غالبًا ما تتطور بعد التعرض للصدمة أو عندما تصبح الغدد اللعابية الصغيرة مسدودة. أصبح العلاج بواسطة الليزر مؤخرًا أكثر شيوعًا بسبب فوائده العديدة، مثل تقليل الألم والنزيف بعد العملية، والتعافي الأسرع. مثال على استخدام دايود ليزر 980 نانومتر لمعالجة كيس مخاطي في الشفاه السفلية في هذه الحالة. **عرض الحالة** : مريض يبلغ من العمر 23 عامًا يعاني من تورم متناوب الظهور والاختفاء غير مؤلم في الشفاه السفلية. كان التشخيص هو الكيس المخاطي. تحت تأثير التخدير الموضعي للمريض، تم استخدام الدايود ليزر 980 نانومتر لإزالة الآفة. ساعد ذلك بإزالة الأنسجة بدقة مع التسبب في الحد الأدنى من الضرر للأنسجة المحيطة. بعد الإجراء، أفاد المريض بعدم وجود أي إزعاج أو مشاكل كبيرة، وبالتالي كان التحمل واضحًا. في موعد المتابعة، لم تكن هناك أي علامات على أن عملية الشفاء قد تأثرت. **الاستنتاج** : يوضح هذا المثال كيف يعالج الدايود ليزر 980 نانومتر الاكياس المخاطية بشكل جيد، مما يثبت فوائده مقارنة بالتقنيات الجراحية التقليدية. يوفر الدايود ليزر تعافيًا أسرع وراحة أفضل للمريض بالإضافة إلى كونه تقنية غير ضارة. و يوفر حلاً بديلاً جيدًا لعلاج الاكياس المخاطية الفموية مع نتائج سريرية ممتازة.

IJL, Issue 2, Vol. 24, 2025
https://doi.org/10.31900/ijl.v24i2.541

Research Article

IRAQI JOURNAL OF LASER

Laser-Ablated Silver Nanoparticles Embedded in P3HT: A Study of Structural and Optical Enhancement

Zainab Jabar Abd Al-Kareem*, Estabraq Talib Abdullah

Department of Physics, College of Science, University of Baghdad, Iraq.
**Email address of the Corresponding author*: zainab.jabbar1804a@sc.uobaghdad.edu.iq

Article history: Received 11 Jun. 2025; Revised 1sept. 2025; Accepted 7 Sept. 2025; Published online 15 Dec. 2025

Abstract: The hole transport layers are critical components of organic conductor-based devices. The metal nanoparticles (NPs) are excellent materials for this purpose. This paper describes the preparation of silver nanoparticles (Ag NPs) using a laser method, which were then mixed with the organic polymer poly(3-hexylthiophene) (P3HT) at different concentrations (0.1, 0.3, and 0.4 wt%). The structural morphology, structure, and optical properties of the new nanocomposite were examined using X-ray diffraction (XRD), field emission scanning electron microscopy (FESEM), atomic force microscopy (AFM), and UV-Vis spectroscopy. The XRD data showed that the created Ag NPs have a crystal structure, with the strongest peaks seen at angles of 38.1°, 44.3°, 64.4°, and 77.4°. The FESEM and AFM tests showed that having more Ag NPs makes the surface rougher and helps spread the nanoparticles better, where the surface roughness increased from 2.04 to 2.46 nm, the mean roughness of the film (Ra) changed from 1.55 to 1.81 nm, and the maximum height of the film (Rmax) ranged from 22.34 to 25.38 nm. The UV-Vis spectroscopy results showed that the material absorbed lighter due to the localized surface plasmon resonance (LSPR) effect, which caused the absorption peaks to move to shorter wavelengths and lowered the optical energy gap from 2.1 eV for pure P3HT to 2 eV with a 0.3 wt% concentration of AgNPs. P3HT nanocomposites with Ag nanoparticles have better structure and optical properties, which make them ideal for organic solar cells and other electronic applications.

Keywords: Poly(3-hexylthiophene), AgNPs, laser ablation, LSPR, nanocomposites, optical properties.

1. Introduction

Organic semiconductors are the most significant category among optoelectronic devices because of their cost-effectiveness, flexibility, and lightweight characteristics [1,2]. The poly (3-hexylthiophene) (P3HT) is the most studied type of conjugated polymer because it can carry electric charge well, stable in different conditions, and can be processed in solution. There are many various applications of these organic polymers, including organic light-emitting diodes (OLEDs), organic solar cells (OSCs), and organic field-effect transistors (OFETs), which have seen extensive utilization [3-5]. P3HT has many advantages, but it is limited because it doesn't absorb much visible light and has average charge carrier mobility [6,7]. To solve these problems, many studies have looked at creating conjugated polymers that include metal nanoparticles (NPs) in the electronic polymer [8]. Metallic Nanoparticles (NPs), especially silver nanoparticles (AgNPs) are of great interest because they have a special effect called localized surface plasmon resonance (LSPR), which improves light absorption and helps move electric charges more easily [9]. The incorporation of AgNPs into P3HT substantially improve the structural, morphological, electrical, and optical properties of the polymer matrix, thereby enhancing device performance. Mustafa and Abdullah (2019) demonstrated that the incorporation of metal nanoparticles into P3HT enhances light absorption and facilitates improved

charge mobility. They studied the effect of P3HT with Al, Ag, and Cu as metallic nanoparticle hybrids. They used laser ablation in liquid (LAL) to synthesize the nanoparticles, and the morphological and structural analysis proved the interaction between P3HT and these nanoparticles [10].

Gan et al. (2025) they demonstrated that employing P3HT in conjunction with silver nanostructures, which increase light, significantly amplified both Raman and fluorescence signals. This phenomenon occurs when light energizes charges in P3HT, which subsequently move to the silver, enhancing the electromagnetic field and amplifying the intensity of both Raman and fluorescence signals [11]. Many of these studies depend on chemical synthesis methods for AgNPs because of their low cost and high efficiency, but these methods suffer from potentially introducing impurities and impacting reproducibility. Despite chemical approaches, laser ablation in liquid (LAL) generates Ag NPs of higher purity, where no capping or stabilizing compounds are required, rendering it an environmentally sustainable method since it gives precise control over NP size and distribution. Due to these features, this method has garnered significant attention for synthesizing nanomaterials [13-15].

Even though LAL-synthesized Ag NPs have many advantages, they haven't been studied much for use in P3HT-based nanomaterials, particularly in chloroform. Consequently, we select the LAL approach, which involves performing laser ablation directly in chloroform (the solvent for dissolving P3HT), resulting in the rapid and uniform dispersion of AgNPs, thereby decreasing agglomeration and enhancing homogeneous incorporation with the polymer. This study aims to employ laser ablation to synthesize Ag NPs for various concentrations (0.1, 0.3, and 0.4 wt%) on the structural, morphological, and optical properties of P3HT's. The motivation of the work, depending on the LAL features, is to utilizing the localized surface plasmon resonance (LSPR) effect of Ag NPs to enhanced light absorption and charge transport in P3HT. By using LAL to make Ag NPs directly in chloroform, we want to improve how well the nanoparticles mix with the polymer and boost the performance of P3HT-based optoelectronic materials.

2. Experimental Parts

2.1. Materials

P3HT, which has a molecular weight of 28000, was used along with schematic 1, and glasses covered with indium tin oxide (ITO) that have a sheet resistance of 12 Ω/sq, supplied by OSSILA Chemical Co. Silver plates with a thickness of 1 mm and a purity of 98.2% were supplied from the local market. Chloroform ($CHCl_3$) with high purity was used as a solvent, which was also provided by OSSILA Chemical Co.

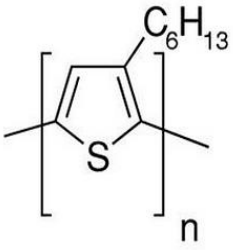

Schematic 1: Poly (3-hexylthiophene) (P3HT).

2.2. Characteristics Technique

Field-effect scanning electron microscopic (FESEM) data were recorded using a Model (Inspect S50). The samples were characterized using AFM to study the topography (Nanosurf Easyscan 2, Switzerland). The X-ray diffraction (XRD) pattern of the prepared AgNPs sample, which was dried in the hot air oven, was recorded at a Model DX-2700BH using CuKα radiation with wavelength = 1.5406 Å. The UV–vis spectroscopy (U-2800, Hitachi double beam, Japan) was used to analyze the prepared samples. The lambda max was measured within the range between 200 and 1100 nm.

2.3. Synthesis of P3HT/Ag NPs Nanocomposites

To dissolve P3HT (20mg), it was added to 1 mL of chloroform, stirred with a magnetic stirrer for 1 h at 60°C, and then put in an ultrasonicator bath for 30 minutes for good polymer stability. First, the silver plate was cleaned with ethanol to remove any contamination. It was added to the peaker (50 ml) containing 20 ml of chloroform, which was used to achieve the affinity with the polymer. To prepare the AgNPs, Q-switched Nd:YAG operating at 1064 nm, and 6 Hz frequency with a energy of 1000 mJ per pulse and a positive lens with a focal lengthof 110mm, which was employed as an ablation source. for 200 shoots was used, Figure.1 shows the laser ablation device. The effective spot size of the laser beam on the metal plate's surface was adjusted between 2.37 mm and 0.4 mm in diameter to enhance the laser fluence. The liquid thickness was adjusted from 2 mm to 14 mm to enhance the shock wave. The liquid thickness is modified by employing various cell dimensions. The quantity of laser blasts administered to the metal target varied from 10 to 80 pulses.

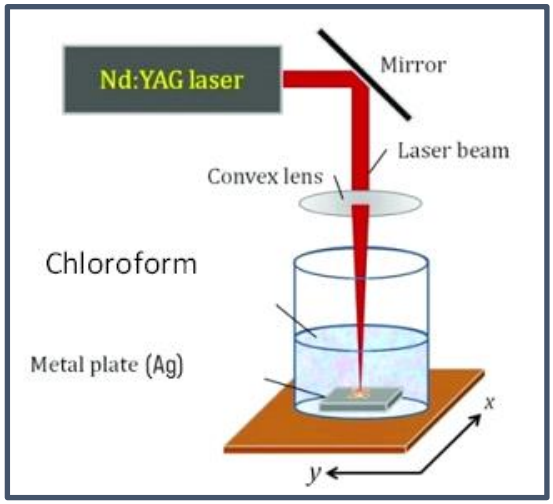

Figure 1: The experimental setup of the preparation of AgNPs by laser device [16].

Fig. 2. The AgNPs that were created were added to a P3HT solution in different amounts (0.1, 0.3, and 0.4 wt%) and mixed for 2 hours at 60°C. They were then placed in an ultrasonic bath for 1 hour. After that, they were applied to ITO substrates using spin coating and heated at 120°C for 10 minutes.

Figure 2*:* The prepared samples of a) pure P3HT, b) 0.1, c)0.3, and d) 0.4 wt% Ag NPs**.**

3. Results and Discussion

The XRD pattern, Fig. 3, shows the crystalline nature of the prepared AgNPs using the laser ablation technique. The important peaks at 2θ values (38.1°, 44.3°, 64.4°, and 77.4°) match the (111), (200), (220), and (311) planes in a face-centred cubic (fcc) silver crystal, according to JCPDS Card No. 04-0783. These results agree with the literature [4,5]. At the same time, the other 2θ values (22.9°, 26.5°, 30.5°, 47°, and 54.3°) may be due to the silver oxide phases (e.g., Ag_2O or AgO) according to the JCPDS No. 41-1104. By using Scherrer equation from the XRD pattern, the mean particle diameter for the Ag NPs can be calculated as follows:

$$D = \frac{k\lambda}{\beta \sin\theta} \quad (1)$$

where λ is the X-ray wavelength, k is the shape constant, βrepresents the full width of the diffraction band (FWHM) for Bragg angle, and θ is the Bragg diffraction angle, respectively. The average crystallite size for Ag NPs was found to be 8 nm. These results satisfy with Rahmah et al. [17] and Kaçuş et al. [18].

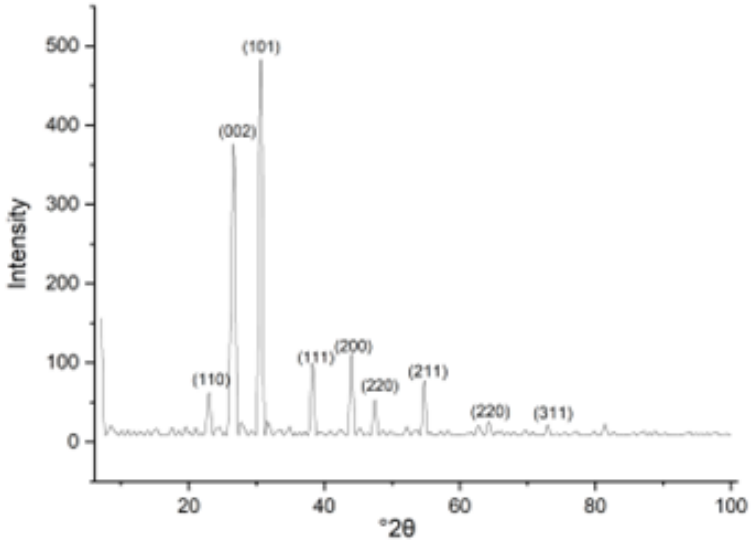

Figure 3: XRD of Ag NPs sample.

To study the morphological structure, only two concentrations of Ag NPs were chosen (0.1 and 0.4 wt%), as shown in Fig. 4a and b. The images show a high tendency for NP agglomeration, especially for higher concentrations. This behavior may be due to the high surface energy of Ag NPs, which makes them aggregate to minimize energy. Also, the preparation method (LAL) doesn't need any surfactants or stabilizers that assist in reducing the aggregation. The uniform size distribution in the P3HT matrix is less broad and broader due to the NPs' agglomeration tendency. This distribution indicates that metallic nanoparticles have a hard time spreading out in the polymer matrix and easily group together into clusters. At 0.1 wt%, the particles tend to clump together, leading to a smaller and less even size range of P3HT, with an average size of about 35 nm. When the concentration of Ag NPs is increased to 0.4 wt%, the silver nanoparticles become more noticeable and spread out better in the polymer matrix, leading to average sizes of about 95 nm. The particle scale distribution illustrates this behaviour in Figure 4. The literature [19,20] reports similar FESEM images of P3HT: Ag NPs. This image shows bright spots on the surface of Ag NPs because of their high atomic number, while the other area appears smooth and darker, indicating the presence of organic P3HT [21].

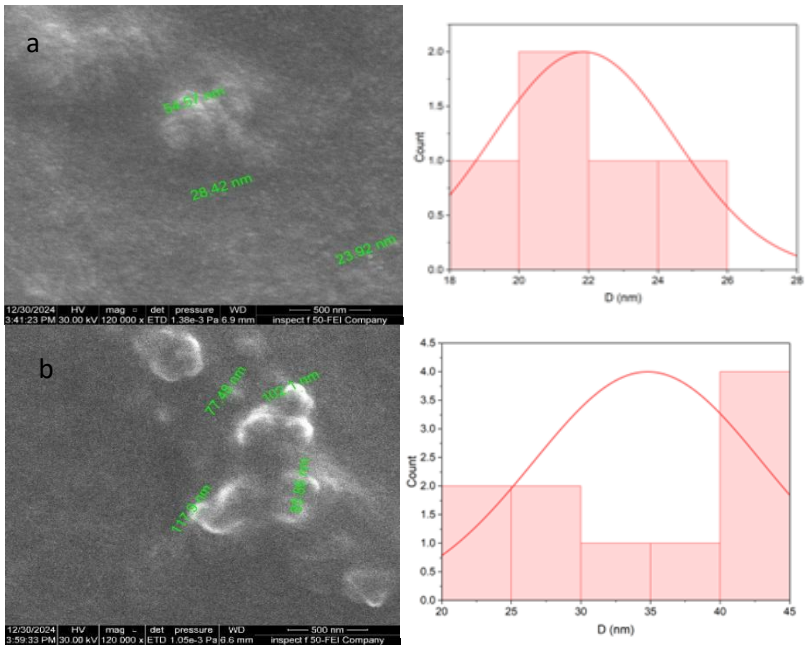

Figure 4: FESEM images and histogram of the particle size distribution of nanoparticles of P3HT (a) with 0.1, and (b) 0.4 wt % Ag NPs.

We appreciate the reviewer for his recommendation. In addition, we extended the discussion to the effects of surface morphology on optical properties, and Figure 5a-b presents 3D AFM plots. The 3D AFM images clearly evidenced that the two parts of the nanostructured P3HT/AgNPs films (Figs. 5a,b), indicating that the plainness of surface for 0. % is fair, and the grain is somewhat spread on the composite surface. With the higher concentration of Ag NPs, the surface roughness is increasing that can result higher probability of agglomeration in the polymer matrix [22,23]. The obtained data indicated that the size of the surface asperities of the film increased from 2.04 to 2.46 nm (Ra) and 1.55-1.81 nm and 22.34-25.38 nm (Ra and Rmax, respectively) of the film, respectively. The enhanced surface roughness may cause enhanced light scattering and absorption which are favourable for the higher generation of excitons.

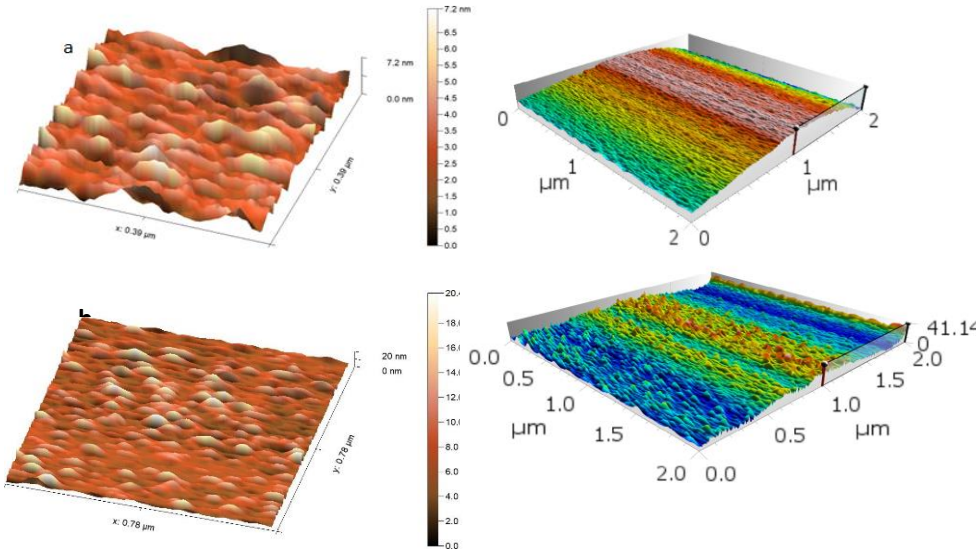

Figure 5: AFM images of P3HT (a) 0.1 wt% AgNPs, and (b) 0.4 wt% AgNPs.

The incorporation of plasmonic NPs into P3HT is an emerging approach to enhancing the optical absorption of polymer matrix. The optical properties of both pure P3HT and nanocomposites of P3HT and AgNPs were examined by the use of UV-Vis spectroscopy. Fig. 6 displays the samples' ultraviolet-visible absorption spectra; as part of the nanoparticle analysis, this included evaluating their absorbance spectra across the wavelength range of 290-600 nm.

Figure 6 indicates the intensity increases with increasing Ag NPs concentration in the nanocomposites, showing that the light absorption improves because of the effects of localized surface plasmon resonance (LSPR). The LSPR of the Ag NPs may couple with the absorption coefficient peak of the P3HT matrix in this case. The increase in the absorption coefficient may be attributed to enhanced light trapping resulting from the incorporation of metallic nanoparticles. The observed increment may also be attributed to the local electrical field enhancement generated by the plasmonic nanoparticles within the polymer matrix [24]. The UV-visible spectrum of the P3HT film showed two peaks at 404 nm and 452 nm, caused by the movement of electrons in the organized structure of the P3HT polymer chains. All exhibited spectra showed a sharp peak near 270–280 nm. This spike might be due to changes in the electrons of the aromatic system or a special effect from AgNPs, which becomes more obvious when there is more Ag. As the concentration of AgNPs increases, the absorption peaks shift to shorter wavelengths, indicating that the electronic structure of P3HT changes because of its interaction or clumping together [25].

Using Beer-Lambert's law: ($\alpha = 2.303A/d$), where A is the absorbance, the absorption coefficient, α, was calculated. Fig. 6 shows the absorption coefficient spectra of the P3HT and P3HT/AgNPs nanocomposites. All samples showed a low absorption in the visible and NIR regions. In the UV range, high absorbance was detected, which is due to the melanin's wide band gap properties [11,12]. In organic semiconductors, the band-gap energy Eg relates to two electron movements: from HOMO (highest occupied molecular orbital) to LUMO (lowest unoccupied molecular orbital), which happen between the molecular orbitals π and π^*. Tauc's method, which uses the formula $\alpha h\upsilon = A(h\upsilon - Eg)1/2$ (where $h\upsilon$ is the energy of the incoming photon), was applied to find the direct band-gap energy by extending the straight line to the photon energy axis. We determined the energy gap of P3HT to be approximately 2.3 eV, which aligns with the literature [13]. The energy gap tends to increase after adding AgNPs to P3HT to form nanocomposites, as shown in Table 1. Crystal regularity also influences these values. The energy gap can be determined using the classical relation for near-edge optical absorption in semiconductors [27]. A slight band gap blue shift (2.35 → 2.38 eV) and the increased absorption intensity imply that the semiconducting nature of P3HT is preserved, as Ag NPs interact plasmonically and alter morphological features of P3HT. this band gap shift may due to enhanced carrier localization, confinement effect, degradation of conjugation length, and Exciton splitting due to the Strong interaction of P3HT with AgNPs.

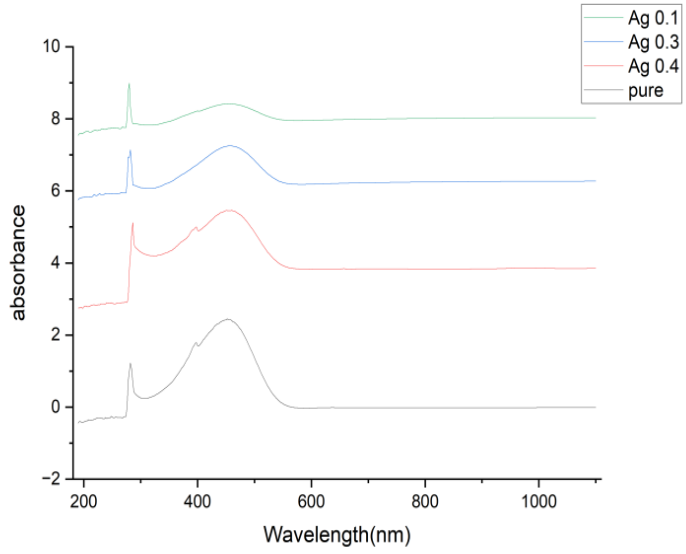

Figure 6: Absorbance spectra for P3HT/Ag NPs nanocomposites.

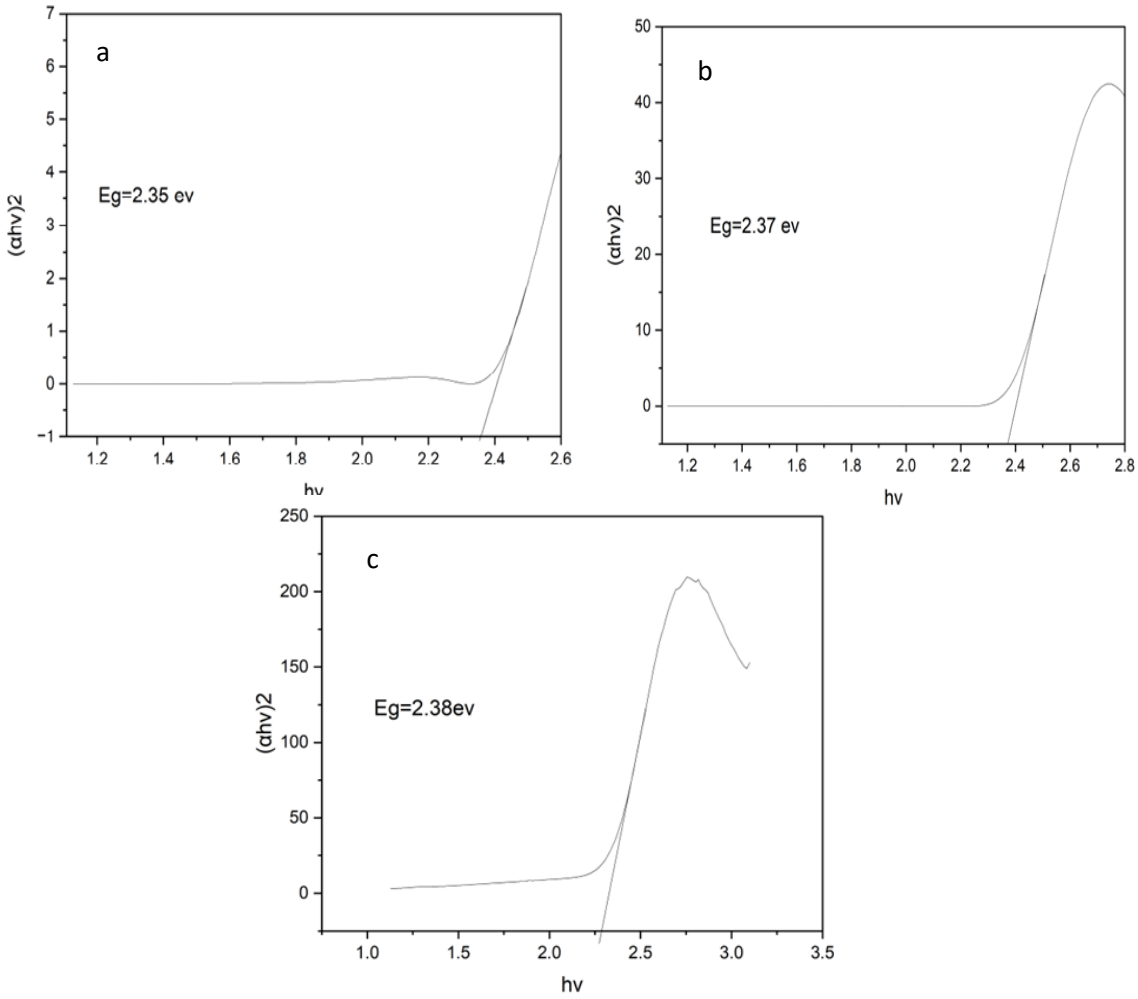

Figure 7: Tauc plot for of P3HT (a) 0.1, (b) 0.3, and (c) 0.4 wt% AgNPs.

Table. 1: The Energy gap values for P3HT/ Ag NPs nanocomposite

Sample	Eg (eV)
Pure P3HT	2.1
0.1	2.35
0.3	2.37
0.4	2.38

4. Conclusions

The preparation of P3HT/Ag nanocomposites exhibits special features in which the silver nanoparticles are made by laser ablation. The surfactant-free Ag NPs, prepared by liquid laser ablation (LAL), with relatively high purity, which minimized any undesired chemical interactions. Structure analysis indicated the existence of Ag NPs crystallites (~9 nm) in a face-centered cubic (fcc) shape. Meanwhile, FESEM results demonstrated the occurrence of regulated agglomerates due to the particle density and polymer attraction. Optical analysis indicated that Ag NPs were able to modulate the intensity of P3HT absorption and emission

spectra, indicating a possible plasmonic effect and excitonic interactions, for example, at the optimized concentrations. These results indicate that the nanocomposite structure and optical properties can be controlled for applications in optoelectronic devices, such as organic solar cells or photodetectors.

References

[1] Q. Zhang, W. Hu, H. Sirringhaus, and K. Müllen, "Recent progress in emerging organic semiconductors", Adv. Mater., 34, 2108701 (2022). DOI: 10.1002/adma.202108701
[2] K. N. Subedi, A. Al-Shadeedi, and B. Lüssem, "Stability of organic permeable base transistors", Appl. Phys. Lett., 115, 193301 (2019). DOI: 10.1063/1.5125233
[3] H. A. Abbas, W. C. Koubaa, and E. T. Abdullah, "Synthesis, characterization and functionalization of P3HT-CNT nanocomposite thin films with doped Ag_2O", East Eur. J. Phys., (1), 342–354 (2024).DOI: 10.26565/2312-4334-2024-1-32.
[4] Q. Fu, P. Yang, X. Huang, et al., "Rational molecular and device design enables organic solar cells approaching 20% efficiency. DOI: 10.1038/s41467-024-46022-3
[5] B. H. Mohammed and E. T. Abdullah, "Comparison between horizontal and vertical OFETs by using poly(3-hexylthiophene) (P3HT) as an active semiconductor layer", Iraqi J. Sci., 61, 1040–1050 (2020). DOI: 10.24996/ijs.2020.61.5.13
[6] F. Laquai, D. Andrienko, R. Mauer, and P. W. M. Blom, "Charge carrier transport and photogeneration in P3HT:PCBM photovoltaic blends", Macromol. Rapid Commun., 36(11), 1001–1025 (2015). DOI: 10.1002/marc.201500047
[7] L.Rodrigues Koenig, et al., "Effects on the emission of different interfaces formed between poly(3-methylthiophene) and poly(3-octylthiophene): Electrochemical impedance and photoluminescence spectroscopy studies", Heliyon, 8, e09515 (2022). DOI: 10.1016/j.heliyon.2022.e09515
[8] S. Kang, T. W. Yoon, G.-Y. Kim, and B. Kang, "Review of conjugated polymer nanoparticles: from formulation to applications", ACS Appl. Nano Mater., 5, (2022). DOI: 10.1021/acsanm.2c04730
[9] M. Mcoyi, K. Mpofu, M. Sekhwama, and P. Mthunzi-Kufa, "Developments in localized surface plasmon resonance", Plasmonics, (2024). DOI: 10.1007/s11468-024-02620-x
[10] M. A. Mustafa and E. T. Abdullah", Iraqi J. Phys., 17, 122–127 (2019). DOI: 10.30723/ijp.v17i43.490
[11] R. Gan, D. Duleba, R. P. Johnson, and J. H. Rice, "p-Type organic semiconductor–metal nanoparticle hybrid film for the enhancement of Raman and fluorescence detection", J. Phys. Chem. C, 129, 3659–3666 (2025). DOI: 10.1021/acs.jpcc.4c08030
[12] A. Kasus-Jacobi, J. L. Washburn, C. A. Land, and H. A. Pereira, "The photosensitive activity of organic/inorganic hybrid devices based on Aniline Blue dye: Au nanoparticles (AB@Au NPs)", Sensors and Actuators A: Physical, 330, 112856 (2021). DOI: 10.1016/j.sna.2021.112856
[13] R. Abbas, J. Luo, X. Qi, A. Naz, I. A. Khan, H. Liu, S. Yu, and J. Wei, "Silver nanoparticles: synthesis, structure, properties and applications", Nanomaterials, 14, 1425 (2024). DOI: 10.3390/nano14171425
[14] D. Zhang, Z. Li, and K. Sugioka, "Femtosecond laser fabrication in transparent materials", J. Phys. Photonics, 3, (2021).
[15] I. Y. Khairani, G. Mínguez-Vega, C. Doñate-Buendía, and B. Gökce, "Ultrafast laser synthesis of nanoparticles in liquids: Mechanisms and strategies", Phys. Chem. Chem. Phys., 25, 19380–19408 (2023).
[16] F. Abd alahadi, N. S. Shnan, and S. F. Haddawi, "Enhancement surface plasmon resonance in the visible region by different active media", Journal of Nanostructures, 14(1), 184–194 (2024). DOI: 10.22052/JNS.2024.01.019
[17] M. I. Rahmah, A. M. Ahmed, T. M. Al-Rashid, and A. J. Qasim, "Preparation of silver nanoparticles using laser ablation for in vitro treatment of MCF-7 cancer cells with antibacterial activity", Plasmonics, 19(4), 2097–2105, 19(4), (2024). DOI: 10.1007/s11468-023-02150-y
[18] H. Kaçuş, M. Biber, and Ş. Aydoğan, "Role of Au and Ag nanoparticles on organic solar cell based on P3HT:PCBM active layer", Appl. Phys. A, 126, 817 (2020). DOI: 10.1007/s00339-020-03992-7
[19] P. Muenraya, S. Sawatdee, T. Srichana, and A. Atipairin, "Silver nanoparticles conjugated with colistin enhanced the antimicrobial activity against Gram-negative bacteria", Molecules, 27, 5780 (2022). DOI: 10.3390/molecules27185780
[20] H. Kaçuş, Ö. Metin, M. Sevim, M. Biber, A. Baltakesmez, and Ş. Aydoğan, "A comparative study on the effect of monodisperse Au and Ag nanoparticles on the performance of organic photovoltaic devices", Opt. Mater., 116, 111082 (2021).
[21] I. M. Ibrahim, "Synthesis and characteristics of Ag, Cu/Au core/shell nanoparticles produced by pulse laser ablation", Iraqi Journal of Science, 58(3C), 1651-1659 (2021).

[22] R. Gan, D. Duleba, R. P. Johnson, and J. H. Rice, "p-Type organic semiconductor–metal nanoparticle hybrid film for the enhancement of Raman and fluorescence detection", J. Phys. Chem. C, 129, 3659–3666 (2025). DOI: 10.1021/acs.jpcc.4c08030.
[23] Y. Zhao, K. Zheng, J. Ning, T. Xu, and S. Wang, "Plasmonics in organic solar cells: toward versatile applications", ACS Appl. Electron. Mater., 5, 632–641 (2023). DOI: 10.1021/acsaelm.2c01607
[24] A. A. Hussein, A. A. Sultan, M. T. Obeid, A. T. Abdulnabi, and M. T. Ali, "Synthesis and characterization of poly(3-hexylthiophene)", Int. J. Sci. Eng. Appl. Sci., 1, (2015).
[25] J. Zhang, Y. Huang, Y. Dan, and L. Jiang, "P3HT/Ag/TiO_2 ternary photocatalyst with significantly enhanced activity under both visible light and ultraviolet irradiation", Appl. Surf. Sci., 488, 228–236 (2019). DOI: 10.1016/j.apsusc.2019.05.150
[26] B. Hajduk, P. Jarka, H. Bednarski, et al., "Thermal and optical properties of P3HT:PC70BM:ZnO nanoparticles composite films", Sci. Rep., 14, 66 (2024). DOI: 10.1038/s41598-023-47134-4
[27] E. K. Salman and G. S. Muhammed, "Study of some structural and optical properties for synthesized graphene/polyaniline/ZnS nanocomposite", Iraqi J. Phys., 22(4), 53–66 (2024). DOI: 10.30723/ijp.v22i4.1244

جسيمات نانوية فضية مُزالة بالليزر ومُضمنة في P3HT: دراسة للتحسين الهيكلي والبصري

زينب عبد الكريم* ،استبرق طالب عبدالله

قسم الفيزياء، كلية العلوم، جامعة بغداد، بغداد، العراق

البريد الالكتروني للباحث:zainab.jabbar1804a@sc.uobaghdad.edu.iq

الخلاصة :تعتبر طبقات نقل الثقوب هي مكونات أساسية للأجهزة القائمة على الموصلات العضوية. تُعد الجسيمات النانوية المعدنية (NPs) مواد ممتازة لهذا الغرض. تصف هذه الورقة البحثية تحضير جسيمات نانوية فضية (Ag NPs) باستخدام طريقة الليزر، والتي خُلطت بعد ذلك مع البوليمر العضوي بولي (3-هكسيل ثيوفين) (P3HT) بتركيزات مختلفة (0.1، 0.3، و0.4٪ وزنًا). دُرست البنية والبنية والخصائص البصرية للمركب النانوي الجديد باستخدام حيود الأشعة السينية (XRD)، ومجهر مسح إلكتروني بانبعاث المجال (FESEM)، ومجهر القوة الذرية (AFM)، ومطيافية الأشعة فوق البنفسجية-المرئية. أظهرت بيانات حيود الأشعة السينية أن جسيمات النانو الفضية المُنتجة لها بنية بلورية، حيث تُرى أقوى القمم عند زوايا 38.1 درجة، 44.3 درجة، 64.4 درجة، و77.4 درجة. أظهرت اختبارات FESEM و AFM أن وجود المزيد من جسيمات النانو الفضية يجعل السطح أكثر خشونة ويساعد على نشر الجسيمات النانوية بشكل أفضل حيث زادت خشونة السطح من 2.04 إلى 2.46 نانومتر، وتغير متوسط خشونة الفيلم (Ra) من 1.55 إلى 1.81 نانومتر، وتراوح أقصى ارتفاع للفيلم (Rmax) من 22.34 إلى 25.38 نانومتر. أظهرت نتائج مطيافية الأشعة فوق البنفسجية والمرئية أن المادة تمتص المزيد من الضوء بسبب تأثير رنين البلازمون السطحي الموضعي (LSPR)، مما تسبب في انتقال قمم الامتصاص إلى أطوال موجية أقصر وخفض فجوة الطاقة الضوئية من 2.1 إلكترون فولت لـ P3HT النقي إلى 2 إلكترون فولت بتركيز 0.3٪ وزني من جسيمات النانو الفضية. تتميز مركبات P3HT النانوية مع جسيمات النانو الفضية ببنية وخصائص بصرية أفضل، مما يجعلها مثالية للخلايا الشمسية العضوية والتطبيقات الإلكترونية .

IJL, Issue 2, Vol. 24, 2025
https://doi.org/10.31900/ijl.v24i2.545

Research Article

IRAQI JOURNAL OF LASER

Design and Implementation Driving Circuit of High Power 980 nm Laser Diode

Al-Jumaily, A.K.[1,2,] *, Mansour, T.S[1]

[1]*Institute of Laser for Postgraduate Studies, University of Baghdad, Baghdad, Iraq,*
[2]*Department of Laser and Optoelectronics Engineering, College of Engineering, Al-Nahrain University, Baghdad, Iraq*
**Email address of the Corresponding author*: anmar.k.anjad@nahrainuniv.edu.iq

Article history: Received 7 Aug. 2025; Revised 5 Sept. 2025; Accepted 13 Sept. 2025; Published online 15 Dec. 2025

Abstract: Laser diode with 980 nm has many attractive applications in telecommunication and photonic systems especially when it used for pumping the Erbium–Doped Fiber Amplifiers (EDFAs) which is an essential c- band amplifier that used in many applications for enhancing the nonlinear system conversion efficiency. In this work pulsed laser diode was manufactured after electronically implement the divider circuit with thermal stability of 14 pin 980 nm butterfly laser diode (AGREE SL 90S31A) that has maximum power of 160 mW. This driver circuit was based on the LM317 adjustable current regulator. The electronically chopped 980 nm laser diode achieved stable modulation in the frequency range from 1 Hz to 1 kHz. The proposed driver circuit is simple, low-cost, and successfully provides the required optical modulation for tapered fiber interferometer applications, making it a practical alternative to expensive electro-optic modulation systems such as commercial Lithium Niobate electro-optic modulators which are costly and also require expensive drivers to operate.

Keywords: 980nm Butterfly laser diode driver; pulse modulation; LM317 current regulator; low-cost optical modulator; photonic applications.

1. Introduction

Pulsed fiber-coupled laser diodes are desired sources in optical communication systems with highly sensitivities temporal response unlike continuous wave laser diode that deliver stable optical output. Short bursts of optical energy with excellent timing, fast switching [1]. High speed modulation systems needs pulsed laser to drive the system with advanced optical modulation formats with speed stating from 20 kHz to 21GHz and data rate with 25 Gbps [2]. The pulsed 980 nm laser diode imperative source in optical sensing network that need to use fine allocated narrow-band laser source which essential for high data rete system and long-haul systems [3- 5]. This vital chopped source used for pumping erbium doped fiber which is nonlinear fiber and mandatory optical element in the cavity of fiber laser system that used in many attractive photonic application such as generation of laser with special optical characteristics like multiwavelength, supercontinuum generation in C and L band Rapid time response and narrowing optical pulse can be obtained when the optical interferometric has wavelength division multiplexer operates with 980 nm laser diodes reached to Q- switched optical pulse and also mode locked toward femtosecond laser diodes pulse [3-11].

Laser diode with 980 nm has many features that make it very captivating in biomedical application either operates in continuous or pulsed mode operation with low and high level. In dental application the exposed area of the dental tubules was decreased using continuous 980 nm laser diode and this decreasing was caused by reducing thermal effects and less absorption of heat by water molecules in tissues[11] while for pulsed mode operation this type of laser was used for acceleration the movement of the orthodontic tooth with low peak power that cause less pain and swelling and faster wound healing when compared with 635 laser diode without temporomandibular disorders [12,13].

In medical imagine and optical coherence tomography (OCT), 980 laser diode was used because of its low photothermal damage, leading of reducing microleakage [14]. Main features of 980 nm laser diode that it has higher absorption cross-section and adjustable pulse width and fast rise and falling time make it crucial in optical communication system that needs excellent timing and synchronization [15]. Electronically chopped 980 laser diode has high electrical to optical conversion efficiency which makes it very necessary for designing and construction optical modulator and also optical switcher in all fiber optical communication system with ultra-high modulation speeds that make it a cornerstone in sensing, optical fiber communication system platforms also in application that deals with high modulation bandwidth with high resolution in temporal and spatial domains [16].

2. Experimental Setup and Work's Methodology

There are three circuits that are designed for obtaining stable 980 laser diodes, one for continues mode of operation, second electronically chopped this laser and the third circuit was for investigation stable laser diode with pulse modulation circuit all of these three circuits were explained in the next subsection.

a. Driver Circuit of Continuous Butterfly the 980 nm Laser Diode

The experimental setup**,** as shown in Figure 1, consists of three main components: a regulated DC power supply, an ammeter for current monitoring, and a custom laser diode driver circuit. The butterfly laser diode was mounted on an aluminum heat sink to maintain thermal stability during operation because any overheating leads to performance degradation at the output. The laser diode driver is based on the LM317 integrated circuit (IC). This IC is a multipurpose three-terminal adjustable voltage regulator that is widely used in power supply and current regulation applications. It was designed to provide a stable adjustable voltage output in the range of 1.25 V to 37 V with 1.5 A current.

One of the useful properties of the LM317 is that it can be operated as a constant current source. Such property makes it highly suitable for safely driving sensitive components such as the laser diode used in this work. The LM317 also maintains a fixed voltage drop of approximately 1.25 V between its output and adjustment terminals. By placing a resistor (R) between these terminals, the output current will be regulated according to Ohm's law:

$$\mathrm{Iout} = \frac{\mathrm{V\,ref}}{\mathrm{R}} \qquad (1)$$

Where Vref is the internal reference voltage of the IC, which is equal to 1.25Vin in this work, and R is the value of the resistor that is used to set the target current. This configuration is particularly useful for laser diodes that are highly sensitive to overcurrent conditions. Even small variations in input voltage can cause large changes in output power if not properly regulated. The LM317 effectively prevents such fluctuations by maintaining a stable output current regardless of supply voltage changes.

A schematic diagram of the circuit is shown in Figure 2. The input of the LM317 is a 12V DC supply that is filtered by a 10 µF capacitor to reduce input noise. A 5 Ω resistor of power rating 2W was used to achieve an output current of approximately 250 mA, which is sufficient to operate the 980 nm butterfly-packaged laser diode across a wide range of optical power. Another advantage of the LM317 provides built-in protection, including thermal overload protection, current limiting, and safe area compensation by protecting both the IC itself and the laser diode from excessive power dissipation or short circuits. The output stage includes a protection diode (SD05) connected in parallel with the laser diode to

protect against voltage spikes and accidental reverse polarity. Finally, a DC ammeter and a voltmeter were placed across the laser diode to continuously measure the supplied current and voltage.

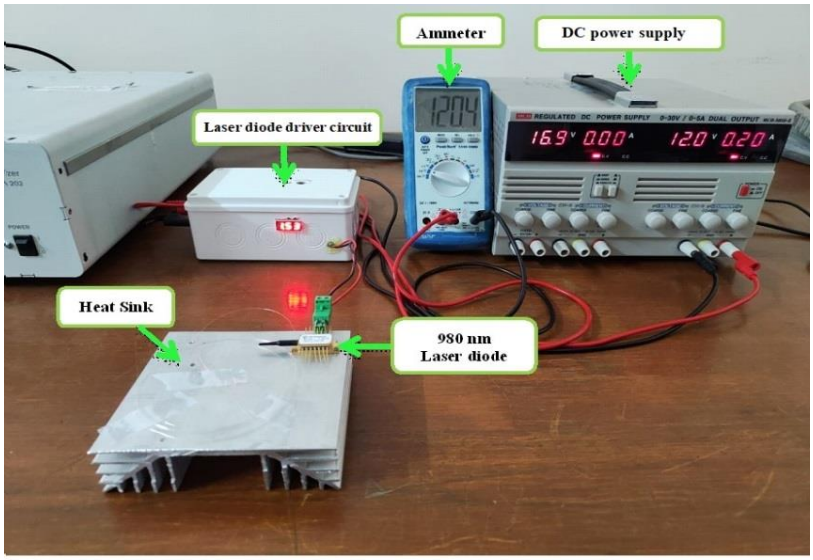

Figure 1: Experimental setup for operating the 980 nm laser diode with current and voltage monitoring.

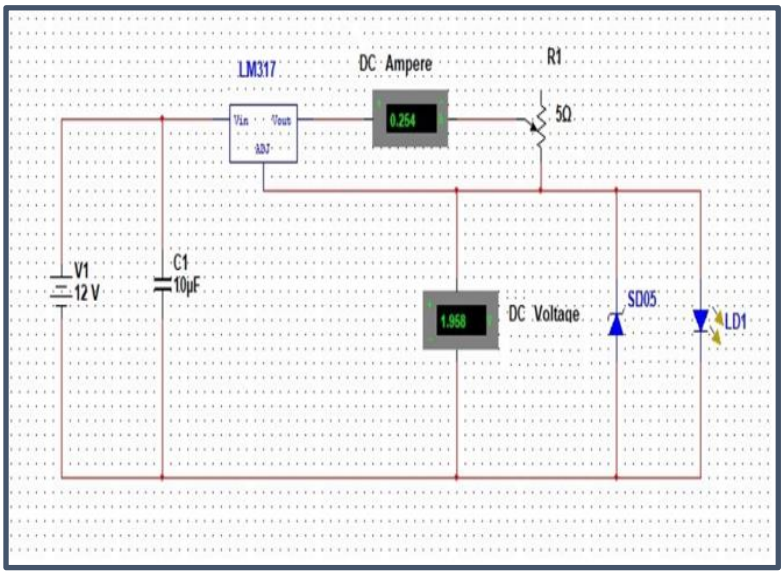

Figure 2: Schematic diagram of the LM317-based constant current laser diode driver circuit.

b. Design and Implementation of Electronically Chopped 980 Laser Diode

In the previous section, the Laser diode is operated and its performance was analyzed in continuous wave mode. In this section, the same laser is operated in pulsed and its performance is also analyzed and various current conditions. A frequency-modulated driver circuit was designed to put the continuous-wave (CW) butterfly laser diode at 980nm into pulse mode operation. The modulation is implemented using an optically

isolated control circuit consisting of a PC817 photocoupler and an IRLZ44 N-channel logic-level MOSFET driver. This configuration enables external digital signals from a function generator or microcontroller to control the laser output while maintaining electrical isolation and protecting the control circuit.
The schematic diagram for the circuit is shown in Figure 3. The design utilizes a photocoupler (PC817) and a logic-level N-channel MOSFET (IRLZ44) to safely drive a laser diode using a pulse signal.

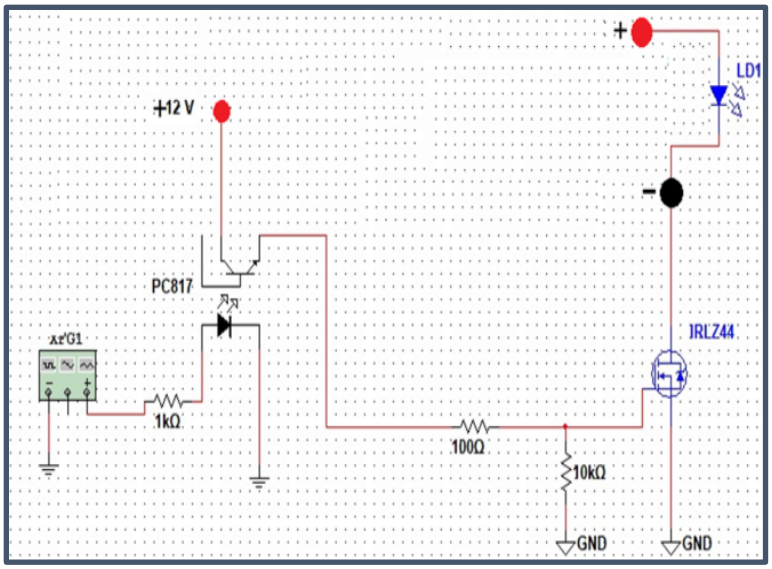

Figure (3): Frequency-modulated driver circuit.

The PC817 is a widely used low-cost photocoupler that provides high isolation voltage between the modulation input and the power stage of the laser driver of a circuit. It contains an internal infrared LED and a phototransistor in a single package. When a control pulse signal from function generator (BK Precision 4075)is applied to the input LED (pins 1 and 2), the emitted light activates the internal Phototransistor and switched it from cutoff to conduction mode, allowing current to pass through the output side across pins 3 and 4. This makes the pulse signal to indirectly control the switching device across the gate of the switching (MOSFET) without direct electrical connection which protects the low-voltage controller from transients and noise.

According to the manufacturer's datasheet, the PC817 exhibits a rise time of 4–10 µs and a fall time of 3–18 µs. These values represent intrinsic device specifications rather than the measured response of the complete system. Therefore, while the PC817 introduces a speed limitation, it ensures circuit protection, and its maximum recommended modulation frequency is typically in the range of 3–10 kHz [17].

The IRLZ44 is a high-speed logic-level N-channel MOSFET which acts as an efficient electronic switch capable of handling high current levels. It can be operated effectively with low gate voltage from 4V to 5V making it compatible with direct driving from logic-level outputs. So, the MOSFET can be activated by the photo coupler allowing the current to flow from the drain to the source to switch the large currents (up to 50 A) through the laser diode.

Based on datasheet specifications, the IRLZ44 exhibits a turn-on delay time of 17 ns, a turn-off delay time of 42 ns, a rise time of 230 ns, and a fall time of 110 ns. These parameters describe the inherent switching capabilities of the MOSFET itself, not the overall driver circuit, and they indicate that the device can theoretically operate at frequencies exceeding 100 kHz, making it suitable for pulse modulation applications [18]. The final circuit is shown in Figure 4. It combines a constant current source based on the LM317 with an optoisolated pulse-controlled MOSFET switch to enable a butterfly-packaged 980 nm laser diode to operate in pulse mode.

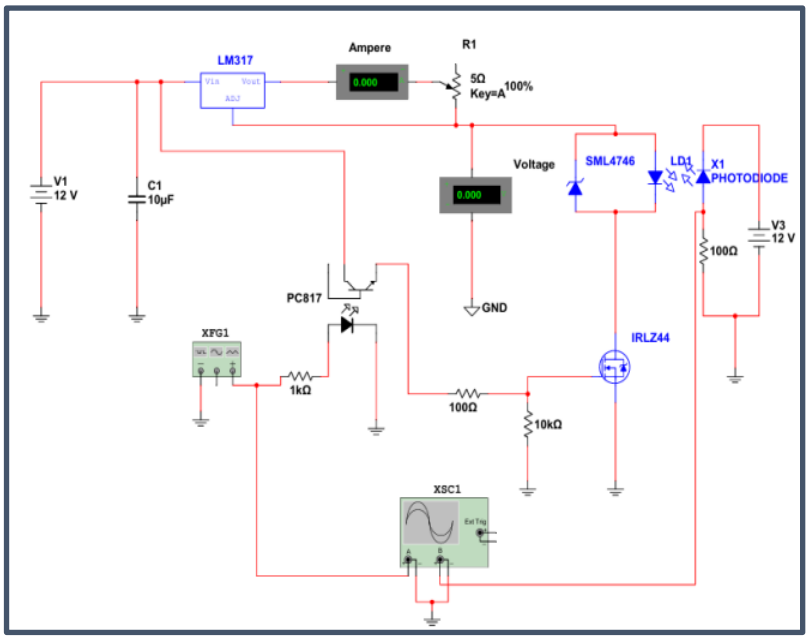

Figure 4: Final driver circuit enabling pulse modulation of a 980 nm butterfly laser diode

3. Result

To characterize the operating performance of the pump laser diode, a series of measurements were carried out to establish the relationship between the applied voltage, the corresponding current, and the resulting optical output power of laser diode. The electrical current was recorded using a digital multimeter (Peak Tech 3340 DMM) while the optical power was measured using an optical power meter (SAT-4E) coupled to the laser diode output through an FC fiber optic connector. The experimental data, summarized in Table 1, show a consistent increase in laser output power with the applied current. It is observed that as the supply voltage is increased from 1.22 V to 2.35 V, the drive current rises from 7.5 mA to 315.8 mA, and the laser output power correspondingly increases from 640 nW to 163.3 mW. This behavior demonstrates the effectiveness of the designed power supply in controlling the laser diode emission across a wide power range, enabling its use in various experimental setups requiring precise optical power control.

The results summarized in Table 1 reveal a direct dependence of the optical output power on the driving current. This relationship is further visualized in Figure 5, showing a nearly linear increase in laser power with increasing current. After stabilizing the output power of the laser diode by properly adjusting the driving current, the device was then operated in pulsed mode at a fixed optical power level without inducing any electrical damage. The response of the laser diode to external modulation was evaluated by applying pulsed signals of varied frequencies through the photocoupler gate. The waveforms were measured using a digital oscilloscope (DS110E). The red traces were taken directly from the function generator output before the input to the photocoupler, while the blue traces were obtained from the photodetector (Thorlabs DET08CFC) connected to the laser diode output that represents the modulated optical signal.

As shown in Figure 6, the blue traces correspond to the pulsed input signals generated by the function generator, while the yellow traces represent the resulting modulated optical output of the laser diode. The observed waveforms at 100 Hz, 500 Hz, and 1 kHz confirm that the circuit successfully reproduces the input modulation pattern with minimal delay and distortion, indicating its suitability for pulse-driven laser applications.

Table 1. Measured voltage, current, and optical power for the 980 nm laser diode.

	Volt (V)	Amp (mA)	Laser power
1	1.22	7.5	640 nW
2	1.27	15.54	3.5 µW
3	1.32	28.77	44.6 µW
4	1.46	47.4	7.47 mW
5	1.56	48	8.1 mW
6	1.65	70	20.78 mW
7	1.8	91.5	36.8 mW
8	1.89	129.3	55.82 mW
9	1.99	171.1	78.5 mW
10	2.06	187	89.43 mW
11	2.11	216.6	106.7 mW
12	2.25	259	130.1 mW
13	2.3	270	137.6 mW
14	2.34	285	146.7 mW
15	2.35	315.8	163.3 mW

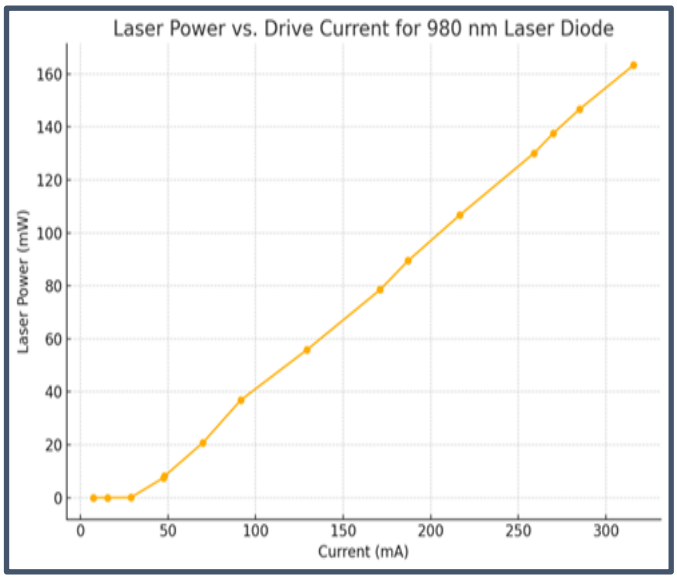

Figure 5: Relationship between drive current and optical output power of the 980 nm laser diode.

4. Conclusion

A highly stable electronically chopped 980 nm laser diode driver was implemented in this work, providing adjustable and reliable temporal characteristics suitable for optical modulation up to 1 kHz. The circuit, based on an LM317 current regulator integrated with pulse modulation, demonstrated simplicity, low cost, and effective performance. This developed pulsed laser source offers strong potential for advanced photonic and sensing applications, particularly in tapered fiber interferometer systems. It also presents a practical alternative to electro-optic modulation systems, such as commercial $LiNbO_3$ electro-optic modulators, which are very expensive. The proposed design represents a cost-effective approach for enhancing nonlinear optical modulation, with promising implications in telecommunication and photonic device integration.

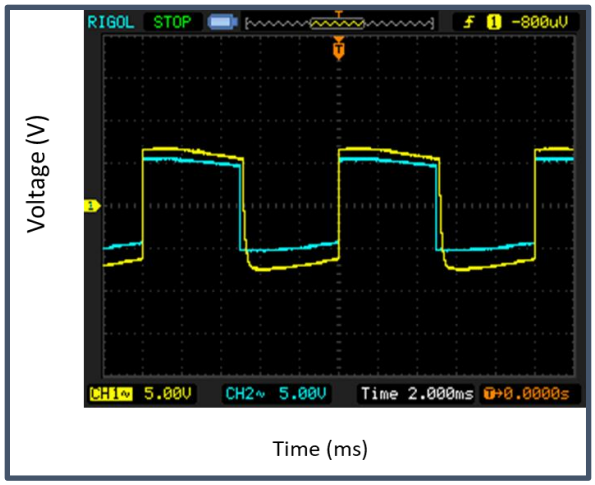

(a)

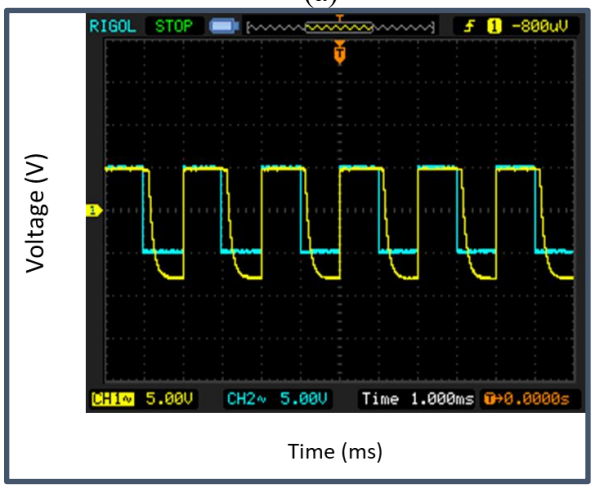

(b)

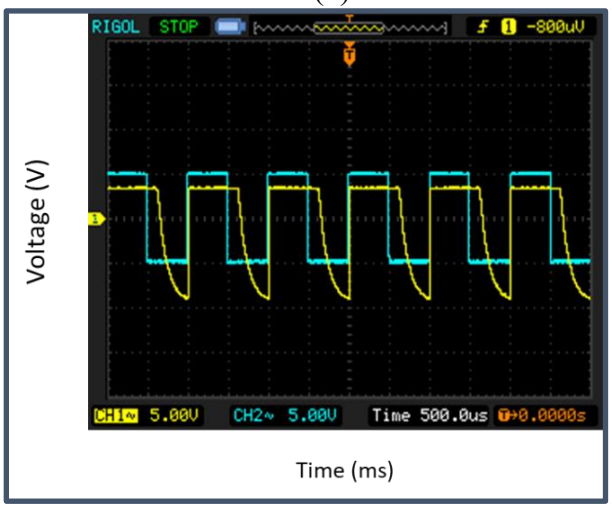

(c)

Figure 6: Frequency response of the 980 nm laser diode showing input pulses (blue) and optical output (yellow) at different modulation frequencies: (a) 100 Hz, (b) 500 Hz, and (c) 1 kHz that confirm stable reproduction of the modulation signals.

References

[1] Hamed Dalir, Yuta Takahashi, and Fumio Koyama, "Low-voltage, high-speed and compact electro-absorption modulator laterally integrated with 980-nm VCSEL", Opt. Express 22, 25746-25755 (2014), DOI: https://doi.org/10.1364/OE.22.025746
[2] Abdul Shakoor, Kengo Nozaki, Eiichi Kuramochi, Katsuhiko Nishiguchi, Akihiko Shinya, and Masaya Notomi, "Compact 1D-silicon photonic crystal electro-optic modulator operating with ultra-low switching voltage and energy," Opt. Express 22, 28623-28634 (2014), DOI: https://doi.org/10.1364/OE.22.028623
[3] Y. I. Hammadi, T. S. Mansour, A. H. H. Al-Masoodi, and S. W. Harun, "Passively femtosecond mode-locked erbium-doped fiber oscillator with external pulse compressor for frequency comb generation", Journal of Optical Communications, vol. 0, no. 0, Nov. 2019, DOI: 10.1515/joc-2019-0240.
[4] Svetlana S. Aleshkina, Andrei Fedotov, Dmitrii Korobko, Dmitrii Stoliarov, Denis S. Lipatov, Vladimir V. Velmiskin, Valery L. Temyanko, Leonid V. Kotov, Regina Gumenyuk, and Mikhail E. Likhachev, "All-fiber polarization-maintaining mode-locked laser operated at 980 nm", Opt. Lett. 45, 2275-2278 (2020) DOI: https://doi.org/10.1364/OL.391193.
[5] Z. Tang et al.," Compact 980-nm all-polarization-maintaining dispersion-managed Figure-9 Yb-doped fiber laser", Journal of Lightwave Technology, vol. 43, no. 15, pp. 7364-7369, 1 Aug.1, 2025, doi: 10.1109/JLT.2025.3570106.
[6] Hani J. Kbashi, Vishal Sharma, Sergey Sergeyev, "Dual-wavelength fiber-laser-based transmission of millimeter waves for 5G-supported Radio-over-Fiber (RoF) links, Optical Fiber Technology", vol.65,2021 https://doi.org/10.1016/j.yofte.2021.102588,
[7] Aseel A. Shakaty, Jassim K. Hmood, Bushra R. Mahdi, and Sulaiman W. Harun, "Passively mode-locked erbium-doped fiber laser based on a nanodiamond saturable absorber", Appl. Opt. 61, 4047-4054 (2022), https://doi.org/10.1364/AO.453751.
[8] Xingwei Li, Huijing Du, Shuguang Li, Jianshe Li, Geng Li, Ling Qin, Meng Li, Menglei Pei, Xingwang Cui, "Supercontinuum generation by nonlinear polarization rotation mode-locked fiber laser with pulse type switchable", Infrared Physics & Technology, Volume 141,2024,105508, ISSN 1350-4495, https://doi.org/10.1016/j.infrared.2024.105508.
[9] Min Won Lee, Fadwa Baladi, Jean-René Burie, Mauro A. Bettiati, Azzedine Boudrioua, and Alexis P. A. Fischer, "Demonstration of optical rogue waves using a laser diode emitting at 980 nm and a fiber Bragg grating", Opt. Lett. 41, 4476-4479 (2016). https://doi.org/10.1364/OL.41.004476.
[10] Hussein Alaa Al-Rubaiyee, Sarah Kadhim Al-Hayali, Sulaiman Wadi Harun, Abdul Hadi Al-Janabi, "Vernier effect based on cascading two Mach–Zehnder interferometers for selectable comb filter and saturable absorber applications in erbium-doped fiber laser", Optical Fiber Technology, Volume 84,2024, https://doi.org/10.1016/j.yofte.2024.103757.
[11] R. Hashim, M. Dhahir, and S. A. AlKurtas, "Effectiveness of 980nm diode Laser in reduction the diameters of exposed dentinal tubules for hypersensitive tooth", IJL, vol. 22, no. 1, pp. 33-42, Jun. 2023, doi: 10.31900/ijl.v22i1.373
[12] Alaa Faiz Abdullah1, Soudad Salman Ahmed, and Balsam Saadi Abdul Hameed, "Exposure of orthodontically Maxillary impacted canine by diode laser (810-980)Nm(comparative study between palatal and buccal position)", IJL, vol. 23, no. 2, pp. 59–68, Dec. 2024, doi: 10.31900/ijl.v23i2.474.
[13] Noor Qasim Mohammed, Zainab F. Mahdi, and Balsam S. Abdulhameed, "A comparative Efficacy of 635 nm and 980 nm low-level laser therapy in treating temporomandibular disorders", IJL, vol. 24, no. 1, pp. 82-92, Jun. 2025, doi: 10.31900/ijl.v24i1.503.
[14] Todea, C., Balabuc, C., Sinescu, C. et al. "En face optical coherence tomography investigation of apical microleakage after laser-assisted endodontic treatment". Lasers Med Sci 25, 629-639 (2010). https://doi.org/10.1007/s10103-009-0680-5.
[15] Jiancheng Zheng, Diao Li, Peng Liu, Xiaoqi Cui, Wei Geng, Qiang Zhang, Zhenyu Xu, Esko I. Kauppinen, and Zhipei Sun, "Synchronized triple-wavelength fiber lasers at 1, 1.55, and 1.9 μm", Opt. Lett. 48, 2619-2622 (2023).
[16] Anusha Dasari, "Optical fiber communication evolution, technology and future trends", Journal of Advance Research in Electrical and Electronics Engineering, Vol. 2 No. 8 (2015), DOI: https://doi.org/10.53555/nneee.v2i8.181
[17] https://www.alldatasheet.com/datasheet-pdf/pdf/11662/ONSEMI/LM317.html
[18] https://www.alldatasheet.com/datasheet-pdf/pdf/252054/VISHAY/IRLZ44.html

تصميم وتنفيذ دائرة قيادة لدايود ليزر عالي القدرة بطول موجي 980 نانومتر

انمار خليل الجميلي [1،2،*]، تحرير صفاء منصور [1]

[1] معهد الليزر للدراسات العليا، جامعة بغداد، بغداد، العراق
[2] قسم هندسة الليزر والإلكترونيات البصرية، كلية الهندسة، جامعة النهرين، الجادرية، بغداد، العراق.

البريد الالكتروني للباحث: anmar.k.anjad@nahrainuniv.edu.iq

الخلاصة: يُعد دايود الليزر بطول موجي 980 نانومتر من المصادر الواعدة في انظمة الاتصالات الضوئية وكذلك في التطبيقات الفوتونية خصوصا عندما يستخدم في ضخ المضخمات الالياف الشمبعة بالاربيوم(EDFA) والتي تعد من المضخمات المهمة والاساسية في تحسين كفاءة التحويل في الانظمة التي تستوجب كفاءة عالية في التحويلات الاخطية.
أما في التطبيقات الصناعية، فيمكن استخدام دايودات الليزر عالية القدرة ضمن هذا الطول الموجي في عمليات اللحام، والقطع، والنقش، واللحام للمواد المتشابهة أو غير المتشابهة، بشرط أن تكون قادرة على امتصاص هذا الطول الموجي.
في هذا العمل، تم تصنيع دايود ليزر بطول موجي 980 نانومتر نوع (AGREE SL 90S31A) بقدرة قصوى تصل إلى 160 mW. استندت دائرة القيادة هذه إلى منظم الجهد القابل للتعديل LM317. وقد حقق الليزر الثنائي عند 980 نانومتر المُقطع إلكترونيًا تضمينًا مستقرًا في مجال التردد من 1 هرتز إلى 1 كيلوهرتز. وتتميز دائرة القيادة المقترحة ببساطتها وانخفاض تكلفتها، كما أنها توفر بنجاح التضمين البصري المطلوب لتطبيقات تداخل الألياف المخروطة (tapered fiber interferometer)، مما يجعلها بديلًا عمليًا للأنظمة المكلفة للتضمين الكهروضوئي مثل المبدلات الكهروضوئية التجارية المصنوعة من نيوبات الليثيوم ($LiNbO_3$)، والتي تتميز بارتفاع تكلفتها وتتطلب أيضًا وحدات تشغيل باهظة الثمن.

IJL, Issue 2, Vol. 24, 2025 **Research Article**
https://doi.org/10.31900/ijl.v24i2.522

Optimization of Er, Cr: YSGG Laser Parameters for Safe and Precise Bone Ablation: An Ex Vivo Histological Study

Noor Majeed Albahdly[1,*], Ameer Dhahir Hameedi[2]

[1]*Institute of Laser for Postgraduate Studies, University of Baghdad, Baghdad, Iraq*
[2]*Collage of Medicine, University of Baghdad, Baghdad, Iraq*
** Email address of the Corresponding Author:* Noor.radi2202m@ilps.uobaghdad.edu.iq

Article history: Received 25 Feb. 2025; Revised 24 Aug. 2025; Accepted 30 Sept. 2025; Published online 15 Dec. 2025

Abstract: The Er, Cr: YSGG laser has emerged as a promising tool for safe and precise bone ablation in dental and maxillofacial procedures. This ex vivo study aimed to optimize the laser parameters to achieve efficient bone cutting with minimal thermal side effects.
Method: This ex vivo study aimed to evaluate the histological effects of varying ER, Cr: YSGG laser parameters on bone incision quality. Mandibular bone samples were collected from three freshly slaughtered sheep and sectioned into six blocks. Osteotomies were performed using an ER, Cr: YSGG laser (2780 nm, Waterlase iPlus) at six different power-frequency combinations (2.5W/20Hz, 4W/20Hz, 6W/20Hz, 4W/30Hz, 6W/30Hz, and 8W/30Hz). Each specimen was irradiated in contact mode for 25 seconds using a MGG6-6 tip, and incisions were evaluated histologically after fixation, decalcification, and H&E staining. Measured variables included incision length, width, length-to-width ratio, carbonization, and precision.
Results: ER, CR: YSGG lasers can be considered practical, effective, and easy for bon incisions. There is no thermal damage. The quality of laser incision at 4W, 20Hz is the best among the parameters($p=0.013$).

Keywords: Bone, histology, incision, IR laser, thermal damage

1. Introduction

One of the oldest forms of orthopaedical treatment is osteotomy. It has been around for nearly a thousand years and is still used today. An osteotomy's fundamental idea is to cut or incision bone, usually to alter the shape or alignment of the bone [1]. Orthopedic surgery has employed various osteotomy techniques to treat deformities and lengthen limbs. Osteotomies are performed with drill bits, electrical saws, and Gigli saws; each has benefits and disadvantages. However, a laser is another method for osteotomy. An erbium laser is one type of laser that was initially employed in maxillofacial surgery [2]. Although the handpiece and bur for osteotomy are effective, they are in direct contact with bone during the cut, causing vibrations and making patients uncomfortable. Thus, it has been suggested that lasers be used for osteotomy treatments. Surgical lasers, however, might facilitate the removal of bone tissue without vibration noises [3]. Bone, known as specialized, living, complex connective tissue, supports and shields the body's critical organs [4]. All bones are composed of a dense outer layer of compact bone and a core of cancellous bone. The cancellous bone is the main component of a bone. It surrounds marrow voids that may contain hematological tissue and form a trabecular network [5]. The accurate, contactless laser

ablation method can remove the body's hard tissue. Laser osteotomy speeds up the healing of the residual bone compared to traditional bone cutting with piezo osteotomes. Recovery is accelerated because the spongy structure is preserved[6]. Bone defect repair is still a significant clinical orthopedic issue. Bone, a highly vascularized tissue, depends on the intimate spatial and temporal relationship between blood vessels and bone cells to preserve skeletal integrity[7]. Laser energy interacts precisely with water and tissues to cut both soft and hard tissue (hydrophotonics). Emission wavelengths, tissue optical characteristics, exposure duration, laser energy, and tissue absorption of the laser energy all affect the outcome of tissue interaction with laser light [8].

Therefore, while cutting bone with a laser, there is less trauma and heat damage. It encourages healing and causes less scar tissue to form, as well as less bleeding and infection[9]. A surgeon can work on tissues more accurately and ablate tissues in hard-to-reach places by using a laser as a surgical tool. A laser can be used during bone cutting to create specific forms and reduce mechanical damage to the surrounding tissue. The properties of the tissue, including its optical characteristics, color, consistency, thermal properties, heat capacity, temperature conductivity, as well as those associated with the laser system, wavelengths, and emission parameters, such as applied power, focal spot size, and emission mode exposure time, determine how the laser acts on the tissue[10-12].

Because water is the chromophore target of the erbium laser, its usage in dentistry goes beyond soft tissues such as mucosa and gingiva to the hard ones, including enamel, dentine, bone, and carious tissue. The thermal effects of erbium lasers on the target tissues can be detected through vaporization. A photomechanical effect is created when water molecules explode, which aids in the ablative and cleaning processes[13].

The Er. Cr: YSGG laser is effective for various dental operations involving both hard and soft tissues because it shows peak absorption by hydroxyapatite (HA) and water at 2780 nm in the infrared spectrum[14]. Since water and hydroxyapatite crystals absorb a large portion of the Erbium, Chromium YSGG laser at 2780 nm wavelength, this free-running pulsed laser has shown promise in treating a variety of hard tissue procedures and soft tissue operations[15].

According to preliminary research, this kind of infrared laser may offer precise, clean, and straight ablation with little thermal harm to nearby tissue because of its water and air sprays. As a result, the Er, Cr: YSGG laser appears to be a substitute tool for oral surgery [16].The biostimulatory effects of laser light irradiation on wound healing, collagen synthesis, and fibroblast proliferation have been used in medical treatments. Additionally, laser light seems to boost adenosine triphosphate (ATP) synthesis and mitochondrial respiration[17]. In dentistry, the Er: YAG (2940 nm) and Er, Cr: YSGG (2790 nm) erbium laser wavelengths are frequently utilized. Among all infrared lasers, they have the highest absorption in water and hydroxyapatite, making them perfect for "optical drilling" in composite fillings, bone, enamel, and dentin [18].

The aim of the present study was to optimize Er, Cr: YSGG laser parameters (2780 nm) for safe and precise bone ablation by assessing histological outcomes in an ex vivo sheep mandible model.

2. Materials and methods

2.1 Sample collection

In this ex vivo study, within four to six hours following slaughter, three Iraqi sheep's mandibles (aged one to one and a half) were used. The bone was preserved in an ice box and kept humidified at the same temperature. The sheep's mandible has been cut into blocks (specimens), with measurements of 1cm in length,2cm in width, and original compact thickness, by electrical saw (Figure 1). The total number was six blocks.

2.2 Laser system

The following instruments were used in this study: Er, Cr: YSGG laser (WATERLASE I plus, BIOLASE)) with a gold handpiece and MGG6-6 laser tip in pulse emission mode (PW).

The laser device is set at six parameters. Each bone specimen was irradiated with Er, CR: YCGG laser 2790nm for 25s for each parameter to make a 2cmm incision. Different laser parameters were used in each irradiation episode. The CNC (computed numerical control) device was used in this experiment to provide a more precise irradiation procedure and verify experimental conditions. This device fixed the bone specimens and held the laser handpiece perpendicular to bone specimens in contact mode; the incision was made with a 2 cm length adjusted in 25 seconds, and the horizontal speed of the CNC device was 0.8 mm/sec.

A CNC device is composed of two parts :(Figure 2)

1-movable part: handle that holds the laser or conventional handpiece and moves in the x-direction through an electrical motor connected to the computer.

2-fix part: mounted table with two arms that hold the bone specimen firmly during laser osteotomy. Figure .3.

Figure. 1: A sheep's mandible, bone specimens.

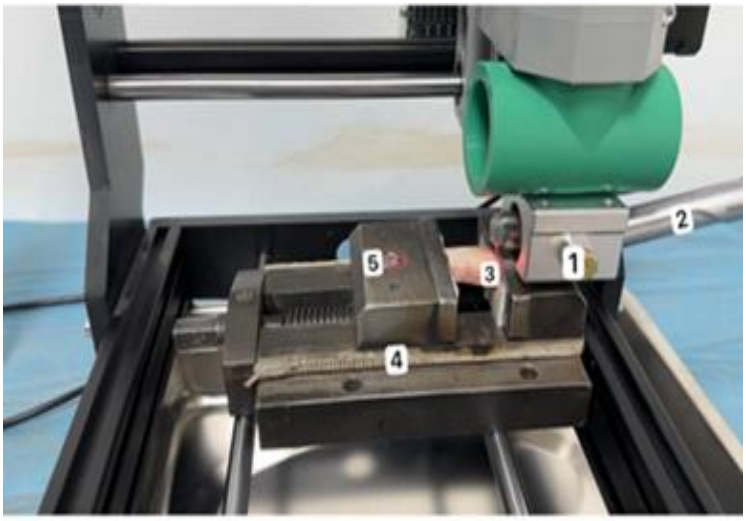

Figure 2: A CNC device:
1- handle,2-laser handpiece,3-bone specimen,4-mounted table,5-the arms that hold the specimen

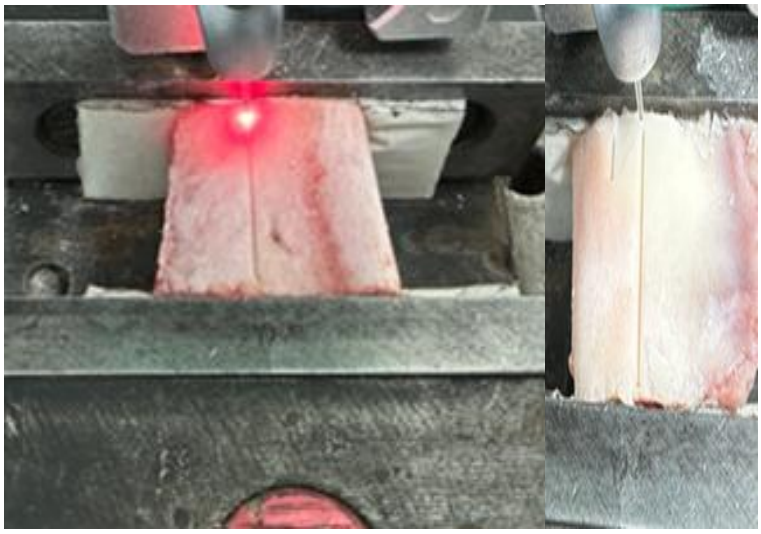

Figure 3: Laser osteotomy.

2.3 Laser Parameters

The laser parameters employed in this ex vivo investigation were selected based on prior research, physician use, and the hard tissue surgical setting of the devices. In order to accomplish the goal of the study, minor differences were made between them. According to the laser parameters setting, the groups were divided as follows: (Table 1)

Table 1. Laser parameters

Laser Group	Power (W)	Energy Per Pulse (mJ)	Water/Air (%)	Frequency (Hz)	Pulse Duration (μs)	Peak Power (W)	Power Density (W/cm²)	Fiber Tip Diameter (μm)
G1	8.0	266.7	50/50	30	60	4.45	2830.3	600
G2	6.0	200.0	50/50	30	60	3.33	2122.7	600
G3	4.0	133.3	50/50	30	60	2.22	1415.1	600
G4	4.0	200.0	50/50	20	60	3.33	1415.1	600
G5	4.0	200.0	50/50	20	60	3.33	1415.1	600
G6	2.5	125.0	50/50	20	60	2.08	884.5	600

2.4 Histological evaluation

After the laser irradiation, a 10% buffered formalin solution was used to fix the specimens. On the same day, they were then sent to the histology lab for a histological analysis. At the laboratory, the bone will be preserved in 10% nitric acid for decalcification for days or weeks according to bone fragment thickness and sequential sample observation. Then, it was put in formalin for 24 hours, dehydrated by graded alcohol, placed in xylene, processed, and embedded in paraffin to prepare a cassette. From these cassettes, sliced s of 5um thickness stained by H and E were examined under scaled lines of the microscope×10 magnifications.

- Slide number

Ten stained slides were obtained from each block, and 60 slides were taken.

2.5 Histological criteria

For histological assessment, each slide was examined under a light microscope by a histologist to evaluate the following for laser osteotomy incision:
1-length of incision
2-width of incision
3-length to width ratio: scored from 1-3 according to the following:
-<0.7 1
-0.7-1.5 2
-> 1.5 3
4. Carbonization: scored from 1-3 according to the following:
Sever 1
Moderate 2
Mild 3
5. Precision: scored from 1-3 according to the following:
Bad 1
Fair 2
Good 3

2.6 Statistical analysis

Continuous variables were expressed as means and standard deviations. Categorical variables were expressed as frequency and percentages. The one-way ANOVA and Tukey's post-hoc test with holm adjustment was performed to find the differences in means between the study groups. The difference between categorical variables was investigated using Fisher's exact test. A P-value less than 0.05 was considered statistically significant. R software packages (dplyr, gt_summery and ggplot) were used for data processing, visualization, and statistical analysis ("R version 4.2.2, R Foundation for Statistical Computing, Vienna, Austria").

3. Result and discussion

3.1 The length, width, and length-to-width ratio (L/W ratio)

Table 2 provides a comparative analysis of the length, width, and length-to-width ratio (L/W ratio) of bone incisions across different study groups subjected to varying laser parameters. The length of bone incision was highest in the 4 W/20 Hz group (0.91 ± 0.08 mm), Figure 7, and lowest in the 2.5 W/20 Hz fig (10), group (0.56 ± 0.04 mm), with a statistically significant difference among the groups ($P < 0.001$). Incision width was greatest in the 2.5 W/20 Hz group (0.79 ± 0.11 mm) and smallest in the 8 W/30 Hz group (0.43 ± 0.05 mm), also with a significant variation ($P < 0.001$). The L/W ratio varied significantly, with the highest ratio observed in the 8 W/30 Hz group (1.66 ± 0.44) fig (9), and the lowest in the 2.5 W/20 Hz group (0.72 ± 0.13). Grading of the L/W ratio revealed that most bone incisions in the 2.5 W/20 Hz group fell into grade 1 (<0.7), whereas incisions in the 8 W/30 Hz group predominantly belonged to grade 3 (>1.5). Statistical tests confirmed significant differences in all evaluated characteristics across groups ($P < 0.001$). Figure 4 illustrates Tukey's post-hoc test for the differences in length-to-width ratio between study groups.

3.2 The precision

Table 3 presents the precision of osteotomy observed in bone incisions subjected to different laser settings. Precision was highest in the 2.5 W/20 Hz group (2.9 ± 0.3)Fig(9), and the 4 W/20 Hz group (2.8 ± 0.4) Fig(7), while the lowest precision was noted in the 8 W/30 Hz group (1.6 ± 0.5) Fig (8).

The grading of precision showed that the majority of cuts in the 2.5 W/20 Hz and 4 W/20 Hz groups were rated as grade 3 (highest precision). In contrast, the 8 W/30 Hz group had a significant proportion of grade 1 (lowest precision). The differences in precision across groups were statistically significant ($P < 0.001$). Figure 5 illustrates ATukey's post-hoc test for the differences in precision scores between study groups.

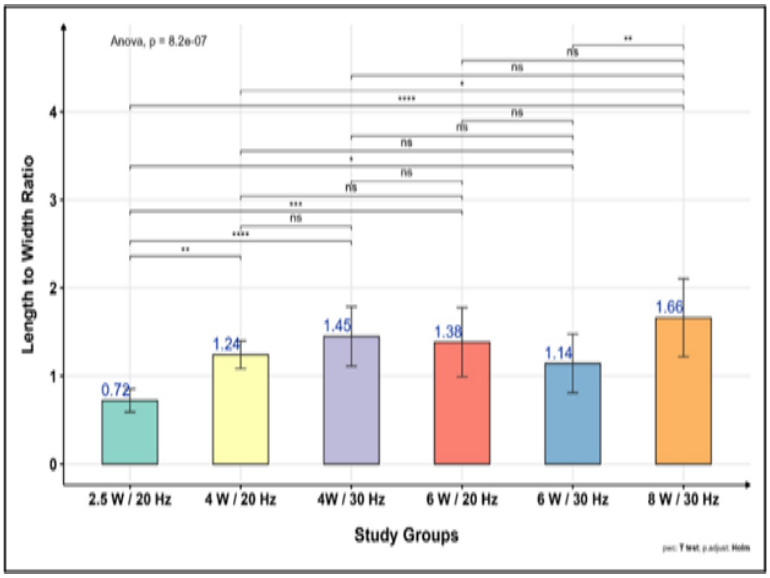

Figure 4: Tukey's post-hoc test for the differences in length-to-width ratio between study groups.

Table 2. Description of length, width, and length-to-width ratio of bone incision in different study groups.

Laser parameter	2.5 W / 20 Hz, N = 10[1]	4 W / 20 Hz, N = 10[1]	4W / 30 Hz, N = 10[1]	6 W / 20 Hz, N = 10[1]	6 W / 30 Hz, N = 10[1]	8 W / 30 Hz, N = 10[1]	P-value[2]
Length (mm)	0.56 ± 0.04^{c}	0.91 ± 0.08^{a}	0.83 ± 0.09^{ab}	0.59 ± 0.05^{c}	0.65 ± 0.11^{cd}	0.73 ± 0.17^{bd}	<0.001
Width (mm)	0.79 ± 0.11^{b}	0.73 ± 0.05^{ab}	0.60 ± 0.14^{ac}	0.47 ± 0.18^{c}	0.59 ± 0.16^{ac}	0.43 ± 0.05^{c}	<0.001
Length-to-width ratio	0.72 ± 0.13^{c}	1.24 ± 0.16^{ab}	1.45 ± 0.34^{ab}	1.38 ± 0.39^{ab}	1.14 ± 0.33^{ac}	1.66 ± 0.44^{b}	<0.001
Grading of L/W ratio							<0.001
1 (<0.7)	6 (60.0%)	0 (0.0%)	0 (0.0%)	3 (30.0%)	1 (10.0%)	0 (0.0%)	
2 (0.7-1.5)	4 (40.0%)	10 (100.0%)	7 (70.0%)	3 (30.0%)	8 (80.0%)	4 (40.0%)	
3 (> 1.5)	0 (0.0%)	0 (0.0%)	3 (30.0%)	4 (40.0%)	1 (10.0%)	6 (60.0%)	

[1]Mean ± SD; n (%)
[2]One-way ANOVA; Fisher's exact test

3.3 The carbonization

Table 3 presents the carbonization of osteotomy observed in bone incisions subjected to different laser settings. The mean scores ranged from 1.0 ± 0.0 in the 2.5 W/20 Hz and 6 W/30 Hz groups to 2.0 ± 0.0 in the 8 W/30 Hz group, indicating the highest degree of carbonization in the latter. Most incisions in the lower power groups (e.g., 2.5 W/20 Hz) exhibited mild carbonization, while all 8 W/30 Hz group incisions showed moderate carbonization. Severe carbonization was observed only in isolated cases within the 4 W/20 HZ group. Statistically significant differences in carbonization were noted among the study groups (P < 0.001).

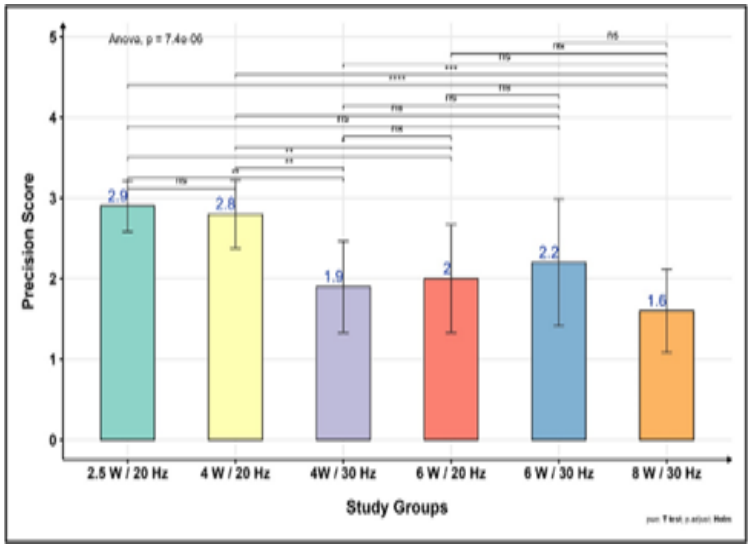

Figure 5: ATukey's post-hoc test for the differences in precision score between study groups

Table 3. Description of precision and carbonization of bone incision using different laser settings.

Laser parameter	2.5 W / 20 Hz, N = 10[1]	4 W / 20 Hz, N = 10[1]	4W / 30 Hz, N = 10[1]	6 W / 20 Hz, N = 10[1]	6 W / 30 Hz, N = 10[1]	8 W / 30 Hz, N = 10[1]	P-value[2]
Precision	2.9 ± 0.3[a]	2.8 ± 0.4[a]	1.9 ± 0.6[b]	2.0 ± 0.7[b]	2.2 ± 0.8[ab]	1.6 ± 0.5[a]	<0.001
1 (bad)	0 (0.0%)	0 (0.0%)	2 (20.0%)	2 (20.0%)	2 (20.0%)	4 (40.0%)	
2 (moderate)	1 (10.0%)	2 (20.0%)	7 (70.0%)	6 (60.0%)	4 (40.0%)	6 (60.0%)	
3 (good)	9 (90.0%)	8 (80.0%)	1 (10.0%)	2 (20.0%)	4 (40.0%)	0 (0.0%)	
Carbonization	1.0 ± 0.0[a]	1.3 ± 0.7[a]	1.2 ± 0.4 [a]	1.3 ± 0.5 [a]	1.0 ± 0.0 [a]	2.0 ± 0.0[b]	<0.001
1 (mild)	10 (100.0%)	8 (80.0%)	8 (80.0%)	7 (70.0%)	10 (100.0%)	0 (0.0%)	
2 (moderate)	0 (0.0%)	1 (10.0%)	2 (20.0%)	3 (30.0%)	0 (0.0%)	10 (100.0%)	
3 (severe)	0 (0.0%)	1 (10.0%)	0 (0.0%)	0 (0.0%)	0 (0.0%)	0 (0.0%)	

[1]n (%)
[2]Fisher's exact test

3.4 The total scores

Table 4 describes the total scores utilized in the study and the statistical differences observed between the study groups. The total scores, presented as mean ± standard deviation (SD), were reported for six different settings, categorized by wattage (2.5 W, 4 W, 6 W, 8 W) and frequency (20 Hz, 30 Hz). The P-value from the one-way ANOVA was 0.013, indicating significant statistical differences between the groups. The highest mean total score was observed in the 4 W / 20 Hz group (7.8 ± 0.8), while the lowest score was found in the 8 W / 30 Hz group (6.2 ± 0.6). Groups with similar total scores were marked with the same superscript letter (e.g., "a" or "b"), and significant differences were noted between groups with different superscripts. Figure 8 illustrates Tukey's post-hoc test for the differences in total scores between study groups.

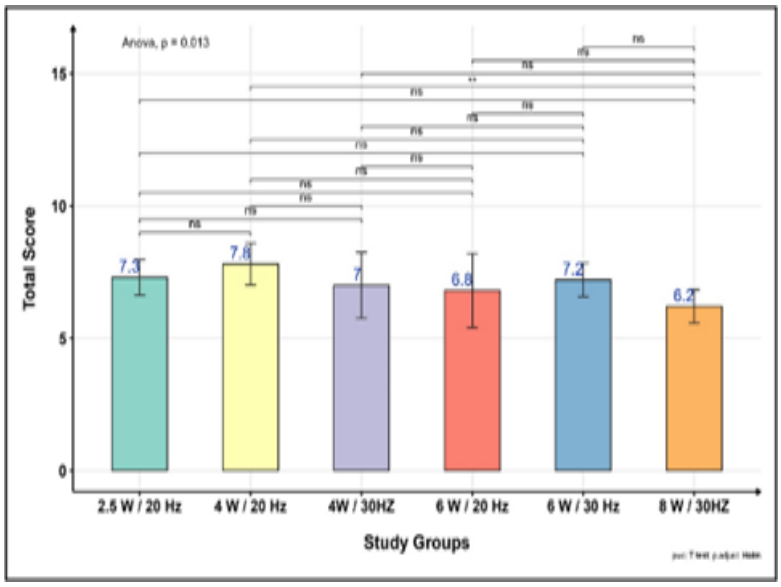

Figure 6: Tukey's post-hoc test for the differences in total scores between study groups.

Table 4: Description of the total score utilized in this study and the statistical differences between the study.

Laser parameter	2.5 W / 20 Hz, N = 10[1]	4 W / 20 Hz, N = 10[1]	4W / 30 Hz, N = 10[1]	6 W / 20 Hz, N = 10[1]	6 W / 30 Hz, N = 10[1]	8 W / 30 Hz, N = 10[1]	P-value[2]
Total score	7.3 ± 0.7[ab]	7.8 ± 0.8[a]	7.0 ± 1.2[ab]	6.8 ± 1.4 [ab]	7.2 ± 0.6 [ab]	6.2 ± 0.6[b]	0.013

[1]Mean ± SD
[2]One-way ANOVA

In laser type, the Er,Cr: YSGG laser, is ideal for surgical procedures, including osteotomy, because it can precisely coagulate arteries and ablate both soft and hard tissue while minimizing heat damage [19].
Because of its high stiffness, high mineral and water content, and quick heat dispersion from the initial absorption layer, hard bone tissue presents difficulties for laser osteotomy [20]. Unlike other laser systems, cutting hard tissue is made possible by an interaction between the laser energy and the water spray, known as the "hydrokinetic effect [21]. A good bone ablation and all forms of treatment of biological hard tissues depend on adequate cooling with an aerosol, ideally made of air and water [22]. This study shows the effect of power and frequency on the quality of laser bone incisions at the histological level.

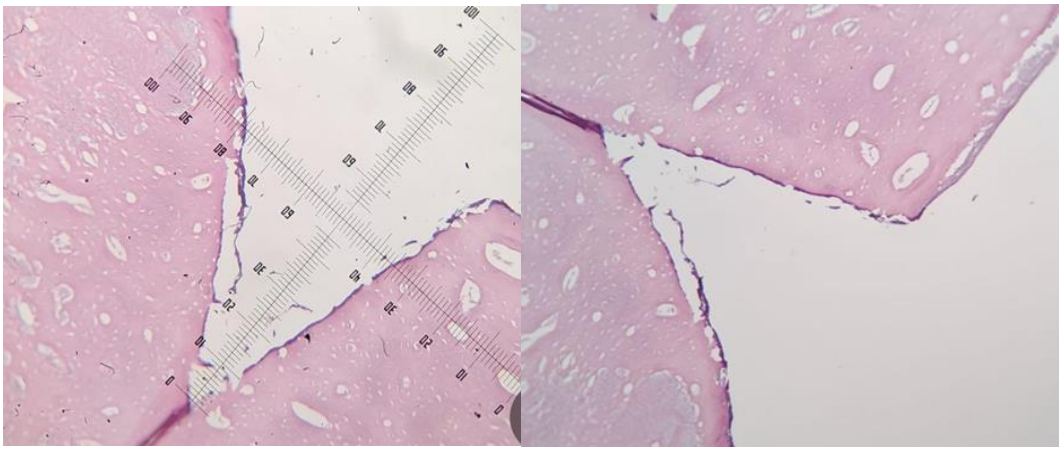

Figure 7: Histological section of Laser osteotomy of 4W 20Hz illustrate deep, precise, less carbonization incision.

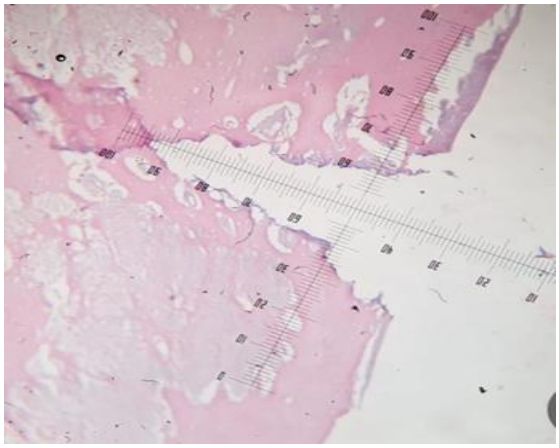

Figure 8: Histological section of laser osteotomy of 8W 30Hz shows the deep, irregular, less precise incision.

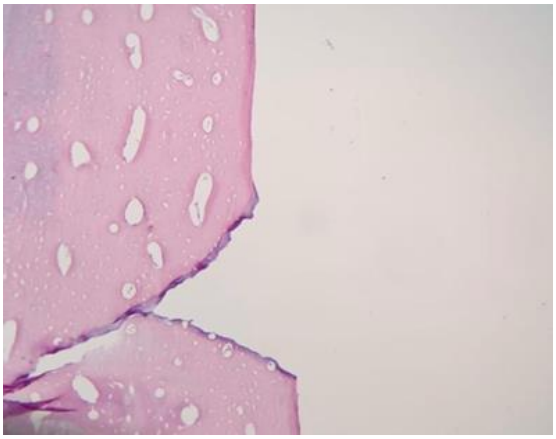

Figure 9:Histological section of laser osteotomy of 2.5W 20Hz shows a precise but shortest depth incision.

Similar to earlier studies, specimens with a high frequency and low radiation power output showed better incision quality, particularly at 20 Hz [23,24]. The incision length was highest in the 4 W/20 HZ group and lowest in the 2.5 W/20 HZ group. One of the important criteria that determines wound efficiency is

the wound depth. Regarding it, an efficiency parameter depends on the clinician's need and how they want to reach their target, which is influenced by other parameters, like the thermal effect when using a laser [25].The length-to-width ratio of laser bone incisions plays a critical role in biopsy procedures, as it directly influences the precision of tissue removal, the extent of thermal damage, and the quality of the histological specimen obtained. In biopsy procedures, a minimal initial incision with a deeper or extended advancement path is preferred to reduce surface trauma and ensure representative tissue sampling [26].In excisional biopsies, specimens collected through laser bone incisions usually have a length-to-width ratio of about 3:1, a shape that improves the accuracy of tissue removal and reduces histological artifacts [27].

Carbonization, which is undesirable in medical laser applications because it increases thermal unfavorable effects on adjacent tissues and slows recovery, is reached as the temperature rises with continued laser exposure. The size, exposure time, and location of the heat deposited inside the tissue are the primary determinants of the ablation's geographic extent[28].

Heat damage and carbonizations are major concerns in the present study, but all examined samples of the laser osteotomy show no thermal damage. Because erbium lasers use water as their primary chromophore, they are a great option for surgical hard tissue procedures. The thermal relaxation time is facilitated by the erbium laser's pulse emission mode and sufficient cooling system [15]. The results of the present study match with evidence from prior ex vivo experiments that demonstrated that the Erbium laser did not cause any heat damage to bone tissue when osteotomy was carried out with cooling air/ water irrigation [29].

Finally, the histological results showed high incision quality with the Er, Cr: YSGG laser system . The interpretation related to laser-tissue interaction depends on multiple laser intrinsic and extrinsic parameters (wavelength, power, mode of emission, beam profile, pulse duration, frequency, and spot size) and the chemical and optical properties of the targeted tissue (tissue chromophores, water, and pigments)[30,31].

4. Conclusion

In ex vivo studies, the Er, Cr: YSGG laser allows for accurate surgical ablation with little thermal damage to nearby tissues. The optimal result is obtained with a 4watt, 20Hz.

References

[1] Kehr P., Fred R.T. Nelson and Carlyn Taliaferro Blauwelt, "A manual of orthopaedic terminology", European Journal of Orthopaedic Surgery & Traumatology, 20(4), 349-349 (2010).
[2] Faschingbauer M., et al., "Are lateral compartment osteophytes a predictor for lateral cartilage damage in varus osteoarthritic knees?: data from the osteoarthritis initiative", The Bone & Joint Journal, 97(12), 1634-1639 (2015.
[3] De Oliveira G.J.P.L., et al., "Effects on bone tissue after osteotomy with different high-energy lasers: an ex vivo study", Photomedicine and laser surgery, 34(7), 291-296 (2016).
[4] Nahian A., and P.R. Chauhan, Histology, periosteum and endosteum, in StatPearls [Internet], StatPearls Publishing (2023).
[5] Farage A.A., and Al Fatlawi F.A., "The measurements of maxillary alveolar bone density at 13-15 years age by using spiral computerized tomography", Journal of Baghdad College of Dentistry, 325(3500), 1-5 (2016).
[6] Beltran B. L.M., et al., "Optimizing controlled laser cutting of hard tissue (bone)", at-Automatisierungstechnik, 66(12), 1072-1082 (2018).
[7] Fadhil E., and Alhijazi, A.Y."Histological and immunohistochemical evaluation of the effect of local exogenous application of VEGF on bone healing (experimental study in rat)", Journal of Baghdad College of Dentistry, 26(4), 108–115 (2014)
[8] Qassab A.H.M., and S.A. Hamad, "Comparison between diode laser and scalpel for lip lengthening in patients with gummy smile", Journal of baghdad college of dentistry, 31(1), 60-64 (2019).
[9] Elmadag, M., et al., "Comparison of four different techniques for performing an osteotomy a biomechanical, radiological and histological study on rabbits tibias", The Bone & Joint Journal, 97(12),1628-1633 (2015).
[10] Jaleel B.A.A., and A.S. Mahmood, "Evaluation the effects of CO_2 Laser on soft and hard tissues (in vitro study)", Iraqi Journal of Laser, 13, 13-22 (2014).

[11] Barrak H., Mahdi S. S., and Alkurtas S. A., "Clinical applications of a 940 nm diode laser for laser troughing versus conventional method: a preliminary study", Iraqi Journal of Laser, 23(2), 52-58 (2024).
[12] Wang X., Zhang C., and Matsumoto K., "In vivo study of the healing processes that occur in the jaws of rabbits following perforation by an Er, Cr: YSGG laser", Lasers in medical science, 20, 21-27 (2005).
[13] Ali F.A., and L. Salman, "Acceleration of canine movement by laser assisted flapless corticotomy [An innovative approach in clinical orthodontics]," Journal of Baghdad College of Dentistry, 26(3), 133-137 (2014).
[14] Mahdi S.-A.-A., and B.-M.-A. Hussein, "Remineralization effect of Er; Cr: YSGG laser irradiation with or without acidulated phosphate fluoride application on deciduous teeth enamel surface with induced white spot lesion: an in vitro study", 16(6), e714–e723 (2024).
[15] Al-Ani A., Taher H., and Alalawi A., "Comparative evaluative study of Erbium, chromium YSGG and wavelength-dual diode lasers in oral soft tissue incision morphology: a histological ex vivo study," Iraqi Journal of Laser, 23(1), 109-117 (2024).
[16] Perussi L.R., et al., "Effects of the Er, Cr: YSGG laser on bone and soft tissue in a rat model", Lasers in medical science, 27, 95-102 (2014).
[17] Alameeri Z.A., and H.A. Jawad, "The Reliability of two different laser wavelengths in inducing bone healing around dental implants: comparative clinical trial", Iraqi Journal of Laser, 22(2), 52-62 (2023).
[18] Diaci J., and B. Gaspirc, "Comparison of Er: YAG and Er, Cr: YSGG lasers used in dentistry", J laser health Acad, 1(1), 1-13 (2012).
[19] Tianmitrapap P., Srisuwantha R., and Laosrisin N., "Flapless Er, Cr: YSGG laser versus traditional flap in crown lengthening procedure," Journal of Dental Sciences, 17(1), 89-95(2022).
[20] Ivanenko M., et al., "Bone tissue ablation with sub-μs pulses of a Q-switch CO_2 laser: Histological examination of thermal side effects," Lasers in Medical Science, 17, 258-264 (2002).
[21] Aria S.A., et al., "Photonics (Er, CR: YSGG and photobiomodulation) versus conventional surgery for impacted lower third molar tooth extraction: a split-mouth, controlled randomized clinical study", Lasers in Dental Science, 6(3), 169-176 (2022).
[22] Romanos G.E., Advanced laser surgery in dentistry. John Wiley & Sons, (2021).
[23]Vescovi P., et al., "Nd: YAG laser versus traditional scalpel. A preliminary histological analysis of specimens from the human oral mucosa. Lasers in Medical Science, 25, 685-691 (2010).
[24] Monteiro L., et al., "A histological evaluation of the surgical margins from human oral fibrous-epithelial lesions excised with CO_2 laser, Diode laser, Er: YAG laser, Nd: YAG laser, electrosurgical scalpel and cold scalpel", Medicina oral, patologia oral y cirugia bucal, 24(2), e271 (2019).
[25] Strakas D., et al., "Evaluation of cutting efficiency and thermal damage during soft tissue surgery with 940 nm-diode laser: An ex vivo study", Lasers in Surgery and Medicine, 55(3), 304- 294 (2023).
[26] Neville B.W., et al., Oral and maxillofacial pathology-E-Book. Elsevier Health Science, (2023).
[27] Farah C., Balasubramaniam R., and McCullough M.J., Contemporary oral medicine, Springer, (2019).
[28] Niemz M. H., Laser-tissue interactions. Springer. 322, (2007).
[29] Stübinger S., et al., "Er: YAG laser osteotomy: preliminary clinical and histological results of a new technique for contact-free bone surgery", European surgical research, 42(3), 150-156 (2009).
[30] Parker P.J., and Parker S.P., Laser safety, in lasers in dentistry-current concepts, Springer, 87-106 (2017).
[31] Kawamura R., et al., "Ex vivo evaluation of gingival ablation with various laser systems and electroscalpel. Photobiomodulation", Photomedicine, and Laser Surgery, 20(6), 364-373 (2002).

تحسين معايير ليزر Er, Cr: YSGG لتحقيق إزالة آمنة ودقيقة للعظم: دراسة نسيجية خارج الجسم على فك الأسفل للغنم

نور مجيد البهدلي[1]،*، أمير ظاهر حميدي[2]

[1]معهد الليزر للدراسات العليا، جامعة بغداد، بغداد، العراق
[2] كلية الطب، جامعة بغداد، بغداد، العراق

البريد الالكتروني للباحث: Noor.radi2202m@ilps.uobaghdad.edu.iq

الخلاصة : برز ليزر (Er, Cr: YSGG) كأداة واعدة للإزالة الآمنة والدقيقة للعظم في الإجراءات السنية والوجهية الفكية. هدفت هذه الدراسة خارج الجسم إلى تحسين معايير الليزر لتحقيق قطع فعال للعظم مع تقليل الآثار الجانبية الحرارية إلى الحد الأدنى. الطريقة: تم الحصول على عينات من عظام الفك السفلي لثلاثة خراف تم ذبحها حديثاً، وقُسمت إلى ست كتل. جرت عمليات قطع العظم باستخدام ليزرEr:Cr: YSGG بطول موجي قدره ٢٧٨٠ نانومتر، وذلك وفق ست مجموعات مختلفة من التوليفات بين القدرة الكهربائية والتردد، وهي: (٢.٥ واط / ٢٠ هرتز)، (٤ واط / ٢٠ هرتز)، (٦ واط / ٢٠ هرتز)، (٤ واط / ٣٠ هرتز)، (٦ واط / ٣٠ هرتز)، و(٨ واط / ٣٠ هرتز) .تم استخدام رأس ليزري **خاص**MGG6-6، وتم توجيه الليزر على كل عينة بوضع التلامس لمدة ٢٥ ثانية .بعد ذلك، خضعت العينات للتثبيت الكيميائي، وإزالة التكلس، ثم التلوين بصبغة الهيماتوكسيلين والإيوزين لغرض التقييم النسيجي .شملت المتغيرات التي تم قياسها: طول الشق، عرضه، النسبة بين الطول والعرض، درجة التفحم، ودقة القطع. النتائج: يمكن اعتبار ليزر (Er, Cr: YSGG) وسيلة عملية وفعالة وسهلة الاستخدام في إجراء شقوق العظام. لم تُلاحظ أي أضرار حرارية . وُجد أن جودة الشق باستخدام الليزر عند قدرة ٤ واط وتردد ٢٠ هرتز هي الأفضل مقارنة ببقية الإعدادات.